Master Thesis

Stimulated phase conjugation of structured single photons through cascaded parametric down-conversion

Author:
Tobey Luck

Supervisor:
Professor Robert W. Boyd

Thesis submitted to the University of Ottawa
in partial fulfillment of the requirements
for the Master of Science degree in Physics

Department of Physics
Faculty of Science
University of Ottawa

© Tobey Luck, Ottawa, Canada, 2026

Declaration of Authorship

I, Tobey Luck, declare that this thesis was written by myself. The contributors to this thesis are:

For the theory developed for biphoton generation in Chapter 2, the work was supervised by Prof. Robert Boyd, with direct oversight and direction provided by Mr. Aarón Aguilar-Cardoso, Dr. Manuel Ferrer-Garcia, Dr. Cheng Li, Dr. Jeremy Upham, and Prof. Jeff Lundeen.

In Chapter 3, the corresponding experiments for the two studies examined were done by Mr. Aarón Aguilar-Cardoso. The analysis of these experiments received direction and input from myself, Dr. Cheng Li, Dr. Jeremy Upham, and Prof. Jeff Lundeen. The development was supervised by Dr. Manuel Ferrer-Garcia and Prof. Robert Boyd.

For Chapter 4, the concept of the experiment was developed by Mr. Aarón Aguilar-Cardoso and Dr. Manuel Ferrer-Garcia. The theoretical work was done by myself and Aarón Aguilar-Cardoso. We received additional support from Dr. Cheng Li, Dr. Jeremy Upham, and Prof. Jeff Lundeen. The project was supervised by Dr. Manuel Ferrer-Garcia and Prof. Robert Boyd.

Chapter 5 discusses the outcomes of the study done in Chapter 4. This analysis was supervised by Prof. Robert Boyd with additional input and direction from Dr. Manuel Ferrer-Garcia and Dr. Jeremy Upham.

Abstract

Stimulated parametric down-conversion (StimPDC) can act as a phase-conjugating nonlinear process when one of the down-converted modes is driven by a bright classical field. In this regime, the stimulated contribution to the nonlinear interaction dominates over the spontaneous background and the generated idler reproduces the conjugated phase of the seed with high fidelity. This behaviour has enabled classical turbulence-mitigation schemes in free-space optical channels, where a probe beam acquires a distorted wavefront that is deterministically conjugated in a nonlinear crystal and corrected upon reverse propagation.

This thesis examines whether the same mechanism can be extended to the single-photon regime. The analysis begins by reviewing the spatial-mode structure of classical StimPDC using a Laguerre–Gaussian description of the nonlinear interaction. The turbulence-mitigation protocol is then summarized to clarify why high-fidelity phase conjugation is central to its operation. The main theoretical development introduces the single-photon–seeded version of the process, referred to as SPS-PDC. Using the full biphoton amplitude of SPS-PDC, the idler mean photon number is derived and shown to contain coherent spontaneous and stimulated contributions of comparable magnitude when only one photon occupies the seeded mode. Because the stimulated term no longer overwhelms the spontaneous background, the generated idler does not reproduce a unique conjugated wavefront. This result identifies a fundamental limit: perfect phase conjugation cannot be achieved with a single-photon seed in a second-order nonlinear interaction of this type.

The implications of this scaling behaviour are examined in the context of turbulence mitigation and quantum key distribution. Although a single-photon version of the classical protocol would offer intrinsic security, the absence of deterministic conjugation prevents reliable wavefront correction. The thesis concludes by outlining an experimental approach for resolving the joint spatial structure of the two idler photons produced in a cascaded parametric down-conversion process. Such measurements would directly test the predicted division between spontaneous and stimulated contributions and further clarify the boundary between classical and quantum phase-conjugation regimes.

Acknowledgements

I would first like to express my sincere gratitude to my supervisor, Prof. Robert W. Boyd. His guidance, patience, and deep expertise in photonics have been central to my development as a researcher. He fostered an environment that emphasized both intellectual rigor and independence, and he created a research group at the University of Ottawa in which I had the opportunity to work alongside outstanding scientists and pursue challenging problems in nonlinear and quantum optics.

I am also grateful to Prof. Jeff Lundeen and Dr. Jeremy Upham, whose advice and practical insight were invaluable throughout my graduate studies. I would like to thank Dr. Manuel Ferrer-Garcia, Mr. Aarón Aguilar-Cardoso and Dr. Cheng Li for their mentorship and for sharing their approach to tackling difficult research questions and developing feasible, well-motivated research ideas. I am thankful to my colleagues Dr. Yaswant Vaddi, Theng-Loo Lim, Yaryna Mamchur, Mahtab Amooei, Omid Mozafar, Sisira Suresh, Dr. Margoth Cordova-Castro, Mahdieh Jabbari, and Dr. Maryam Abbasi for their discussions, collaboration, and support, all of which contributed meaningfully to my graduate experience.

Finally, I am deeply grateful to my mother for her patience, encouragement, and unwavering support. Her confidence in me made this work possible.

Contents

Declaration of Authorship ii

Abstract iii

Acknowledgements iv

1 Introduction 1

2 Core Theory of $\chi^{(2)}$ Interactions and Biphoton Generation 5
2.1 Introduction . . . 5
2.2 Maxwell Equations and the Wave Equation with Polarization . . . 6
2.2.1 Scope and Approximations . . . 7
2.3 Classical Nonlinear Polarization . . . 7
2.3.1 Expansion of the Polarization . . . 8
2.3.2 Tensor Structure of $\chi^{(2)}$ . . . 8
2.3.3 Phase Matching and Energy Conservation . . . 9
2.3.4 Undepleted-Pump Approximation . . . 9
2.4 Quantized Electromagnetic Field . . . 10
2.4.1 Mode Expansion and Ladder Operators . . . 10
2.4.2 Positive and Negative Frequency Components . . . 11
2.4.3 Quantized Interaction Hamiltonian for $\chi^{(2)}$ . . . 11
2.5 First-Order Solution and the Biphoton State . . . 12
2.5.1 Perturbative Evolution . . . 12
2.5.2 Two-Photon Component of the State . . . 14
2.5.3 Interpretation of the Biphoton Amplitude . . . 14
2.6 LG Basis and Spatial Structure of the SPDC State . . . 15
2.7 Summary . . . 17

3 Stimulated Parametric Down-Conversion and Classical Phase Conjugation 19
3.1 Introduction . . . 19
3.1.1 Interaction Hamiltonian with a Classical Seed . . . 20
3.1.2 Field-Level Description of StimPDC . . . 20
3.1.3 Dependence on Pump–Seed Waist Ratio and Radial Coupling . 22
3.2 StimPDC for Turbulence Mitigation . . . 22
3.2.1 Phase Structure and Information Transfer in the StimPDC Geometry . . . 23
3.2.2 Relevant QKD Definitions . . . 24
3.2.3 QKD Implementation in the Turbulence-Mitigation Experiment 26
3.2.4 Motivation for a Single-Photon Extension . . . 27
3.2.5 Single-Photon Perspective on Turbulence Cancellation . . . 28
3.3 Summary . . . 29

4 Single-Photon Seeding and Cascaded Parametric Down-Conversion 30
4.1 Introduction 30
4.2 Summary of Key Results 30
4.3 Author Contributions 31
4.4 Embedded Manuscript 31

5 Implications of the Theoretical Findings 50
5.1 Introduction 50
5.2 Classical and Single-Photon Seeded StimPDC 51
5.3 Photon-Number Scaling of Stimulated and Spontaneous Contributions 52
5.4 Deterministic versus Conditional Phase Conjugation 54
5.5 Limits of Phase Conjugation as a Quantum Operation 56
5.6 Consequences for Phase Conjugation Protocols 57
5.7 Implications for QKD and Turbulence Mitigation 57
5.8 Experimental Considerations 58
5.8.1 Preliminary Search for Temporal Correlations in SPDC 58
5.8.2 Joint-Idler Measurements in CPDC 59
5.9 Summary and Outlook 61

A Related Coauthored Publications 62
A.1 Tailoring spatial modes produced by stimulated parametric down-conversion 62
A.2 All-optical turbulence mitigation for free-space quantum key distribution using stimulated parametric down-conversion 71

Bibliography 81

List of Figures

1.1 Representative LG intensity and phase profiles for several values of ℓ and p, where the superscript denotes the azimuthal index ℓ and the subscript denotes the radial index p in the notation LG_p^ℓ. The azimuthal phase term $e^{i\ell\phi}$ determines the orbital angular momentum of the mode, while the radial index p controls the number of radial nodes and the radial extent of the intensity distribution. 2

2.1 Wave-vector geometry for three-wave mixing in a $\chi^{(2)}$ crystal. The pump wave vector $\mathbf{k}_p$ decomposes into the signal and idler wave vectors. The lower panel shows the longitudinal components, and the small mismatch Δk_z between $k_{p,z}$ and $k_{i,z} + k_{s,z}$ reduces the conversion efficiency and sets the phase-matching envelope. 9

2.2 Schematic of the $\chi^{(2)}$ interaction. A classical pump field drives the creation of a signal-idler photon pair. The positive-frequency component of the pump couples to the negative-frequency components of the quantized fields, corresponding to the creation operators in Eq. (2.28). 12

2.3 Normalized intensity profiles of LG modes with fixed azimuthal index $\ell = 1$ and increasing radial index p. The redistribution of intensity with increasing p alters the spatial overlap with the pump field and hence the magnitude of the nonlinear coupling coefficients. 16

3.1 Stimulated parametric down-conversion in a $\chi^{(2)}$ crystal. A classical seed field E_s and a pump field E_p overlap inside the nonlinear medium. The nonlinear polarization driven by their product generates an idler field whose transverse structure is proportional to $E_p E_s^*$. This geometry provides an intuitive picture of the spatial overlap that appears analytically in the StimPDC interaction Hamiltonian and underlies the phase conjugation behaviour derived in the text. 21

3.2 StimPDC turbulence-mitigation geometry. (a) A Gaussian probe from Bob traverses the turbulent channel left to right and acquires a distorted phase before reaching Alice. Inside Alice's $\chi^{(2)}$ crystal the distorted probe overlaps with an information-bearing pump field shaped in the desired spatial mode. The generated idler carries the pump mode together with the conjugated turbulence distortion. (b) The idler propagates back through the same turbulent channel from right to left, so that the accumulated phase cancels the conjugated distortion and Bob receives a corrected spatial mode at position v. Insets illustrate the phase of the different beams at the labelled positions. 25

5.1 Preliminary experiment designed to probe mode-resolved temporal correlations in Type-II SPDC. A 405 nm pump drives SPDC in a ppKTP Type-II crystal, producing orthogonally polarized signal and idler photons that are separated using a polarizing beam splitter. Each arm is expanded, projected onto a selected LG mode using an SLM, and coupled into a single-mode fibre connected to a single-photon detector. Detection events are analyzed using a temporal correlator to search for coincidence peaks associated with conjugate OAM projections. 59
5.2 Proposed CPDC joint-idler measurement. A 405 nm pump is split to drive an SPDC stage (left) and an SPS-PDC/CPDC stage (right). Detection of the first idler photon heralds the presence of a single-photon seed in the second crystal. The two idler photons are analysed independently using spatial light modulators, single-mode fibres, and single-photon detectors D_1 and D_2. Coincidence counts between the two detection arms probe the joint-idler mean photon numbers predicted in Chapter 4. 60

List of Abbreviations

BPF	Band-Pass Filter
CPDC	Cascaded Parametric Down-Conversion
CW	Continuous Wave
DM	Dichroic Mirror
LG	Laguerre–Gaussian
OAM	Orbital Angular Momentum
PBS	Polarizing Beam Splitter
PDC	Parametric Down-Conversion
QBER	Quantum Bit Error Rate
QKD	Quantum Key Distribution
SLM	Spatial Light Modulator
SMF	Single-Mode Fiber
SPDC	Spontaneous Parametric Down-Conversion
SPS-PDC	Single-Photon–Seeded Parametric Down-Conversion
StimPDC	Stimulated Parametric Down-Conversion

Chapter 1

Introduction

Free-space optical communication can involve the encoding of information in many physical parameters of light, including polarization, frequency, and time-bin structure. Among these, the transverse spatial structure of optical beams is particularly attractive because it supports high-dimensional alphabets that are useful in both classical multiplexing and quantum communication [1, 2]. Laguerre-Gaussian (LG) modes are a widely used spatial-mode basis: each LG mode carries orbital angular momentum (OAM) through an azimuthal phase factor $\exp(i\ell\phi)$, and the unbounded index ℓ provides a large state space for mode-division multiplexing and high-dimensional quantum encoding [1, 2, 3]. Representative intensity and phase profiles for several LG modes are shown in Fig. 1.1. OAM has also been established as a native degree of freedom for entanglement and quantum-state engineering, beginning with early demonstrations of OAM entanglement in spontaneous parametric down-conversion (SPDC) [4] and extending to high-dimensional quantum cryptography in which the transverse mode index directly labels the information alphabet [5, 6].

A central obstacle for spatial-mode communication is propagation through inhomogeneous media. Atmospheric turbulence and related refractive-index fluctuations imprint spatially varying phase distortions that degrade mode purity and increase cross-talk between OAM channels [7, 8]. These distortions are stochastic and evolve on millisecond timescales, faster than the response of most digital correction systems [7]. Explicit wavefront sensing and channel estimation are therefore unattractive: they require real-time measurement and feedback that struggle to keep pace with the channel dynamics. It is instead attractive to seek all-optical correction methods that respond at the speed of the nonlinear interaction itself. Phase conjugation is one such method: by generating a field whose wavefront is the complex conjugate of an input, subsequent propagation through a reciprocal channel can reverse accumulated aberrations and recover the original mode structure [7, 9, 10, 11]. In the context of OAM, phase conjugation inverts the azimuthal phase $\ell \to -\ell$ and more generally reverses phase distortions present in arbitrary spatial superpositions [2, 8].

Stimulated parametric down-conversion (StimPDC) in a $\chi^{(2)}$ crystal provides a convenient all-optical route to phase conjugation. The mechanism differs from classical phase conjugation schemes such as four-wave mixing in an important respect: the generated idler is not a time-reversed replica of the seed propagating in the reverse direction, but instead a new field at frequency $\omega_i = \omega_p - \omega_s$ whose transverse phase structure is conjugated relative to the seed. Specifically, when a classical pump is mixed with a bright classical seed, the generated idler inherits a transverse structure proportional to the product $E_p E_s^*$, so the idler carries the pump envelope together with the conjugated phase of the seed [12, 13, 14]. This is illustrated schematically in Chapter 3 (Fig. 3.1). This mechanism can be exploited for turbulence mitigation by sending a probe through a turbulent channel, generating an idler that carries the conjugated probe phase at the receiver, and then returning the idler through the same channel

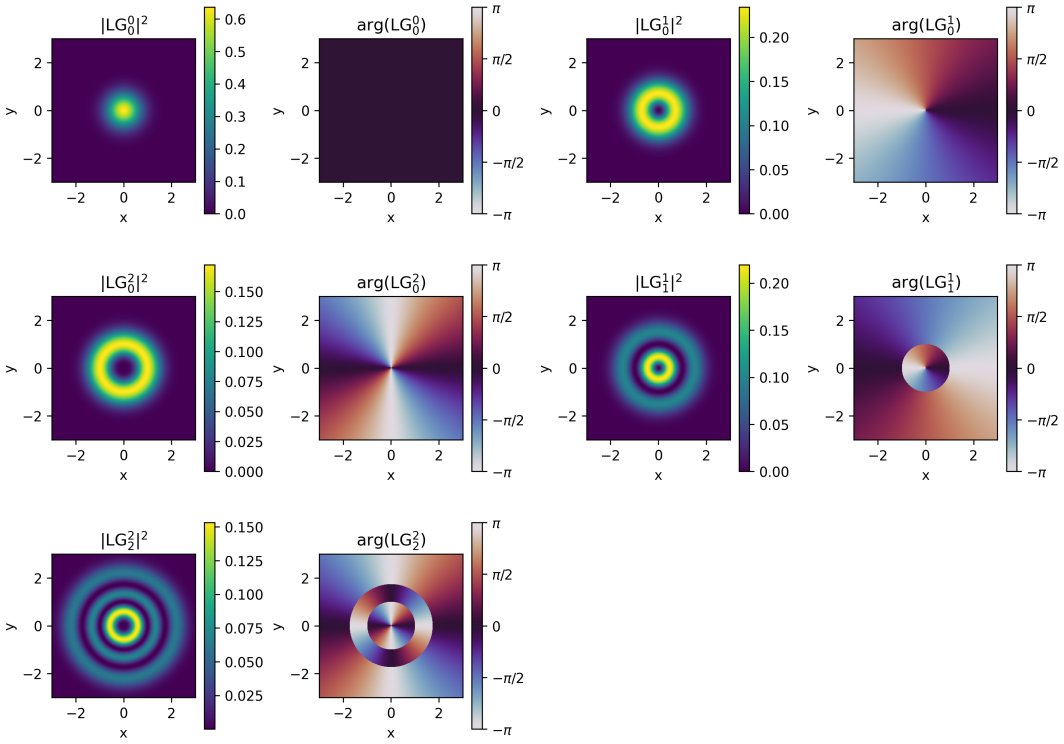


FIGURE 1.1: Representative LG intensity and phase profiles for several values of ℓ and p, where the superscript denotes the azimuthal index ℓ and the subscript denotes the radial index p in the notation LG_p^ℓ. The azimuthal phase term $e^{i\ell\phi}$ determines the orbital angular momentum of the mode, while the radial index p controls the number of radial nodes and the radial extent of the intensity distribution.

so that the turbulence phase cancels on a round trip [15]. In the classical regime, the seed is bright and the stimulated contribution dominates over spontaneous emission, yielding deterministic wavefront reversal and high-fidelity spatial-mode transfer as confirmed in spatially resolved StimPDC measurements [12, 16].

The question addressed in this thesis is the extent to which this phase-conjugation mechanism persists when the seed contains a single photon. If a single-photon analogue of deterministic StimPDC phase conjugation existed, it could enable turbulence-mitigation strategies that are compatible with quantum communication, where an eavesdropper cannot measure or copy the travelling state without disturbance [17, 18]. This motivation is particularly strong for OAM-based quantum key distribution (QKD), where turbulence-induced mode mixing can directly increase error rates and reduce achievable key rates [5, 6, 8]. At the same time, prior work on SPDC spatial correlations and OAM structure provides the tools needed to formulate the seeded interaction in a spatial-mode basis [4, 19, 20].

A key complication is that the single-photon-seeded process necessarily operates in a regime where spontaneous and stimulated contributions are comparable. In classically seeded StimPDC, increasing the seed photon number produces stimulated dominance and suppresses the relative impact of spontaneous emission, but a single photon cannot provide that scaling advantage. More broadly, seeded and unseeded contributions coexist in parametric down-conversion at the operator level, and their competition becomes experimentally and conceptually important whenever the seed flux is not macroscopic [21]. The central problem is therefore not whether a conjugated component exists, but whether it can be isolated as a deterministic single-photon output mode analogous to the classical idler field.

This thesis resolves the question by deriving the single-photon-seeded StimPDC process within a cascaded PDC model. The analysis shows that the idler contains a stimulated contribution that carries the conjugated spatial structure associated with the seed and a spontaneous contribution that does not; when the seed contains only one photon, these contributions remain comparable and the idler cannot be described as a clean, deterministic phase-conjugated replica of the input. This distinction follows directly from photon-number scaling and persists independent of pump shaping, crystal geometry, or alignment, thereby identifying a clear boundary between classical and quantum operation in StimPDC [12, 21].

In addition to the theoretical analysis, the thesis proposes a spatially resolved joint-idler measurement that directly probes the cascaded output. By resolving each idler photon in a chosen transverse mode and recording coincidence counts, the experiment samples the joint idler distribution predicted by the model and tests the separation between spontaneous and stimulated contributions that is otherwise hidden in unconditional measurements [16, 21]. This provides a concrete route to observing single-photon phase-conjugated correlations even when deterministic single-photon wavefront reversal is not available.

Two related coauthored publications are reproduced in Appendix A and are directly relevant to the work developed here. The first, Ref. [16], presents a theoretical and experimental study of spatial-mode generation and control via classical StimPDC, establishing the LG-mode framework and waist-ratio dependence that underpin the analysis in Chapter 3. The second, Ref. [15], proposes and demonstrates the all-optical turbulence-mitigation scheme whose single-photon extension is the central motivation of this thesis. Both works represent substantive collaborative contributions, and together they provide the experimental context for the theoretical developments that follow.

The structure of the thesis reflects this progression. Chapter 2 reviews the quantum and nonlinear optics used throughout the work. Chapter 3 develops classical StimPDC, its field-level phase-conjugation behaviour, and the corresponding turbulence-mitigation geometry. Chapter 4 derives the cascaded SPDC description of single-photon-seeded StimPDC and presents the embedded manuscript containing the full theoretical development. Chapter 5 places the results in context, clarifies the distinction between deterministic classical phase conjugation and conditional single-photon signatures, discusses implications for turbulence mitigation and QKD, and outlines experimental steps for observing the predicted joint-idler structure.

Chapter 2

Core Theory of $\chi^{(2)}$ Interactions and Biphoton Generation

2.1 Introduction

The goal of this chapter is to develop the theoretical framework required for the analysis of stimulated and cascaded parametric down-conversion in the chapters that follow. The emphasis is on the classical and quantum aspects of second-order $\chi^{(2)}$ nonlinear interactions that govern photon-pair generation, spatial-mode correlations, and the behaviour of seeded processes. Rather than providing a broad survey of nonlinear or quantum optics, the chapter focuses on deriving the specific results needed to construct the biphoton state produced by SPDC and to analyze its spatial structure in a mode-resolved description.

The discussion begins with the classical nonlinear response of a dielectric medium and the origin of three-wave mixing in materials with nonvanishing second-order susceptibility. Starting from the expansion of the nonlinear polarization, the role of energy conservation and phase matching is established following standard treatments in nonlinear optics. These considerations determine the frequency and wave-vector constraints that ultimately shape the spatial and spectral structure of the generated fields.

The treatment then moves to the quantized electromagnetic field and the construction of the interaction Hamiltonian for a $\chi^{(2)}$ medium under the undepleted-pump approximation. This formulation follows the canonical approach developed by Mandel and Wolf [22] and related quantum-optical treatments, in which the pump is treated classically while the signal and idler fields are quantized. Within this framework, the first-order perturbative solution of the Schrödinger equation yields the two-photon component of the output state produced by SPDC.

The resulting biphoton amplitude plays a central role throughout the remainder of the thesis. Its structure is determined by spatial-overlap integrals involving the pump profile, the transverse mode functions of the signal and idler fields, and the phase-matching envelope imposed by the finite crystal length. To make these features explicit, the transverse modes are expressed in the LG basis, which provides a natural description of orbital angular momentum transfer and radial-mode coupling in paraxial beams [23]. In this representation, conservation of orbital angular momentum and the weighting of radial modes emerge directly from the angular and radial structure of the overlap integrals.

The final sections connect the mode-resolved structure of the SPDC biphoton state to the seeded interactions that appear in StimPDC and CPDC. In these processes, a photon drawn from the biphoton state acts as an input to a second $\chi^{(2)}$ interaction, and the same overlap integrals derived in this chapter govern how phase and spatial

information are transferred to the idler field. The results presented here therefore provide all theoretical ingredients required for the analyses in Chapters 3 and 4.

2.2 Maxwell Equations and the Wave Equation with Polarization

The starting point for the classical and quantum descriptions developed in this thesis is Maxwell's equations in a dielectric medium. In the absence of free charges and free currents, they take the form [12, 13, 24]

$$\nabla \cdot \mathbf{D}(\mathbf{r},t) = 0, \tag{2.1}$$

$$\nabla \cdot \mathbf{B}(\mathbf{r},t) = 0, \tag{2.2}$$

$$\nabla \times \mathbf{E}(\mathbf{r},t) = -\frac{\partial \mathbf{B}(\mathbf{r},t)}{\partial t}, \tag{2.3}$$

$$\nabla \times \mathbf{H}(\mathbf{r},t) = \frac{\partial \mathbf{D}(\mathbf{r},t)}{\partial t}. \tag{2.4}$$

For a nonmagnetic medium we take $\mathbf{B} = \mu_0 \mathbf{H}$. The material response is contained in the electric displacement field

$$\mathbf{D}(\mathbf{r},t) = \varepsilon_0 \mathbf{E}(\mathbf{r},t) + \mathbf{P}(\mathbf{r},t), \tag{2.5}$$

where $\mathbf{P}$ is the macroscopic polarization density [12, 24].

Taking the curl of Faraday's law and using the vector identity

$$\nabla \times (\nabla \times \mathbf{E}) = \nabla(\nabla \cdot \mathbf{E}) - \nabla^2 \mathbf{E}, \tag{2.6}$$

we obtain

$$\nabla(\nabla \cdot \mathbf{E}) - \nabla^2 \mathbf{E} = -\mu_0 \frac{\partial}{\partial t} (\nabla \times \mathbf{H}) = -\mu_0 \frac{\partial^2 \mathbf{D}}{\partial t^2}. \tag{2.7}$$

Substituting Eq. (2.5) allows us to obtain

$$\nabla^2 \mathbf{E} - \nabla(\nabla \cdot \mathbf{E}) - \mu_0 \varepsilon_0 \frac{\partial^2 \mathbf{E}}{\partial t^2} = \mu_0 \frac{\partial^2 \mathbf{P}}{\partial t^2}. \tag{2.8}$$

Equation (2.8) shows that the polarization acts as a driving term for the electric field. In a homogeneous medium and for the paraxial scenarios considered later, it is standard to work in a regime where spatial variations of $\nabla \cdot \mathbf{E}$ can be neglected compared to $\nabla^2 \mathbf{E}$, which yields the sourced wave equation [12, 13]

$$\nabla^2 \mathbf{E}(\mathbf{r},t) - \frac{1}{c^2} \frac{\partial^2 \mathbf{E}(\mathbf{r},t)}{\partial t^2} = \mu_0 \frac{\partial^2 \mathbf{P}(\mathbf{r},t)}{\partial t^2}. \tag{2.9}$$

To connect with nonlinear optics, we decompose the polarization into linear and nonlinear parts,

$$\mathbf{P}(\mathbf{r},t) = \mathbf{P}^{(1)}(\mathbf{r},t) + \mathbf{P}^{(\mathrm{NL})}(\mathbf{r},t), \tag{2.10}$$

where $\mathbf{P}^{(1)}$ determines the refractive index and $\mathbf{P}^{(\mathrm{NL})}$ is treated as a perturbative source term responsible for frequency conversion [12, 25]. In particular, a noncentrosymmetric medium admits a second-order nonlinear polarization $\mathbf{P}^{(2)}$, which generates sum- and difference-frequency components and underlies spontaneous and stimulated parametric down-conversion. The next section specifies the $\chi^{(2)}$ expansion used

in this thesis and identifies the frequency-mixing terms relevant to SPDC, StimPDC, and CPDC.

2.2.1 Scope and Approximations

The theoretical development in this chapter relies on a set of standard approximations that are widely used in treatments of three-wave mixing and spontaneous parametric down-conversion. For clarity, these assumptions are collected here.

First, the electromagnetic fields are treated within the paraxial approximation. The interacting fields are assumed to propagate predominantly along a common longitudinal axis, with transverse variations that are slow on the scale of an optical wavelength. Under these conditions, the fields are approximately transverse and longitudinal field components may be neglected. This justifies ignoring spatial variations of $\nabla \cdot \mathbf{E}$ relative to $\nabla^2\mathbf{E}$ when deriving the sourced wave equation from Maxwell's equations [12, 13].

Second, the nonlinear medium is taken to be homogeneous, and dispersion is included only through the refractive indices that determine the phase-matching condition. This means that linear birefringence and any field-polarization dependence of $\chi^{(2)}$ beyond the choice of a single effective scalar coupling are not modelled explicitly: each field is assigned a fixed polarization at the outset, so the tensor structure of $\chi^{(2)}$ reduces to an overall efficiency factor that does not affect the spatial-mode analysis. Spatial dispersion of the nonlinear susceptibility and nonlocal response effects are neglected. The polarization response is assumed to be instantaneous on the timescales of interest, allowing the use of a frequency-independent $\chi^{(2)}$ tensor [25].

Third, the pump field is treated as a classical, undepleted field with fixed amplitude and spatial profile. This undepleted-pump approximation is valid in the low-conversion-efficiency regime relevant to spontaneous and weakly stimulated down-conversion, and it leads to an interaction Hamiltonian that contains no pump operators [12, 22].

Fourth, the evolution of the quantum state is treated perturbatively and truncated at first order in the interaction Hamiltonian. This low-gain approximation restricts the analysis to the single-pair component of the output state and neglects higher-order multi-pair contributions. In this regime, time ordering in the evolution operator does not affect the result [22, 26].

Finally, rapidly oscillating, non–energy-conserving terms in the interaction Hamiltonian are neglected under the rotating-wave approximation. Only terms that annihilate a pump photon and create a signal–idler photon pair are retained. This approximation is implicit in most quantum-optical treatments of $\chi^{(2)}$ interactions and is well justified when the interaction time is long compared to an optical period [27].

Within these assumptions, the theory developed in this chapter captures the essential spatial and modal structure of SPDC, StimPDC, and CPDC while remaining analytically tractable.

2.3 Classical Nonlinear Polarization

The classical response of a dielectric to an applied field provides the starting point for the quantum model developed later. When a medium lacks inversion symmetry, the induced polarization can acquire a second-order contribution. This contribution drives frequency conversion and underlies the processes examined in Chapter 3. The presentation below follows standard formulations of nonlinear polarization [12, 13, 25] and is restricted to the results needed later.

2.3.1 Expansion of the Polarization

In a dielectric driven by an electric field, the macroscopic polarization admits a power-series expansion in the field amplitude,

$$\mathbf{P}(\mathbf{r},t) = \varepsilon_0 \Big[\chi^{(1)} : \mathbf{E}(\mathbf{r},t) + \chi^{(2)} : \mathbf{E}(\mathbf{r},t)\mathbf{E}(\mathbf{r},t) + \chi^{(3)} : \mathbf{E}(\mathbf{r},t)\mathbf{E}(\mathbf{r},t)\mathbf{E}(\mathbf{r},t) + \cdots\Big], \tag{2.11}$$

where $\chi^{(n)}$ denotes the n-th order susceptibility tensor and ":" indicates contraction over the relevant Cartesian indices [12, 13, 25]. This expansion is valid when the response is local and instantaneous on the timescales of interest and when the applied field is sufficiently weak that higher-order terms are negligible [12, 25]. In a medium lacking inversion symmetry, the second-order term is permitted and is responsible for three-wave mixing.

Writing the second-order contribution in components gives

$$P_i^{(2)}(\mathbf{r},t) = \varepsilon_0 \sum_{j,k} \chi_{ijk}^{(2)} E_j(\mathbf{r},t)\, E_k(\mathbf{r},t), \tag{2.12}$$

where $\chi_{ijk}^{(2)}$ is symmetric under interchange of the last two indices when the interacting frequencies are far from material resonances (Kleinman symmetry) [12, 25]. In typical nonlinear crystals used for SPDC, the allowed tensor components are set by the point-group symmetry of the medium, and only a small subset contributes to a given polarization configuration [25, 28].

To make the frequency content explicit, consider a real electric field expressed as a sum of complex monochromatic components,

$$\mathbf{E}(\mathbf{r},t) = \sum_m \Big[\mathbf{E}_m^{(+)}(\mathbf{r})\, e^{-i\omega_m t} + \mathbf{E}_m^{(-)}(\mathbf{r})\, e^{+i\omega_m t}\Big], \qquad \mathbf{E}_m^{(-)} = (\mathbf{E}_m^{(+)})^*. \tag{2.13}$$

Substituting Eq. (2.13) into Eq. (2.12) shows that $P^{(2)}$ contains products of the form $\mathbf{E}_j^{(+)}\mathbf{E}_k^{(+)} e^{-i(\omega_j+\omega_k)t}$ (sum-frequency generation), $\mathbf{E}_j^{(+)}\mathbf{E}_k^{(-)} e^{-i(\omega_j-\omega_k)t}$ (difference-frequency generation), and their complex conjugates [12, 13]. For the down-conversion processes studied in this thesis, the relevant three-wave mixing channel is the one in which a pump component at ω_p drives fields near ω_s and ω_i such that

$$\omega_p \approx \omega_s + \omega_i, \tag{2.14}$$

with the approximation becoming exact in the infinite-time limit and broadened to a finite bandwidth in realistic experiments [12, 13].

2.3.2 Tensor Structure of $\chi^{(2)}$

The structure of $\chi^{(2)}$ is set by the point-group symmetry of the medium. Many tensor components vanish under these symmetry constraints [25, 28]. In typical SPDC crystals only a small subset contributes, and the interaction can be treated with an effective scalar coefficient.

In this thesis each field maintains a fixed polarization chosen to isolate a single dominant nonlinear coupling. Under these conditions the tensor structure contributes only an overall efficiency factor and does not affect the spatial-mode structure developed later.

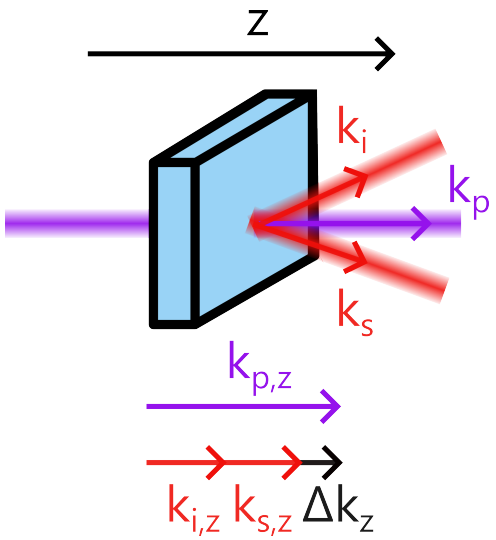


FIGURE 2.1: Wave-vector geometry for three-wave mixing in a $\chi^{(2)}$ crystal. The pump wave vector $\mathbf{k}_p$ decomposes into the signal and idler wave vectors. The lower panel shows the longitudinal components, and the small mismatch Δk_z between $k_{p,z}$ and $k_{i,z} + k_{s,z}$ reduces the conversion efficiency and sets the phase-matching envelope.

2.3.3 Phase Matching and Energy Conservation

The temporal dependence of the nonlinear polarization enforces

$$\omega_p = \omega_s + \omega_i. \tag{2.15}$$

The spatial dependence determines the wave-vector relations inside the medium. Efficient generation occurs when

$$\mathbf{k}_p = \mathbf{k}_s + \mathbf{k}_i, \tag{2.16}$$

with only a small mismatch arising from dispersion or birefringence as depicted in Fig. 2.1. In the upper part of this figure the pump enters the nonlinear crystal and generates signal and idler fields that exit at small angles to the pump direction. The geometry emphasizes that the three wave vectors add vectorially inside the medium. The lower part of the figure extracts the longitudinal components $k_{p,z}$, $k_{i,z}$, and $k_{s,z}$, and identifies the residual mismatch Δk_z between $k_{p,z}$ and the sum $k_{i,z} + k_{s,z}$. This mismatch governs the phase-matching envelope that appears in the overlap integral for the biphoton amplitude and limits the range of spatial modes that are efficiently generated. The condition $\Delta k_z \approx 0$, and its geometric interpretation, are well established in treatments of three-wave mixing [12, 13, 29].

2.3.4 Undepleted-Pump Approximation

The pump field is treated as a classical field with fixed amplitude. This approximation holds when the conversion efficiency is low and is standard in analyses of three-wave mixing [12]. In the quantum description it appears in the absence of pump operators in the interaction Hamiltonian [22].

The field is written as

$$\mathbf{E}(\mathbf{r}, t) = \mathbf{E}_p(\mathbf{r}, t) + \hat{\mathbf{E}}_s(\mathbf{r}, t) + \hat{\mathbf{E}}_i(\mathbf{r}, t), \tag{2.17}$$

with only the signal and idler fields quantized. The pump takes the form

$$\mathbf{E}_p(\mathbf{r},t) = \mathcal{E}_p(\mathbf{r})e^{-i\omega_p t} + \text{c.c.}, \tag{2.18}$$

and does not evolve significantly along the crystal. This approximation simplifies the interaction Hamiltonian in Section 2.4.3 and is valid throughout the scenarios studied in this thesis.

2.4 Quantized Electromagnetic Field

The description of spontaneous and stimulated parametric processes requires a quantum treatment of the electromagnetic field. In this section the field is quantized in a mode expansion appropriate for paraxial propagation in a dielectric medium. The presentation follows standard canonical formulations of quantum electrodynamics in dispersive media [22, 26, 27], with emphasis on the elements needed to construct the $\chi^{(2)}$ interaction Hamiltonian and the biphoton state used in later chapters.

2.4.1 Mode Expansion and Ladder Operators

The quantized electromagnetic field is expanded in a complete set of orthonormal spatial modes. This expansion provides a basis in which creation and annihilation operators act on well-defined transverse states of the field. The mode functions are taken to be solutions of the source-free Helmholtz equation in the nonlinear medium, subject to appropriate boundary conditions, and form a complete basis for the field degrees of freedom [22, 26].

The positive-frequency component of the electric field operator is written as

$$\hat{\mathbf{E}}^{(+)}(\mathbf{r},t) = \sum_{\mu} \mathcal{E}_\mu \, \hat{a}_\mu \, u_\mu(\mathbf{r}) \, e^{-i\omega_\mu t}, \tag{2.19}$$

where the index μ labels the spatial mode and frequency. The mode functions satisfy the orthonormality condition

$$\int d^3r \, u_\mu(\mathbf{r}) \, u_\nu^*(\mathbf{r}) = \delta_{\mu\nu}, \tag{2.20}$$

and completeness ensures that the field operator can be reconstructed uniquely from this expansion.

The prefactors $\mathcal{E}_\mu$ are fixed by canonical quantization and ensure that each excitation of mode μ carries an energy $\hbar\omega_\mu$. In free space or weakly guiding dielectrics one has

$$\mathcal{E}_\mu = \sqrt{\frac{\hbar\omega_\mu}{2\varepsilon_0}}, \tag{2.21}$$

up to refractive-index factors [22, 27]. Their explicit form will not be required in what follows, since only relative spatial amplitudes enter the overlap integrals that define the nonlinear coupling.

The operators $\hat{a}_\mu$ and $\hat{a}_\mu^\dagger$ obey the canonical bosonic commutation relations

$$[\hat{a}_\mu, \hat{a}_\nu^\dagger] = \delta_{\mu\nu}, \tag{2.22}$$

with all other commutators vanishing. The multimode vacuum state $|0\rangle$ is defined by

$$\hat{a}_\mu|0\rangle = 0 \qquad \forall\, \mu. \tag{2.23}$$

The negative-frequency component of the field operator is the Hermitian conjugate of the positive-frequency component, and the full electric field operator is

$$\hat{\mathbf{E}}(\mathbf{r},t) = \hat{\mathbf{E}}^{(+)}(\mathbf{r},t) + \hat{\mathbf{E}}^{(-)}(\mathbf{r},t). \tag{2.24}$$

This representation provides the structure needed for constructing the interaction Hamiltonian in Section 2.4.3 and for defining the biphoton amplitude in Section 2.5.

2.4.2 Positive and Negative Frequency Components

The decomposition of the field operator into positive- and negative-frequency components is a standard element of field quantization and plays a central role in light-matter interactions [22, 26, 27]. The positive-frequency component contains annihilation operators and corresponds to processes in which field quanta are absorbed, while the negative-frequency component contains creation operators and corresponds to emission processes.

Given the mode expansion in Section 2.4.1, the positive-frequency component is

$$\hat{\mathbf{E}}^{(+)}(\mathbf{r},t) = \sum_{\mu} \mathcal{E}_\mu \, \hat{a}_\mu \, u_\mu(\mathbf{r}) \, e^{-i\omega_\mu t}, \tag{2.25}$$

and the negative-frequency component follows as

$$\hat{\mathbf{E}}^{(-)}(\mathbf{r},t) = \left[\hat{\mathbf{E}}^{(+)}(\mathbf{r},t)\right]^\dagger = \sum_{\mu} \mathcal{E}_\mu \, \hat{a}_\mu^\dagger \, u_\mu^*(\mathbf{r}) \, e^{+i\omega_\mu t}. \tag{2.26}$$

This separation is essential when constructing the nonlinear interaction Hamiltonian. Under the rotating-wave approximation, only products of positive-frequency pump fields and negative-frequency signal and idler fields contribute appreciably to the interaction, while rapidly oscillating non-energy-conserving terms average to zero upon time integration [22, 25]. This structure is exploited explicitly in Section 2.4.3.

2.4.3 Quantized Interaction Hamiltonian for $\chi^{(2)}$

The interaction between the quantized electromagnetic field and a second-order nonlinear medium follows from the nonlinear polarization. In the electric-dipole approximation, the interaction Hamiltonian is

$$\hat{H}_{\text{int}} = -\int d^3r \, \hat{\mathbf{P}}^{(2)}(\mathbf{r},t) \cdot \hat{\mathbf{E}}(\mathbf{r},t), \tag{2.27}$$

a form that appears in standard treatments of nonlinear quantum optics [22, 26, 27].

In deriving this Hamiltonian, several approximations are assumed: the response is local in space, spatial dispersion of $\chi^{(2)}$ is neglected, and the rotating-wave approximation is applied to retain only energy-conserving terms. The pump field is treated classically under the undepleted-pump approximation, while the signal and idler fields remain quantized.

Retaining only the terms that annihilate one pump photon and create a signal-idler photon pair, we obtain

$$\hat{H}_{\text{int}} = \varepsilon_0 \int d^3r \, \chi^{(2)} \, E_p^{(+)}(\mathbf{r},t) \, \hat{E}_i^{(-)}(\mathbf{r},t) \, \hat{E}_s^{(-)}(\mathbf{r},t) + \text{h.c.}, \tag{2.28}$$

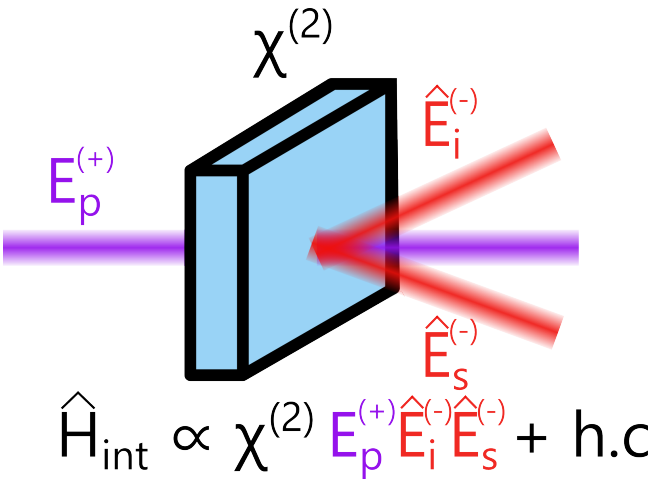


FIGURE 2.2: Schematic of the $\chi^{(2)}$ interaction. A classical pump field drives the creation of a signal-idler photon pair. The positive-frequency component of the pump couples to the negative-frequency components of the quantized fields, corresponding to the creation operators in Eq. (2.28).

where all fields are taken to have fixed polarizations and $\chi^{(2)}$ denotes the effective scalar nonlinearity for the chosen configuration. Terms oscillating at frequencies far from resonance vanish upon time integration over intervals long compared to the optical period.

Substituting the mode expansions from Sections 2.4.1 and 2.4.2 gives

$$\hat{H}_{\text{int}} = \sum_{\mu_i,\mu_s} \kappa_{\mu_i,\mu_s}\, \hat{a}^\dagger_{\mu_i} \hat{a}^\dagger_{\mu_s}\, e^{i(\omega_i+\omega_s-\omega_p)t} + \text{h.c.}, \tag{2.29}$$

with coupling coefficient

$$\kappa_{\mu_i,\mu_s} = \varepsilon_0 \int d^3r\, \chi^{(2)}\, \mathcal{E}_p(\mathbf{r})\, u^*_{\mu_i}(\mathbf{r})\, u^*_{\mu_s}(\mathbf{r})\, e^{i\Delta k z}. \tag{2.30}$$

The exponential contains the longitudinal phase mismatch $\Delta k = k_p - k_s - k_i$ introduced in Section 2.3.3. The transverse structure of this overlap integral determines the spatial correlations and mode structure of the generated photon pairs.

The Hamiltonian in Eq. (2.29) forms the basis for the perturbative derivation of the SPDC biphoton state in Section 2.5. The same operator structure also governs the seeded interactions examined in Chapter 3.

2.5 First-Order Solution and the Biphoton State

2.5.1 Perturbative Evolution

The evolution of the quantum state in a nonlinear medium is governed by the unitary time-evolution operator

$$\hat{U}(t) = \mathcal{T} \exp\left[-\frac{i}{\hbar}\int_0^t \hat{H}_{\text{int}}(t')\, dt'\right], \tag{2.31}$$

where $\hat{H}_{\text{int}}$ is the interaction Hamiltonian given in Eq. (2.29) and $\mathcal{T}$ denotes the time-ordering operator. This formulation is standard in time-dependent perturbation theory and quantum optics [22, 26].

In the low-gain regime relevant for SPDC, the probability of generating more than one photon pair within the interaction time is negligible [30]. Under this condition, the evolution operator may be expanded perturbatively and truncated at first order,

$$\hat{U}(t) \approx \mathbb{I} - \frac{i}{\hbar} \int_0^t \hat{H}_{\text{int}}(t')\, dt'. \tag{2.32}$$

At this order, the time-ordering operator has no effect, since only a single time integral appears [22, 27]. Higher-order terms, which would account for multiple-pair generation and pump depletion, are neglected throughout this thesis.

Assuming the initial state of the signal and idler fields is the multimode vacuum $|0\rangle$, the state after interaction time t is

$$|\Psi(t)\rangle \approx |0\rangle - \frac{i}{\hbar} \int_0^t dt'\, \hat{H}_{\text{int}}(t')\, |0\rangle. \tag{2.33}$$

Only the part of the Hamiltonian containing two creation operators contributes to this expression, since all terms involving annihilation operators acting on the vacuum vanish identically.

Substituting Eq. (2.29) into Eq. (2.33) gives

$$|\Psi(t)\rangle \approx |0\rangle - \frac{i}{\hbar} \sum_{\mu_i,\mu_s} \kappa_{\mu_i,\mu_s} \hat{a}^\dagger_{\mu_i} \hat{a}^\dagger_{\mu_s} \int_0^t e^{i(\omega_i+\omega_s-\omega_p)t'}\, dt'\, |0\rangle. \tag{2.34}$$

The time integral produces a frequency-selection function centered at $\omega_i+\omega_s = \omega_p$. In the limit where the interaction time t is long compared to the optical period, this function approaches

$$\int_0^t e^{i(\omega_i+\omega_s-\omega_p)t'}\, dt' \;\to\; 2\pi\, \delta(\omega_i + \omega_s - \omega_p), \tag{2.35}$$

which enforces energy conservation in the three-wave mixing process [13, 22]. It is worth clarifying the origin of the sinc function that replaces this delta function for a crystal of finite length L. The delta function here arises from the temporal integral over the interaction time and enforces energy conservation $\omega_i + \omega_s = \omega_p$; it is not the same as the phase-matching sinc. The sinc envelope familiar from phase-matching analyses instead arises from the spatial integral of $e^{i\Delta k z}$ over the finite crystal length, which yields $L\,\text{sinc}(\Delta k L/2)$. In a finite crystal both effects are present: the temporal integral broadens the energy-conservation delta function into a narrow sinc in frequency, while the spatial integral independently produces a sinc in Δk that limits the range of efficiently phase-matched spatial modes. Neither sinc modifies the transverse-mode selection rules derived below, for two reasons. First, the longitudinal phase-mismatch sinc depends only on Δk_z and is independent of the transverse coordinates, so it acts as a scalar weighting factor on the transverse overlap integrals without modifying their angular or radial structure. Second, in the paraxial and near-degenerate regime considered here, the phase-matching bandwidth is narrow compared to the scale over which the transverse mode functions vary [20]. Consequently, both finite-crystal corrections modify the overall generation efficiency and spectral bandwidth but leave

the spatial-mode structure of the biphoton amplitude unchanged, and the infinite-crystal approximation captures the essential spatial physics relevant to the LG mode decomposition used throughout this thesis.

Using Eq. (2.35), the state may be written as

$$|\Psi(t)\rangle \approx |0\rangle + \sum_{\mu_i,\mu_s} \Phi_{\mu_i,\mu_s}\, \hat{a}^\dagger_{\mu_i} \hat{a}^\dagger_{\mu_s} |0\rangle, \tag{2.36}$$

where the biphoton amplitude is

$$\Phi_{\mu_i,\mu_s} = -\frac{i}{\hbar}\, 2\pi\, \kappa_{\mu_i,\mu_s}\, \delta(\omega_i + \omega_s - \omega_p). \tag{2.37}$$

Equation (2.36) represents the leading-order two-photon component of the SPDC output state. Its structure encodes both the spatial-mode overlap and the phase-matching constraints imposed by the nonlinear medium. These features are examined in detail in the following subsections.

2.5.2 Two-Photon Component of the State

The first-order perturbative evolution produces the two-photon component of the output state,

$$|\Psi\rangle = |0\rangle + \sum_{\mu_i,\mu_s} \Phi_{\mu_i,\mu_s}\, \hat{a}^\dagger_{\mu_i} \hat{a}^\dagger_{\mu_s} |0\rangle, \tag{2.38}$$

where Φ_{μ_i,μ_s} is the biphoton probability amplitude. This amplitude determines the probability amplitude for creating one photon in idler mode μ_i together with one photon in signal mode μ_s.

To make the spatial structure explicit, the mode indices are expressed in the LG basis introduced in Section 2.6. Writing $\mu \equiv (\ell, p)$, the state becomes

$$|\Psi\rangle = |0\rangle + \sum_{\ell_i,p_i} \sum_{\ell_s,p_s} \Phi_{\ell_i,p_i;\ell_s,p_s}\, \hat{a}^\dagger_{\ell_i,p_i} \hat{a}^\dagger_{\ell_s,p_s} |0\rangle. \tag{2.39}$$

The coefficients $\Phi_{\ell_i,p_i;\ell_s,p_s}$ encode the full transverse-mode correlations of the photon pair.

As shown in Section 2.5.1, these coefficients are proportional to the spatial overlap integral

$$\Phi_{\ell_i,p_i;\ell_s,p_s} \propto \int d^3r\, \mathcal{E}_p(\mathbf{r})\, u^*_{\ell_i,p_i}(\mathbf{r})\, u^*_{\ell_s,p_s}(\mathbf{r})\, e^{i\Delta k z}, \tag{2.40}$$

together with the longitudinal phase-matching envelope enforcing energy conservation. The structure of this overlap integral determines which combinations of azimuthal and radial indices are populated in the down-converted field.

Equation (2.39) provides a complete mode-resolved description of the SPDC output in the low-gain regime and forms the starting point for interpreting the OAM correlations of the photon pair.

2.5.3 Interpretation of the Biphoton Amplitude

The biphoton amplitude $\Phi_{\ell_i,p_i;\ell_s,p_s}$ determines the joint probability amplitudes for generating photon pairs in specific transverse modes. The probability of detecting an idler photon in mode (ℓ_i, p_i) and a signal photon in mode (ℓ_s, p_s) is proportional to

$$P_{\ell_i,p_i;\ell_s,p_s} \propto \left|\Phi_{\ell_i,p_i;\ell_s,p_s}\right|^2. \tag{2.41}$$

As a result, the spatial correlations of the down-converted photons are fully encoded in the structure of $\Phi_{\ell_i,p_i;\ell_s,p_s}$ [31].

In the context of orbital angular momentum, these coefficients are commonly interpreted in terms of the spiral spectrum of SPDC [31, 32, 33]. In this formalism, the LG-resolved biphoton amplitude obtained above is identified directly with the spiral-spectrum coefficients,

$$C_{\ell_i,\ell_s}^{p_i,p_s} \equiv \Phi_{\ell_i,p_i;\ell_s,p_s}, \tag{2.42}$$

up to normalization conventions. The spiral spectrum is then defined as the joint OAM probability distribution

$$P_{\ell_i,\ell_s}^{p_i,p_s} = |\Phi_{\ell_i,p_i;\ell_s,p_s}|^2 . \tag{2.43}$$

For a Gaussian pump beam carrying zero orbital angular momentum, the azimuthal dependence of the overlap integral in Eq. (2.40) enforces the selection rule

$$\ell_i + \ell_s = 0, \tag{2.44}$$

so that the spiral spectrum is concentrated along the anti-diagonal in (ℓ_i, ℓ_s) space. The width of this distribution, often referred to as the spiral bandwidth, is governed by the pump waist, the crystal length, and the phase-matching conditions [31]. A broader spiral spectrum corresponds to higher-dimensional OAM entanglement.

Importantly, the spiral-spectrum coefficients are determined by the same spatial overlap integrals that appear in the interaction Hamiltonian. As a result, the quantities introduced here are not specific to spontaneous down-conversion. The same coefficients govern the coupling strength in stimulated and cascaded processes, where a single photon or classical field seeds the nonlinear interaction. This connection will be exploited in later chapters to analyse StimPDC and CPDC, where the transfer and conjugation of OAM are determined by the structure of $\Phi_{\ell_i,p_i;\ell_s,p_s}$.

2.6 LG Basis and Spatial Structure of the SPDC State

The transverse spatial modes of the optical fields are expressed in the LG basis, which provides a complete and orthonormal set of solutions to the paraxial wave equation and is widely used in analyses of spatial-mode structure in nonlinear and quantum optics [23, 34]. Each LG mode is labeled by an azimuthal index $\ell \in \mathbb{Z}$ and a radial index $p \geq 0$. At the plane of the nonlinear crystal, the normalized transverse mode function may be written as

$$u_{\ell,p}(r,\phi) = \sqrt{\frac{2\,p!}{\pi\,(p+|\ell|)!}}\,\frac{1}{w}\left(\frac{\sqrt{2}r}{w}\right)^{|\ell|} L_p^{|\ell|}\left(\frac{2r^2}{w^2}\right) e^{-\frac{r^2}{w^2}} e^{i\ell\phi}, \tag{2.45}$$

where w is the beam waist and $L_p^{|\ell|}$ is the generalized Laguerre polynomial.

These modes satisfy the orthonormality relation

$$\int d^2r_\perp\, u_{\ell,p}(r,\phi)\, u^*_{\ell',p'}(r,\phi) = \delta_{\ell,\ell'}\,\delta_{p,p'}, \tag{2.46}$$

and form a complete basis for paraxial transverse fields. An equivalent orthonormality holds in transverse momentum space, reflecting the fact that LG modes are eigenfunctions of the Fourier transform up to a scale factor [22].

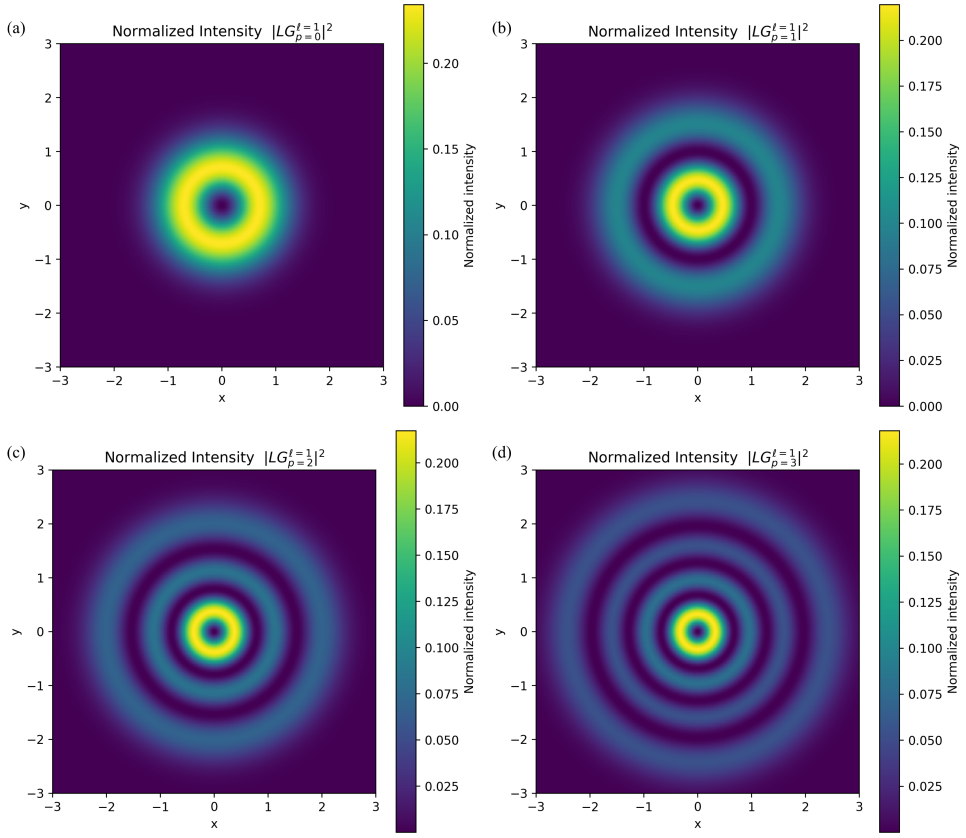


FIGURE 2.3: Normalized intensity profiles of LG modes with fixed azimuthal index $\ell = 1$ and increasing radial index p. The redistribution of intensity with increasing p alters the spatial overlap with the pump field and hence the magnitude of the nonlinear coupling coefficients.

Figure 1.1 illustrates representative LG intensity and phase profiles. Modes with $\ell \neq 0$ exhibit a helical azimuthal phase dependence $e^{i\ell\phi}$ and a central phase singularity, corresponding to an orbital angular momentum of $\ell\hbar$ per photon. Increasing the radial index p introduces additional radial nodes, redistributing the transverse intensity without altering the OAM content of the mode.

In many practical situations, including those considered in this thesis, the azimuthal structure is of primary interest since there is no equivalent conservation relation for the radial indices. Figure 2.3 shows the normalized intensity profiles for modes with $\ell = 1$ and increasing p. As p increases, additional radial rings appear and the intensity shifts outward from the beam center. These changes directly affect the spatial overlap with a given pump profile and therefore modify the strength of nonlinear coupling.

The spatial dependence of the SPDC interaction is captured by the mode-resolved overlap integral

$$\kappa_{\ell_i,p_i;\,\ell_s,p_s} \propto \int d^3r\, \mathcal{E}_p(\mathbf{r})\, u^*_{\ell_i,p_i}(\mathbf{r})\, u^*_{\ell_s,p_s}(\mathbf{r})\, e^{i\Delta kz}, \tag{2.47}$$

which combines the transverse pump profile, the signal and idler mode functions, and the longitudinal phase-matching factor. The angular dependence of the LG modes

enforces the orbital-angular-momentum selection rule

$$\ell_i + \ell_s = \ell_p, \tag{2.48}$$

where ℓ_p is the OAM of the pump field. In this thesis the pump is taken to be Gaussian, so $\ell_p = 0$ and consequently

$$\ell_i = -\ell_s. \tag{2.49}$$

While the azimuthal indices are constrained by rotational symmetry, the radial indices (p_i, p_s) remain unconstrained by Eq. (2.48). Their contribution enters through the Laguerre polynomial factors in Eq. (2.47) and through the finite transverse extent of the pump and crystal. These radial weights depend on experimental parameters such as the pump waist, crystal length, and phase-matching bandwidth.

The resulting biphoton amplitude $\Phi_{\ell_i,p_i;\ell_s,p_s}$ therefore directly encodes the joint spatial-mode structure of the photon pair. When summed over the radial indices, its dependence on the azimuthal indices defines the spiral spectrum, which quantifies the distribution of OAM in the SPDC state [31]. In this sense, the overlap integral in Eq. (2.47) provides the microscopic origin of the spiral spectrum discussed in the literature.

This LG-mode description is central to the analysis of cascaded processes in Chapter 4. In CPDC, a photon drawn from the SPDC state acts as a seed for a second $\chi^{(2)}$ interaction, and the coupling between the seed and the generated idler is governed by the same spatial overlap structure. As a result, the (ℓ, p) composition of the SPDC state directly determines how phase and OAM are transferred in the cascaded interaction.

2.7 Summary

This chapter developed the theoretical framework underlying stimulated and cascaded parametric down-conversion. Beginning from the classical description of the second-order nonlinear polarization, the conditions for three-wave mixing were established through energy conservation and phase matching. Under the undepleted-pump approximation, these considerations led naturally to a quantized interaction Hamiltonian in which the pump is treated classically and the signal and idler fields are described by bosonic operators.

Using first-order perturbation theory in the low-gain regime, the two-photon component of the SPDC output state was derived explicitly. The resulting biphoton amplitude encodes the full spatial and modal structure of the photon pairs generated in the nonlinear medium. Its dependence on overlap integrals between the pump field and the transverse mode functions of the signal and idler fields determines the correlations observed in joint detection measurements.

To analyse this structure in a transparent way, the transverse modes were expressed in the LG basis. In this representation, conservation of OAM follows directly from the azimuthal dependence of the overlap integrals, while the radial indices control the weighting of the down-converted modes through their radial profiles. These features were illustrated through representative mode structures and form the basis for understanding how spatial information is distributed across the biphoton state.

The results of this chapter provide the foundation for the analysis of seeded $\chi^{(2)}$ processes. In StimPDC and CPDC, a photon originating from the SPDC biphoton

state serves as a seed for a subsequent nonlinear interaction, and the same spatial-overlap structure derived here governs the coupling between the seed and the generated idler field. The mode-resolved biphoton amplitude introduced in this chapter therefore serves as the central theoretical object connecting spontaneous, stimulated, and cascaded down-conversion throughout the remainder of the thesis.

Chapter 3

Stimulated Parametric Down-Conversion and Classical Phase Conjugation

3.1 Introduction

StimPDC provides a practical method for transferring spatial structure between optical fields in a $\chi^{(2)}$ medium. When one of the down-converted modes is seeded, the generated idler acquires a transverse profile proportional to the product $E_p E_s^*$, linking the idler to both the pump structure and the conjugated seed. This behaviour has been used to study spatial-mode transfer in nonlinear optics and to implement wavefront-correction schemes based on phase conjugation [16, 35].

The first set of results relevant to this thesis appears in my coauthored study [16] (found in Section 1 of the Appendix), which mapped how the StimPDC response depends on pump structure, seed OAM, radial content, and waist ratio. The measurements confirmed that the idler reproduces the azimuthal and radial features of the seed with high fidelity whenever the spatial overlap with the pump is maximized. These observations establish the classical StimPDC interaction as a precise and controllable tool for shaping structured light.

A second application, developed in [15], a work for which I am a contributing co-author, used the same phase-conjugating response to correct turbulence-induced distortions in free-space channels. A probe beam sent from Bob to Alice acquires a random spatial phase while passing through turbulence. Inside Alice's crystal, the distorted probe overlaps with an information-bearing pump, and the generated idler inherits the pump mode together with the conjugated turbulence phase. After propagating back through the same channel, the returning field reproduces the pump mode with the distortion removed.

These classical results raise a natural question for quantum communication. If the probe were replaced by a single photon, the turbulence-mitigation geometry would become compatible with quantum key distribution and inherit its security guarantees [36]. Whether this extension is feasible depends on what "phase conjugation" means in the single-photon regime and on whether a physical interaction can implement the required transformation on a quantum spatial state. To separate these issues, this chapter first develops the classical theory that leads to $E_i \propto E_p E_s^*$, then presents the turbulence-cancellation mechanism in that mean-field setting. It then reformulates the same cancellation at the level of single-photon probability amplitudes, which clarifies what must be achieved in the quantum regime.

The remainder of the thesis addresses the physical mechanism. Chapter 4 treats the $\chi^{(2)}$ interaction with a single-photon seed at the level of quantum states and

correlations, and quantifies the extent to which phase-conjugated behaviour persists beyond the classical product description.

3.1.1 Interaction Hamiltonian with a Classical Seed

The starting point for classical stimulated parametric down-conversion is the $\chi^{(2)}$ interaction Hamiltonian introduced in Chapter 2,

$$\hat{H}_{\text{int}} = \varepsilon_0 \int d^3r\, \chi^{(2)}\, E_p^{(+)}(\mathbf{r},t)\, \hat{E}_i^{(-)}(\mathbf{r},t)\, \hat{E}_s^{(-)}(\mathbf{r},t) + \text{h.c.}, \tag{3.1}$$

which describes the three-wave mixing process driven by the second-order nonlinear polarization.

In the stimulated regime, the signal field is seeded by a bright classical beam. Its positive- and negative-frequency components are therefore treated as complex functions rather than operators. The pump field is likewise treated classically under the undepleted-pump approximation, while the idler field remains quantized. Replacing $\hat{E}_s^{(-)}$ by the classical field $E_s^{(-)}$ yields

$$\hat{H}_{\text{int}} = \varepsilon_0 \int d^3r\, \chi^{(2)}\, E_p^{(+)}(\mathbf{r},t)\, E_s^{(-)}(\mathbf{r},t)\, \hat{E}_i^{(-)}(\mathbf{r},t) + \text{h.c.}. \tag{3.2}$$

When this Hamiltonian acts on the idler vacuum, only the terms that create an idler photon contribute to the evolution. Using the mode expansion [37]

$$\hat{E}_i^{(-)}(\mathbf{r},t) = \sum_{\mu_i} \mathcal{E}_{\mu_i}\, u_{\mu_i}^*(\mathbf{r})\, \hat{a}_{\mu_i}^\dagger e^{i\omega_i t}, \tag{3.3}$$

and substituting the classical pump and seed fields, the interaction Hamiltonian reduces to

$$\hat{H}_{\text{int}} = \sum_{\mu_i} \Lambda_{\mu_i}\, \hat{a}_{\mu_i}^\dagger\, e^{i(\omega_i - \omega_p + \omega_s)t} + \text{h.c.}, \tag{3.4}$$

where the coupling coefficient is

$$\Lambda_{\mu_i} = \varepsilon_0 \int d^3r\, \chi^{(2)}\, \mathcal{E}_{\mu_i}\, E_p^{(+)}(\mathbf{r})\, E_s^{(-)}(\mathbf{r})\, u_{\mu_i}^*(\mathbf{r})\, e^{i\Delta k z}. \tag{3.5}$$

Equation (3.5) shows explicitly that the probability amplitude for generating an idler photon in mode μ_i is governed by the spatial product $E_p E_s^*$ inside the nonlinear medium. This operator-level result already encodes the key feature of classical StimPDC: the idler field is sourced by the pump profile multiplied by the complex conjugate of the seed field. The physical implications of this structure for wave propagation and phase conjugation are made explicit in the field-level treatment that follows, and are illustrated schematically in Fig. 3.1.

3.1.2 Field-Level Description of StimPDC

While the interaction Hamiltonian reveals the origin of the coupling between pump, seed, and idler modes, the phase-conjugation behaviour of classical StimPDC is most transparently derived at the level of the driven wave equation. This approach makes explicit the assumptions under which the idler inherits the conjugated spatial structure of the seed and provides a direct link to the turbulence-mitigation protocol discussed later in this chapter.

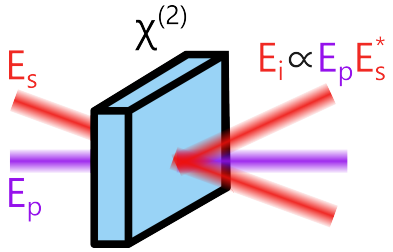


FIGURE 3.1: Stimulated parametric down-conversion in a $\chi^{(2)}$ crystal. A classical seed field E_s and a pump field E_p overlap inside the nonlinear medium. The nonlinear polarization driven by their product generates an idler field whose transverse structure is proportional to $E_p E_s^*$. This geometry provides an intuitive picture of the spatial overlap that appears analytically in the StimPDC interaction Hamiltonian and underlies the phase conjugation behaviour derived in the text.

In a homogeneous, nonmagnetic medium, the idler field satisfies the sourced wave equation

$$\nabla^2 E_i(\mathbf{r},t) - \frac{n_i^2}{c^2}\frac{\partial^2 E_i(\mathbf{r},t)}{\partial t^2} = \frac{1}{\varepsilon_0 c^2}\frac{\partial^2 P_i^{(2)}(\mathbf{r},t)}{\partial t^2}, \tag{3.6}$$

where $P_i^{(2)}$ is the component of the second-order nonlinear polarization oscillating at the idler frequency [12, 13].

Under the undepleted-pump approximation, the pump and seed are prescribed classical fields with slowly varying envelopes,

$$E_p(\mathbf{r},t) = A_p(\mathbf{r})\, e^{-i\omega_p t} + \text{c.c.}, \tag{3.7}$$

$$E_s(\mathbf{r},t) = A_s(\mathbf{r})\, e^{-i\omega_s t} + \text{c.c.}. \tag{3.8}$$

The second-order polarization driving the idler arises from the product of the positive-frequency pump and the negative-frequency seed components,

$$P_i^{(2)}(\mathbf{r},t) = \varepsilon_0 \chi^{(2)} A_p(\mathbf{r})\, A_s^*(\mathbf{r})\, e^{-i\omega_i t} + \text{c.c.}, \tag{3.9}$$

with $\omega_i = \omega_p - \omega_s$ enforcing energy conservation.

Seeking a monochromatic solution

$$E_i(\mathbf{r},t) = A_i(\mathbf{r})\, e^{-i\omega_i t} + \text{c.c.}, \tag{3.10}$$

and substituting into Eq. (3.6) yields the inhomogeneous Helmholtz equation

$$\nabla^2 A_i + k_i^2 A_i = -\, k_i^2 \chi^{(2)} A_p A_s^*, \tag{3.11}$$

where $k_i = n_i \omega_i / c$.

In the paraxial and slowly varying envelope approximations, longitudinal second derivatives are neglected relative to propagation terms [12]. Under near-perfect phase matching, the driven solution of Eq. (3.11) yields an idler envelope proportional to the source term,

$$A_i(\mathbf{r}_\perp, z) \propto A_p(\mathbf{r}_\perp, z)\, A_s^*(\mathbf{r}_\perp, z). \tag{3.12}$$

Equation (3.12) makes explicit the origin of phase conjugation in classical StimPDC. The idler field inherits the transverse amplitude of the pump together with the complex conjugate phase of the seed. If the seed carries a spatial phase $\phi_s(\mathbf{r}_\perp)$, the

idler acquires a phase $-\phi_s(\mathbf{r}_\perp)$, establishing deterministic wavefront reversal. This field-level result is the direct propagation analogue of the overlap structure derived from the interaction Hamiltonian and illustrated schematically in Fig. 3.1.

Crucially, Eq. (3.12) is a mean-field statement: it presumes a seed with a well-defined complex amplitude. When the seeding mode is occupied by a single photon, the mean field amplitude vanishes, so phase conjugation cannot be inferred from the classical product alone. The corresponding quantum mechanism is addressed in Chapter 4.

3.1.3 Dependence on Pump–Seed Waist Ratio and Radial Coupling

The spatial structure of the StimPDC output depends sensitively on the relative beam waists of the pump and seed. This dependence follows directly from the overlap structure of Eq. (3.12). In the LG basis, both fields contain Laguerre polynomial factors whose radial extent is set by their respective waists. The product $E_p(\mathbf{r})E_s^*(\mathbf{r})$ therefore inherits a radial structure that reflects the degree to which the pump and seed profiles overlap within the nonlinear medium.

Experiments in [16] showed that the waist ratio w_p/w_s controls the radial-mode weights of the generated idler. When the waists are matched, the overlap integral is dominated by terms in which the idler radial index p_i equals the seed radial index p_s. In this regime, the stimulated idler reproduces the seed's radial-node structure with high fidelity. As the waist ratio increases above unity, contributions from additional radial indices become significant, and the generated idler exhibits mixing across the p-modes. This behaviour is consistent with standard analyses of spatial-mode coupling in three-wave mixing [12, 13], where radial-mode purity is preserved only when the waists are chosen to maximize the transverse overlap.

The waist ratio also influences the effective support of the nonlinear interaction. A tightly focused seed overlapping with a broad pump produces an idler concentrated near the pump center, while a broad seed combined with a tightly focused pump yields a weaker and more diffuse idler. These effects were mapped quantitatively in [16], where measurements confirmed that both the amplitude and radial structure of the idler depend on the spatial filtering imposed by the pump.

3.2 StimPDC for Turbulence Mitigation

Classical StimPDC has been employed as an effective tool for correcting wavefront distortions in free-space optical channels. The central mechanism is the deterministic relation $E_i \propto E_p E_s^*$, which ensures that the generated idler reproduces the spatial mode of the pump while carrying the conjugated phase of the probe. This property enables a turbulence-mitigation strategy in which a probe sent through a distorted channel acquires a turbulence phase, and its conjugate appears on the idler generated at the receiver. When the idler retraces the same channel in the opposite direction, the accumulated phase cancels the conjugated distortion, allowing the transmitted spatial mode to be recovered. The following subsections summarize the classical implementation of this protocol in my second coauthored publication [15] (found in Section 2 of the Appendix), and illustrate how the geometry of StimPDC enables turbulence correction in practice.

3.2.1 Phase Structure and Information Transfer in the StimPDC Geometry

The spatial structure of the StimPDC output follows directly from the product $E_p(\mathbf{r})E_s^*(\mathbf{r})$ that appears in the nonlinear polarization. This relation not only enforces phase conjugation of the seed, but also enables a deterministic cancellation of propagation-induced phase distortions in reciprocal channels. In this subsection, we make this mechanism explicit for the turbulence-mitigation geometry studied in [15].

In that protocol, the pump and seed fields play asymmetric roles. The seed is a Gaussian probe beam sent from Bob to Alice through a turbulent free-space channel. As it propagates, the probe acquires a spatially varying phase. In the thin-phase-screen approximation, the effect of turbulence can be modeled by a multiplicative transfer function

$$T(\mathbf{r}_\perp) = \exp[i\phi(\mathbf{r}_\perp)], \tag{3.13}$$

which captures the dominant transverse phase distortions for weak-to-moderate scintillation [7, 8].

At Bob, the probe field is taken to be

$$E_s^{(\mathrm{Bob})}(\mathbf{r}_\perp) = E_0(\mathbf{r}_\perp), \tag{3.14}$$

so that after propagation to Alice it becomes

$$E_s^{(\mathrm{Alice})}(\mathbf{r}_\perp) = E_0(\mathbf{r}_\perp)\,\exp[i\phi(\mathbf{r}_\perp)]. \tag{3.15}$$

Alice prepares the pump field in the spatial mode she wishes to transmit,

$$E_p(\mathbf{r}_\perp) = A_p(\mathbf{r}_\perp)\,\exp[i\theta_p(\mathbf{r}_\perp)], \tag{3.16}$$

where both the amplitude and phase encode information. Inside Alice's $\chi^{(2)}$ crystal, the distorted seed and structured pump overlap. As shown in Sec. 3.1.2, the idler generated by classical StimPDC is proportional to the nonlinear source term,

$$E_i^{(\mathrm{Alice})}(\mathbf{r}_\perp) \propto E_p(\mathbf{r}_\perp)\,[E_s^{(\mathrm{Alice})}(\mathbf{r}_\perp)]^*. \tag{3.17}$$

Substituting Eq. (3.15) yields

$$E_i^{(\mathrm{Alice})}(\mathbf{r}_\perp) \propto A_p(\mathbf{r}_\perp)\,\exp[i\theta_p(\mathbf{r}_\perp)]\,\exp[-i\phi(\mathbf{r}_\perp)]. \tag{3.18}$$

The idler therefore carries the spatial mode of the pump together with the conjugated turbulence phase imprinted on the seed.

The idler then propagates back to Bob through the same turbulent channel. Reciprocity implies that backward propagation multiplies the field by the same phase factor $\exp[i\phi(\mathbf{r}_\perp)]$. The field received by Bob is

$$E_i^{(\mathrm{Bob})}(\mathbf{r}_\perp) = E_i^{(\mathrm{Alice})}(\mathbf{r}_\perp)\,\exp[i\phi(\mathbf{r}_\perp)]. \tag{3.19}$$

Using Eq. (3.18), the turbulence phases cancel exactly,

$$E_i^{(\mathrm{Bob})}(\mathbf{r}_\perp) \propto A_p(\mathbf{r}_\perp)\,\exp[i\theta_p(\mathbf{r}_\perp)]. \tag{3.20}$$

Bob therefore receives a field that reproduces the pump mode prepared by Alice, with the turbulence-induced phase distortion fully removed.

This behaviour is illustrated schematically in Fig. 3.2. Bob sends a Gaussian probe through the turbulent channel, and the probe accumulates a distorted phase before reaching Alice. Inside Alice's $\chi^{(2)}$ crystal the distorted probe overlaps with an information-bearing pump field that has been shaped into the spatial mode Alice intends to transmit. The generated idler inherits the pump's spatial structure together with the conjugated turbulence phase carried by the probe. As the idler propagates back to Bob through the same turbulent channel, it acquires the forward turbulence phase, which cancels the conjugated distortion imprinted at Alice. Bob therefore receives a corrected field that reproduces the pump mode.

This cancellation arises from the StimPDC product structure $E_p E_s^*$ together with channel reciprocity, and does not require any explicit estimation of the turbulence. The derivation above is classical: it is formulated in terms of deterministic field amplitudes and uses the mean-field relation in Eq. (3.12). A complementary single-photon formulation, expressed directly in terms of spatial probability amplitudes and unitary propagation through turbulence, is given in Sec. 3.2.5. The remaining physical question is whether a $\chi^{(2)}$ interaction seeded by a single photon can implement the required phase-conjugating map in any operational sense; this issue motivates the quantum analysis in Chapter 4.

3.2.2 Relevant QKD Definitions

Quantum key distribution protocols are commonly analyzed using information-theoretic quantities that quantify correlations between the legitimate parties and any potential eavesdropper. In this subsection we briefly introduce the definitions required later, following standard treatments [17, 18, 38].

Consider two classical random variables A and B, where $A \in \mathcal{A} = \{a_1, \ldots, a_d\}$ represents the symbol Alice selects from a d-ary alphabet and $B \in \mathcal{B}$ represents Bob's corresponding measurement outcome. The Shannon entropy of a discrete random variable A with probability distribution $\{p(a)\}$ is

$$H(A) = -\sum_a p(a)\, \log_2 p(a), \tag{3.21}$$

and the joint entropy of A and B is

$$H(A,B) = -\sum_{a,b} p(a,b)\, \log_2 p(a,b). \tag{3.22}$$

The conditional entropy of A given B is

$$H(A|B) = -\sum_{a,b} p(a,b)\, \log_2 p(a|b). \tag{3.23}$$

The mutual information between Alice and Bob is then

$$I(A{:}B) = H(A) + H(B) - H(A,B) = H(A) - H(A|B), \tag{3.24}$$

which quantifies how much Bob's outcomes reveal about Alice's symbols.

In a prepare-and-measure QKD protocol, Alice encodes a classical symbol $a \in \mathcal{A}$ onto a quantum state ρ_a and transmits it to Bob, who performs a measurement to recover an estimate of a; no entanglement between Alice and Bob is required. The quality of the quantum channel is often characterized by the quantum bit error rate (QBER), defined as the probability that Bob's decoded symbol differs from Alice's

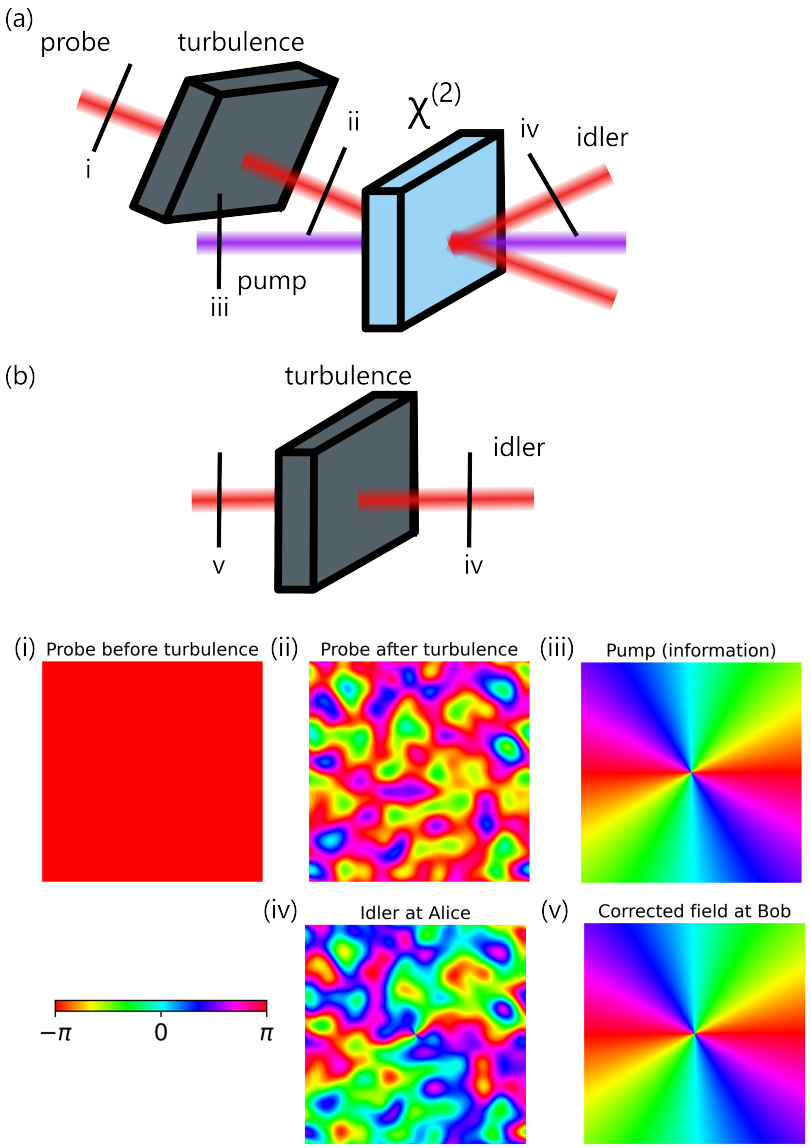


FIGURE 3.2: StimPDC turbulence-mitigation geometry. (a) A Gaussian probe from Bob traverses the turbulent channel left to right and acquires a distorted phase before reaching Alice. Inside Alice's $\chi^{(2)}$ crystal the distorted probe overlaps with an information-bearing pump field shaped in the desired spatial mode. The generated idler carries the pump mode together with the conjugated turbulence distortion. (b) The idler propagates back through the same turbulent channel from right to left, so that the accumulated phase cancels the conjugated distortion and Bob receives a corrected spatial mode at position v. Insets illustrate the phase of the different beams at the labelled positions.

prepared symbol. For binary alphabets with symmetric errors, $I(A:B)$ is a monotonically decreasing function of the QBER and vanishes when the error rate reaches 50%.

Security requires that Bob's information about Alice's symbols exceeds that available to an eavesdropper Eve. Classically, this condition is expressed as

$$I(A{:}B) > I(A{:}E), \tag{3.25}$$

which ensures that privacy amplification can distill a secret key. In a full quantum treatment, Eve's accessible information is bounded by the Holevo quantity

$$\chi(A{:}E) = S(\rho_E) - \sum_a p(a)\, S(\rho_E^{(a)}), \tag{3.26}$$

where $S(\rho) = -\mathrm{Tr}(\rho \log_2 \rho)$ is the von Neumann entropy, ρ_E is Eve's average quantum state, and $\rho_E^{(a)}$ is Eve's state conditioned on Alice sending symbol a [17]. In this context, $I(A{:}E)$ in Eq. (3.25) should be understood as this effective bound.

A positive secret-key rate is achievable only when Alice and Bob's mutual information exceeds Eve's accessible information. The role of turbulence mitigation in OAM-based QKD is therefore to reduce the QBER and thereby increase $I(A:B)$ without simultaneously increasing Eve's information.

3.2.3 QKD Implementation in the Turbulence-Mitigation Experiment

The turbulence-mitigation experiment reported in [15] demonstrated that stimulated parametric down-conversion can reverse phase distortions acquired during free-space propagation. Although the experiment was performed entirely in the classical regime, its geometry closely resembles a prepare-and-measure communication protocol and therefore provides a useful reference point for assessing whether phase conjugation could be incorporated into quantum key distribution.

Operationally, Bob prepares a probe beam and sends it through a turbulent channel to Alice. The probe acquires a spatially varying phase that degrades its modal purity. At Alice, the distorted probe overlaps inside a $\chi^{(2)}$ crystal with a structured pump field that encodes the information Alice wishes to transmit. Through StimPDC, the generated idler acquires the pump mode together with the conjugated phase of the probe. When the idler propagates back to Bob through the same channel, the forward turbulence phase cancels the conjugated distortion imprinted at Alice, and Bob receives a field that reproduces the pump mode. As shown in Sec. 3.2.1, this cancellation follows directly from the field-level relation

$$\mathcal{E}_i \propto \mathcal{E}_p\, \mathcal{E}_s^*, \tag{3.27}$$

and does not require any explicit estimation of the turbulence.

From the perspective of QKD, this behavior corresponds to Alice encoding information into a spatial mode and Bob recovering it after a noisy round-trip propagation. In conventional OAM-based QKD, turbulence increases the quantum bit error rate by distorting the transmitted modes [39, 40]. The classical StimPDC experiment therefore establishes that, at the level of wave optics, phase conjugation can suppress this dominant source of error.

The configuration is nevertheless insecure. Both the probe and the pump are classical fields with macroscopic amplitudes, so an eavesdropper can extract information from the channel without introducing detectable disturbance. Eve could split off a fraction of the optical power, perform partial measurements, or inject auxiliary classical fields without violating any fundamental constraint. In this regime, the disturbance-information tradeoff required for QKD does not apply, and Eve's accessible information is not bounded by the no-cloning principle. Consequently, the mutual-information condition for secret-key generation,

$$I(A{:}B) > I(A{:}E), \tag{3.28}$$

cannot be satisfied when Eve has access to classical travelling fields. The classical turbulence-mitigation experiment therefore serves only as a proof of principle for phase correction, not as a secure communication protocol.

3.2.4 Motivation for a Single-Photon Extension

If the turbulence-mitigation protocol were implemented with single photons rather than classical probes, the security of the channel would follow from standard QKD principles. A single photon cannot be copied or measured without introducing disturbance, and any attempt by an eavesdropper to extract information from the forward channel would modify the quantum state detected by Alice and Bob [36, 41]. Extending the protocol to this regime would therefore make the turbulence-corrected channel compatible with QKD.

At a qualitative level, the phase-cancellation mechanism does not rely on the presence of a classical field amplitude. A single photon propagating through a turbulent channel acquires a spatially varying phase in the sense that its wavefunction transforms as

$$\psi(\mathbf{r}_\perp) \to \psi(\mathbf{r}_\perp)\, e^{i\varphi(\mathbf{r}_\perp)}. \tag{3.29}$$

If an operation existed that mapped this state to its phase-conjugated counterpart,

$$\psi(\mathbf{r}_\perp)\, e^{i\varphi(\mathbf{r}_\perp)} \to \psi^*(\mathbf{r}_\perp)\, e^{-i\varphi(\mathbf{r}_\perp)}, \tag{3.30}$$

then a subsequent propagation through the same reciprocal channel would re-impose the forward turbulence phase and restore the original spatial structure. At the level of single-particle wave mechanics, turbulence cancellation is therefore possible provided that genuine phase conjugation can be realized.

The difficulty is that classical StimPDC relies on the presence of a complex seed field to generate the conjugated response. In that regime, the idler amplitude is deterministically proportional to $E_p E_s^*$. A single photon does not supply a classical field amplitude, and the StimPDC interaction must instead be described in terms of quantum operators and expectation values. In particular, the output contains both spontaneous and stimulated contributions whose relative weights depend on the photon number in the seeding mode.

Whether phase conjugation survives in this regime, and in what sense it can be meaningfully defined for single photons, cannot be inferred from the classical theory alone. Addressing this question requires a quantum treatment of the StimPDC interaction with a single-photon seed. This analysis is carried out in Chapter 4, where the structure of the CPDC output state is derived and the extent to which phase-conjugated behaviour persists is examined quantitatively.

3.2.5 Single-Photon Perspective on Turbulence Cancellation

The turbulence-mitigation protocol described above was derived using classical field amplitudes, but the underlying cancellation mechanism can be reformulated at the level of single-photon probability amplitudes. This distinction is essential for assessing whether turbulence correction is compatible with quantum communication.

Consider a single photon propagating through a turbulent free-space channel. In the paraxial regime, the effect of turbulence on the transverse degree of freedom can be modeled as a unitary transformation acting on the photon's spatial wavefunction,

$$\psi(\mathbf{r}_\perp) \longrightarrow (U_{\text{turb}}\psi)(\mathbf{r}_\perp) = \psi(\mathbf{r}_\perp)\, e^{i\varphi(\mathbf{r}_\perp)}, \tag{3.31}$$

where $\varphi(\mathbf{r}_\perp)$ is a random phase imposed by refractive-index fluctuations and provided the turbulence is weak enough that amplitude scintillation is negligible and the channel acts primarily as a phase screen [7, 8]. This transformation does not rely on a classical field amplitude; it acts equally on single-photon and multi-photon states. Note that the turbulent channel is modeled here as purely phase-imprinting and lossless. This approximation, which is standard in the thin-phase-screen regime, neglects intensity-dependent scintillation effects; amplitude fluctuations would reduce the round-trip cancellation fidelity and would need to be accounted for in any practical single-photon implementation.

Suppose now that, after forward propagation through the turbulent channel, an operation is applied that maps the spatial state to its phase-conjugated counterpart,

$$\psi(\mathbf{r}_\perp)\, e^{i\varphi(\mathbf{r}_\perp)} \longrightarrow \psi^*(\mathbf{r}_\perp)\, e^{-i\varphi(\mathbf{r}_\perp)}. \tag{3.32}$$

If the resulting photon propagates backward through the same reciprocal channel, it undergoes the transformation

$$\psi^*(\mathbf{r}_\perp)\, e^{-i\varphi(\mathbf{r}_\perp)} \longrightarrow \psi^*(\mathbf{r}_\perp), \tag{3.33}$$

so that the turbulence-induced phase cancels exactly. The spatial structure of the photon is therefore restored, up to complex conjugation, without any knowledge of the turbulence itself.

This argument shows that turbulence cancellation does not fundamentally rely on classical wave optics. Rather, it depends on three components: (i) unitary and reciprocal propagation through the channel, (ii) an operation that implements phase conjugation of the spatial probability amplitude, and (iii) backward propagation through the same channel. When these conditions are met, phase cancellation is possible even at the single-photon level.

What differs from the classical case is the mechanism by which phase conjugation is realized. Classical StimPDC produces a deterministic conjugated field through the product $E_p E_s^*$. A single photon does not possess a mean field amplitude, so any phase-conjugation mechanism must instead operate on quantum probability amplitudes or higher-order correlations. Whether stimulated parametric down-conversion provides such a mechanism when seeded by a single photon is therefore a nontrivial question and cannot be answered by classical theory alone.

This motivates the analysis in Chapter 4, where the StimPDC interaction is treated quantum mechanically and the structure of the output state is derived when the seeding mode contains a single photon. The goal of that analysis is to determine whether and in what sense phase-conjugated behaviour persists in the quantum regime.

3.3 Summary

This chapter reviewed the classical behaviour of stimulated parametric down-conversion and its role in phase conjugation. Starting from the $\chi^{(2)}$ interaction Hamiltonian with a classical seed, the idler generation amplitude was shown to be governed by the spatial product $E_p E_s^*$. A complementary field-level derivation based on the driven wave equation made explicit the approximations under which the idler envelope is proportional to the nonlinear source term, thereby establishing the origin of wavefront reversal in the classical regime.

The chapter then summarized how this phase-conjugating response enables turbulence mitigation in a reciprocal free-space channel. A probe that acquires a turbulence phase on the forward path produces, upon StimPDC with a structured pump, an idler that carries the pump mode together with the conjugated turbulence phase. Backward propagation through the same channel restores the pump mode by cancelling the turbulence-induced phase without any explicit estimation of the turbulence.

To connect these ideas with quantum communication, relevant information-theoretic definitions for QKD were introduced, including Shannon entropy and mutual information. The classical turbulence-mitigation experiment was then placed in a QKD context, showing why it cannot be secure when implemented with classical travelling fields.

Finally, the chapter clarified the single-photon perspective. Even for a single photon, turbulence acts as a unitary transformation on the spatial wavefunction, so phase cancellation remains possible in principle provided an operation exists that implements phase conjugation of the spatial probability amplitude. What changes relative to the classical setting is the mechanism: the mean-field product $E_p E_s^*$ does not apply to a single-photon seed, so any phase-conjugating behaviour must be assessed using a quantum description of the nonlinear interaction. This motivates the analysis in Chapter 4, which derives the relevant output states and identifies what aspects of the classical phase-conjugation picture persist in the quantum regime.

Chapter 4

Single-Photon Seeding and Cascaded Parametric Down-Conversion

4.1 Introduction

Classical StimPDC produces an idler whose transverse structure is proportional to the product $E_p E_s^*$. This condition guarantees that the idler inherits the spatial mode of the pump and the conjugated phase of the seed, a behaviour used in Chapter 3 to correct turbulence distortions in classical free-space channels. A natural question is whether this mechanism survives when the seed is a single photon. If it did, the turbulence-mitigation strategy developed earlier could be promoted to a fully quantum protocol.

The transition to the single-photon regime changes the interaction. A single photon does not supply a classical field amplitude. Instead, the StimPDC output is determined by a StimPDC biphoton amplitude constructed from the SPDC state. This amplitude introduces both spontaneous and stimulated contributions, so the idler does not in general occupy a single well-defined spatial mode. In addition, the stimulated term is extremely weak when compared with the background of spontaneous events. This makes direct observation of the single-photon StimPDC signature difficult.

Cascaded parametric down-conversion (CPDC) resolves this difficulty. The first crystal generates a photon pair, and detection of one photon heralds the presence of a single-photon seed in the second crystal. Stimulated emission in the second stage is therefore recorded only when a seed photon is present, allowing the stimulated contribution to be isolated from the spontaneous background. This configuration provides a viable approach to observing single-photon phase conjugation.

The remainder of this chapter summarizes the theoretical behaviour relevant to single-photon seeding and introduces the complete manuscript describing the CPDC experiment. The manuscript, reproduced in Section 4.4, contains the full derivation of the SPS-PDC amplitude, the CPDC theory, and the corresponding theoretical results.

4.2 Summary of Key Results

The manuscript develops analytical expressions for the mean idler photon number in a given LG mode when the StimPDC process is seeded by a single photon. The SPS-PDC output contains two contributions:

- A spontaneous term identical to that of ordinary SPDC.

- A stimulated term that appears only when the OAM selection rule $\ell_i = -\ell_s$ is satisfied.

The stimulated term represents the single-photon analogue of the classical phase-conjugation response. When the process is measured without heralding, the stimulated contribution is overwhelmed by spontaneous emission. In contrast, the CPDC architecture uses the first-crystal idler photon to herald the seed. The joint-detection distribution of the two idler photons exhibits a clear diagonal enhancement at $\ell_{i1} = \ell_{i2}$, which is the expected conjugation signature. Heralding improves the visibility of this effect by roughly two orders of magnitude, demonstrating that CPDC provides a practical method for observing single-photon phase conjugation.

The full derivation, analysis, and supporting measurements are presented in the attached manuscript.

4.3 Author Contributions

The initial experimental concept and high-level motivation for the study were developed by Mr. Aguilar-Cardoso, who identified the CPDC geometry as a route to observing single-photon OAM phase conjugation. Building on this starting point, I identified the need to investigate how the stimulated process changes when the seed is a non-classical single-photon state rather than a bright classical beam, a question that the initial formulation had not addressed quantitatively. This became the central theoretical problem of the work.

I carried out the full theoretical development presented in this chapter and in the embedded manuscript: deriving the SPS-PDC biphoton amplitude, computing the mode-resolved mean photon number decomposition into spontaneous and stimulated contributions, and extending the framework to the CPDC configuration. I implemented all numerical simulations, generated all figures, and wrote the original manuscript draft. I also led the interpretation and presentation of the results, including the visibility analysis that quantifies the advantage of heralding over unheralded detection.

Manuscript review and editing were carried out collaboratively with the coauthors, and supervision and project oversight were provided by the senior authors. The final quantitative plots were prepared in collaboration with Dr. Ferrer-Garcia.

The theoretical framework developed here has implications beyond the specific CPDC geometry. The mode-resolved decomposition of the SPS-PDC output into spontaneous and stimulated contributions provides a general tool for analyzing any $\chi^{(2)}$ process seeded by a non-classical state, and the heralding strategy demonstrated here could be adapted to probe stimulated emission signatures in other quantum nonlinear optical configurations, including entangled-photon seeding and multi-crystal cascades.

4.4 Embedded Manuscript

For completeness, the full manuscript associated with this chapter is included in the following section.

Research Article Vol. 43, No. 3 / March 2026 / Journal of the Optical Society of America B A37

Journal of the Optical Society of America B

OPTICAL PHYSICS

Description of single-photon orbital angular momentum conjugation with stimulated parametric down-conversion [Invited]

Tobey J. B. Luck,[1,*] Aarón A. Aguilar-Cardoso,[1] Cheng Li,[1] Manuel F. Ferrer-Garcia,[1] Jeremy Upham,[1] Jeff S. Lundeen,[1,2] and Robert W. Boyd[1,3]

[1]Nexus for Quantum Technologies, Department of Physics, University of Ottawa, Ottawa K1N 6N5, Ontario, Canada
[2]National Research Council of Canada, 100 Sussex Drive, Ottawa, Ontario K1A 0R6, Canada
[3]Institute of Optics, University of Rochester, Rochester, 14627, New York, USA

Received 2 September 2025; revised 24 November 2025; accepted 25 November 2025; posted 26 November 2025; published 11 December 2025

The ability to manipulate the orbital angular momentum (OAM) of a single photon is of vital importance to photonic quantum technologies. A particularly relevant operation is the phase conjugation of OAM. One can in principle achieve this using stimulated parametric down-conversion (StimPDC), which produces an idler beam that exhibits a phase conjugate of the seed beam's spatial structure. However, implementing StimPDC for single-photon OAM phase conjugation remains challenging. This is because the photon flux of realistic single-photon sources is low compared to that of a classical pump beam, which causes the StimPDC process to occur less frequently compared to its spontaneous counterpart. To overcome this, we propose a cascaded parametric down-conversion scheme, in which the signal photon from a spontaneously down-converted pair seeds the StimPDC process, while the idler photon heralds the seed's presence. This configuration uses coincidence detection to effectively post-select for stimulated events among the background of spontaneous contributions. We show that single-photon OAM phase conjugation manifests as a bias toward equal OAM between the heralding idler and the stimulated idler. Our results offer a practical route to manipulate single-photon correlations in the OAM degree of freedom and could have implications for applications such as free-space quantum communication and quantum-enhanced sensing. © 2025 Optica Publishing Group. All rights, including for text and data mining (TDM), Artificial Intelligence (AI) training, and similar technologies, are reserved.

https://doi.org/10.1364/JOSAB.578036

1. INTRODUCTION

The family of optical beams carrying orbital angular momentum (OAM) of light, characterized by a discretized azimuthal phase dependence $\exp\{i\ell\phi\}$, has emerged as a pivotal resource in modern optics. Photons carrying OAM enable high-dimensional encoding of information, making them invaluable for applications ranging from quantum communication, cryptography, and sensing technologies [1–4]. The unbounded nature of the OAM quantum number ℓ further allows for dense multiplexing in classical and quantum channels, enabling high-capacity data transmission and enhanced noise resistance [5,6]. However, manipulation of OAM states at the single-photon level, such as phase conjugation, remains experimentally challenging, limiting their potential in practical quantum information technologies.

One transformation of particular relevance to OAM-based systems is the phase conjugation of the azimuthal structure of light, in which a light beam carrying topological charge ℓ is converted into one with charge $-\ell$. This process reverses the helical phase front of the input beam, effectively flipping the direction of OAM while preserving the radial structure. We note that one can extend this concept to reverse spatial distortions or wavefront curvature in arbitrary spatial modes of light [7–9]. Here, OAM phase conjugation refers specifically to the inversion of the azimuthal phase dependence $\exp\{i\ell\phi\}$, which can also apply to superpositions of OAM, each ℓ maps to $-\ell$, and the coefficients are complex-conjugated. This effect has been leveraged to design OAM multiplexers, quantum state synthesizers, and entanglement switchers, underscoring its versatility in both classical and quantum regimes [5,10,11]. Phase conjugation of OAM can be implemented through processes such as difference-frequency generation (DFG) [12], where angular momentum conservation enforces conjugation between input and output modes. While these effects have been demonstrated in classical regimes using coherent beams, their behavior

A38 Vol. 43, No. 3 / March 2026 / Journal of the Optical Society of America B Research Article

in the single-photon regime remains largely underexplored. Phase conjugation on the single-photon level is of particular interest due to its potential for practical quantum applications. For instance, the deterministic unitary induced on the OAM labels, which is the mode inversion $\ell \to -\ell$, can be used as a building block for quantum gates in OAM encodings (distinct from full complex conjugation, which is nonunitary) [13]. In quantum communication, single-photon phase conjugation could be used to extend various protocols into the single-photon regime. One such protocol is the mitigation of atmospheric turbulence-induced phase distortions in free-space OAM channels by mixing the phase conjugate of a probe beam (which characterizes the turbulence of the channel) with information to be sent, causing the phase distortion to be reversed upon propagation back through the turbulent media [14]. More broadly, access to quantum-compatible phase conjugation enables new strategies for high-fidelity information transfer, such as suppression of Kerr nonlinearities in optical fiber communications and adaptive optics within quantum networks [15–17].

Single-photon-stimulated parametric down-conversion (SPS-PDC), which refers to the single-photon-seeded counterpart of classically seeded StimPDC, provides a route to OAM mode phase conjugation at the single-photon level. Here, SPS-PDC denotes a $\chi^{(2)}$ interaction pumped by a classical field and stimulated by an input single photon. In conventional classically seeded StimPDC, injecting a bright seed into a pumped crystal produces down-converted light in which the idler carries the phase-conjugated spatial mode of the seed [18,19]. In the single-photon-seeded regime, the stimulated contribution competes with a substantial spontaneous background, unlike in StimPDC where the stimulated contribution dominates [20]. One can observe the transition from a spontaneous-emission-dominated PDC output to a stimulated-emission-dominated one by gradually increasing the seed beam's intensity. Interestingly, the contribution of spontaneous components is nontrivial even for StimPDC seeded by an intense classical beam, which could produce single-photon-added coherent states [21]. Both StimPDC and SPS-PDC offer several practical advantages over other methods of phase conjugation. Unlike digital approaches based on spatial light modulators, they are all-optical $\chi^{(2)}$ interactions whose response is set by the pump and phase matching bandwidths, allowing sub-nanosecond pump-limited operation without wavefront measurement [22,23]. Compared with $\chi^{(3)}$ four-wave mixing, $\chi^{(2)}$ implementations in bulk crystals avoid resonant media and associated complexity while maintaining high spatial-mode fidelity [24,25]. Moreover, energy conservation ($\omega_i = \omega_p - \omega_s$) yields simultaneous phase conjugation and frequency conversion, enabling translation between spectral bands without mode-locked sources [26]. To experimentally observe azimuthal phase conjugation in this quantum regime, it is essential to distinguish relatively rare stimulated events from a much more prevalent spontaneous background, which is a challenge arising from the inherently low intensity of the seed relative to the pump.

In this work, we analyze the SPS-PDC process and propose a cascaded implementation. The configuration, which is denoted by cascaded parametric down-conversion (CPDC), first generates a pair of down-converted photons via spontaneous parametric down-conversion (SPDC); one photon seeds an SPS-PDC process in a second nonlinear crystal, while the presence of the seed photon is heralded by detection of its idler partner. The SPDC process thus serves as both a single-photon source and a source of timing information, which allows us to measure the OAM spectrum of the SPS-PDC process conditioned on the presence of a seeding photon. Although an earlier work has investigated temporal correlations between photons produced in the CPDC configuration [27], our work extends this framework by incorporating the angular spectra of both the pump and seed beams, thereby studying the process in a spatial-mode-resolved manner and revealing how the cascaded configuration facilitates OAM phase conjugation at the single-photon level. This paper is organized as follows. In Section 2, we derive the mean number of idler photons in the SPS-PDC process in a specific Laguerre–Gaussian (LG) mode and find that the phase conjugation effect corresponds to higher mean photon numbers when the OAM of the idler and seed photons is conjugate. We then show that without heralding, the stimulated phase conjugation of the seed is overwhelmed by spontaneous emission when the seed flux is significantly lower than the pump flux, rendering the phase conjugation effect difficult to observe directly. In Section 3, we show that the CPDC approach effectively filters out unseeded spontaneous events by heralding the presence of a seed, thereby post-selecting for the stimulated events in which the phase conjugation is observed. We develop a theoretical framework for identifying signatures of OAM phase conjugation in the quantum regime and assess the conditions under which the effect can be unambiguously observed. Additionally, we quantify the visibility of the phase conjugation effect in both configurations and demonstrate how the heralding of the seed allows for the excess spontaneous events to be neglected, thus greatly increasing the visibility of the desired phase conjugation effect. In Section 4, we present our conclusions.

2. SINGLE-PHOTON-STIMULATED PARAMETRIC DOWN-CONVERSION WITHOUT HERALDING

A. Mean Idler Photon Number Distribution in Laguerre–Gaussian Modes

In SPDC, the OAM of the down-converted signal and idler photons is related to the OAM of the pump by the conservation of OAM, $\ell_p = \ell_s + \ell_i$, where ℓ_p, ℓ_s, ℓ_i denote the OAM of the pump, signal, and idler, respectively [28–30]. When the OAM of the pump is zero, the signal and idler photons will have conjugate OAM, $\ell_s = -\ell_i$, or equal in magnitude and opposite in sign. The down-converted photons generated in conjugate OAM states following the distribution are known as the spiral spectrum, denoted $\mathcal{M}^{\ell_i,\ell_s}_{p_i,p_s}$, which relates the probability of generation to azimuthal indices ℓ_i, ℓ_s and radial indices p_i, p_s [31,32]. In SPS-PDC, the conservation of OAM between the pump, signal, and idler also applies [33]. However, in this section, we show how the OAM spectrum of down-converted photons does not directly follow the spiral spectrum. This is done by deriving the mean photon number of idler photons in mode $\tilde{\mathrm{LG}}^{\ell_i}_{p_i}$ in the SPS-PDC process where we find that the mean photon number is the sum of a spontaneous and

Research Article Vol. 43, No. 3 / March 2026 / Journal of the Optical Society of America B A39

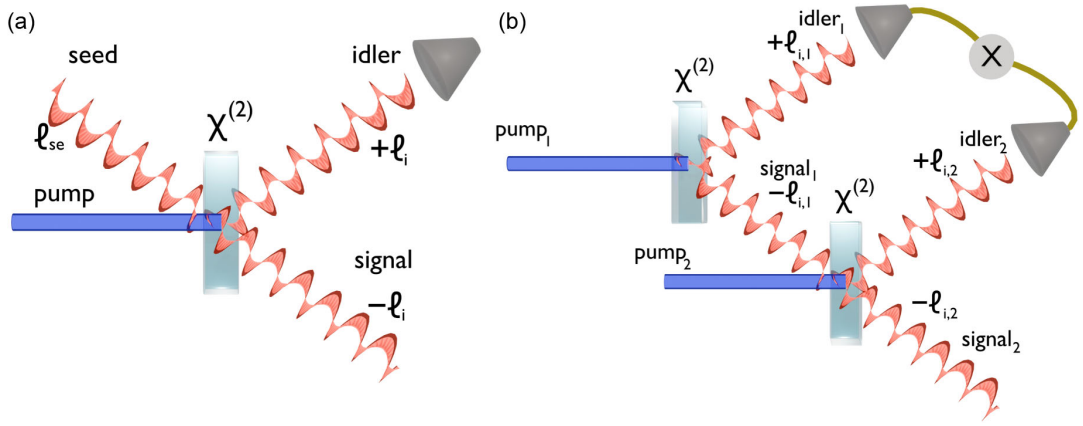


Fig. 1. Schematic of the (a) SPS-PDC process in which the mean number of photons in a specified LG mode of the idler field is measured. In this case, we consider a single-photon detector placed at the output of the idler beam; (b) CPDC process in which a single photon undergoes azimuthal phase conjugation. A seed photon (signal$_1$) generated via SPDC seeds the nonlinear process in the second crystal, while its partner photon (idler$_1$) serves as a herald. Coincidences are measured between the two single-photon detectors, one measuring the heralding photon (idler$_1$) and the other measuring the idler photon generated by the SPS-PDC process (idler$_2$), allowing the OAM spectrum of the SPS-PDC process to be measured conditioned on the presence of the seed photon.

stimulated term, where $\tilde{\mathrm{LG}}_{p_i}^{\ell_i}$ represents a LG mode in k-space (in what follows, "$\sim$" denotes that the quantity is defined in k-space) with azimuthal index ℓ_i and radial index p_i. The normalized LG mode functions in k-space are given by

$$\tilde{\mathrm{LG}}_{p}^{\ell}(\rho,\varphi)=\sqrt{\frac{w^2 p!}{2\pi(p+|\ell|)!}}\left(\frac{\rho w}{\sqrt{2}}\right)^{|\ell|} \times e^{-w^2\rho^2/4}(-1)^p L_p^{|\ell|}\left(\frac{\rho^2 w^2}{2}\right) e^{[i\ell(\varphi+\frac{\pi}{2})]}, \tag{1}$$

where ρ and φ are the radial and azimuthal coordinates in k-space, w is the corresponding spatial-frequency waist, and $L_p^{|\ell|}(\cdot)$ is the associated Laguerre polynomial. The SPS-PDC process is depicted schematically in Fig. 1(a), where a detector measuring mode $\tilde{\mathrm{LG}}_{p_i}^{\ell_i}$ measures the output of the idler in the SPS-PDC process. Here, the SPS-PDC process is seeded by a single photon with OAM ℓ_{se} (where "se" denotes the seed). The transverse profile of the biphoton down-conversion output state for a SPS-PDC process seeded by a single photon in mode $\tilde{\mathrm{LG}}_{p_{se}}^{\ell_{se}}$ in the monochromatic, paraxial, and thin crystal approximations in the low-gain regime is given by [34]

$$|\psi_{\mathrm{SPS-PDC}}\rangle = |0\rangle|1;\mathbf{q}_{se},(\ell_{se},p_{se})\rangle + C\iint \mathrm{d}^2\mathbf{q}_i\mathrm{d}^2\mathbf{q}_s\,\tilde{W}_d(\mathbf{q}_i+\mathbf{q}_s)\hat{a}^\dagger(\mathbf{q}_i)\hat{a}^\dagger(\mathbf{q}_s) \times |0;\mathbf{q}_i\rangle|1;\mathbf{q}_{se},(\ell_{se},p_{se})\rangle, \tag{2}$$

where constant $C=(\hbar\sqrt{\omega_p\omega_s\omega_i}\chi_{\mathrm{eff}}^{(2)}/\sqrt{\varepsilon_0})$ corresponds to the coefficients in the nonlinear process [20], $\tilde{W}_d(\cdot)$ corresponds to the Fourier transform of the spatial distribution of the pump at the input face of the crystal and is given by $\tilde{W}_d(\mathbf{q}_d)=(w_d/\sqrt{2\pi})\exp\{-w_d^2|\mathbf{q}_i+\mathbf{q}_s|^2/4\}$, where w_d is the beam waist of the pump in k-space, $\mathbf{q}$ are the transverse wavevectors of the fields corresponding to the pump (d), idler (i), signal (s), and seed (se), respectively, $|1;\mathbf{q},(\ell,p)\rangle$ corresponds to a Fock state in mode $\tilde{\mathrm{LG}}_{p}^{\ell}$ with transverse wavevector $\mathbf{q}$, and $\hat{a}^{(\dagger)}$ denotes an annihilation (creation) operator. Notice that in Eq. (2), the phase-matching term does not appear, as it can be approximated as unity under the thin crystal approximation [34]. The distribution $[N_{p_i}^{\ell_i}]_{\mathrm{SPS-PDC}}$ corresponds to the mean photon number of idler photons (per temporal detection mode) in mode $\tilde{\mathrm{LG}}_{p_i}^{\ell_i}$ and is given by the expectation value $[N_{p_i}^{\ell_i}]_{\mathrm{SPS-PDC}}=\langle\psi_{\mathrm{SPS-PDC}}|\hat{n}(\mathbf{q}_i,(\ell_i,p_i))|\psi_{\mathrm{SPS-PDC}}\rangle$, where $\hat{n}(\mathbf{q},(\ell,p))=\hat{a}^\dagger(\mathbf{q},(\ell,p))\hat{a}(\mathbf{q},(\ell,p))$ represents the number density associated with a photon in mode $\tilde{\mathrm{LG}}_{p}^{\ell}$ at transverse wavevector $\mathbf{q}$. Here "per temporal detection mode" means per gate (for continuous-wave pumping with a window detection window Δt, opened at frequency f_{gate}) or per pulse (for pulsed pumping at laser repetition frequency f_{rep}); measured count rates follow by multiplying the mean photon number by the gate or laser repetition frequency. The first three terms in the binomial expansion of $[N_{p_i}^{\ell_i}]_{\mathrm{SPS-PDC}}$ vanish due to the orthogonality of the Fock states: $\langle n;\mathbf{q}_1|m;\mathbf{q}_2\rangle=\delta(n-m)\delta^2(\mathbf{q}_1-\mathbf{q}_2)$. Thus, the remaining term in the mean photon number is given by

$$[N_{p_i}^{\ell_i}]_{\mathrm{SPS-PDC}} = |C|^2\int\cdots\int \mathrm{d}^2\mathbf{q}_i\mathrm{d}^2\mathbf{q}_i'\mathrm{d}^2\mathbf{q}_i''\mathrm{d}^2\mathbf{q}_i'''\mathrm{d}^2\mathbf{q}_s\mathrm{d}^2\mathbf{q}_s'\mathrm{d}^2\mathbf{q}_{se}\mathrm{d}^2\mathbf{q}_{se}'\,\tilde{W}_d(\mathbf{q}_i+\mathbf{q}_s) \times \tilde{W}_d^*(\mathbf{q}_i'+\mathbf{q}_s')\left[\tilde{\mathrm{LG}}_{p_i}^{\ell_i}(\mathbf{q}_i'')\right]^*\tilde{\mathrm{LG}}_{p_i}^{\ell_i}(\mathbf{q}_i''')\left[\tilde{\mathrm{LG}}_{p_{se}}^{\ell_{se}}(\mathbf{q}_{se})\right]^*\tilde{\mathrm{LG}}_{p_{se}}^{\ell_{se}}(\mathbf{q}_{se}') \times \langle 1;\mathbf{q}_i'|\hat{a}^\dagger(\mathbf{q}_i'')\hat{a}(\mathbf{q}_i''')|1;\mathbf{q}_i\rangle\langle 1;\mathbf{q}_{se}'|\hat{a}(\mathbf{q}_s')\hat{a}^\dagger(\mathbf{q}_s)|1;\mathbf{q}_{se}\rangle. \tag{3}$$

A40 Vol. 43, No. 3 / March 2026 / Journal of the Optical Society of America B Research Article

Due to the ladder-operator action on the Fock states and the orthonormality of the Fock states, the inner product $\langle 1;\mathbf{q}_i'|\hat{a}^\dagger(\mathbf{q}_i'')\hat{a}(\mathbf{q}_i''')|1;\mathbf{q}_i\rangle = \delta^2(\mathbf{q}_i''-\mathbf{q}_i')\delta^2(\mathbf{q}_i'''-\mathbf{q}_i)$. We use the canonical commutation relation in the transverse-momentum continuum $[\hat{a}(\mathbf{q}_s'),\hat{a}^\dagger(\mathbf{q}_s)] = \delta^{(2)}(\mathbf{q}_s'-\mathbf{q}_s)$ from which it follows that

$$\hat{a}(\mathbf{q}_s')\hat{a}^\dagger(\mathbf{q}_s) = \delta^2(\mathbf{q}_s'-\mathbf{q}_s) + \hat{a}^\dagger(\mathbf{q}_s)\hat{a}(\mathbf{q}_s'). \tag{4}$$

This relation can be used to evaluate the inner product as

$$\begin{aligned}&\langle 1;\mathbf{q}_{se}'|\hat{a}(\mathbf{q}_s')\hat{a}^\dagger(\mathbf{q}_s)|1;\mathbf{q}_{se}\rangle\\ &= \delta^2(\mathbf{q}_{se}'-\mathbf{q}_{se})\delta^2(\mathbf{q}_s'-\mathbf{q}_s) + \delta^2(\mathbf{q}_{se}'-\mathbf{q}_s)\delta^2(\mathbf{q}_s'-\mathbf{q}_{se}).\end{aligned} \tag{5}$$

Due to the orthonormality of the LG modes in k-space, $\int \mathrm{d}^2\mathbf{q}\tilde{\mathrm{LG}}_p^{\ell}(\mathbf{q})[\tilde{\mathrm{LG}}_{p'}^{\ell'}(\mathbf{q})]^* = \delta_{\ell,\ell'}\delta_{p,p'}$, the mean photon number evaluates to

$$\begin{aligned}&[N_{p_i}^{\ell_i}]_{\mathrm{SPS-PDC}}\\ &= |C|^2 \iiint \mathrm{d}^2\mathbf{q}_i\mathrm{d}^2\mathbf{q}_i'\mathrm{d}^2\mathbf{q}_s\, \tilde{W}_d(\mathbf{q}_i+\mathbf{q}_s)\\ &\quad\times \tilde{W}_d^*(\mathbf{q}_i'+\mathbf{q}_s)\tilde{\mathrm{LG}}_{p_i}^{\ell_i}(\mathbf{q}_i)\left[\tilde{\mathrm{LG}}_{p_i}^{\ell_i}(\mathbf{q}_i')\right]^*\\ &\quad+\left|C\iint \mathrm{d}^2\mathbf{q}_i\mathrm{d}^2\mathbf{q}_s\, \tilde{W}_d(\mathbf{q}_i+\mathbf{q}_s)\tilde{\mathrm{LG}}_{p_i}^{\ell_i}(\mathbf{q}_i)\tilde{\mathrm{LG}}_{p_{se}}^{\ell_{se}}(\mathbf{q}_s)\right|^2.\end{aligned} \tag{6}$$

We note that there exists a weighting factor on the second term in Eq. (6) relative to the first term that depends on the average photon number in the seeding mode. However, since the seeding mode is composed of a single photon, this weighting factor evaluates to 1, which agrees with previous work that shows the weighting factor of the stimulated contribution scales linearly with the average number of photons in the seeding mode [35]. The overlap integrals in Eq. (6), where $\mathcal{N}_{p_i}^{\ell_i}$ and $|\mathcal{M}_{p_i,p_{se}}^{\ell_i,\ell_{se}}|^2$ correspond to the first and second integrals, respectively, have been solved analytically in Sections (S1) and (S2) of Supplement 1. This allows for the mean photon number to be expressed as

$$[N_{p_i}^{\ell_i}]_{\mathrm{SPS-PDC}} = \mathcal{N}_{p_i}^{\ell_i} + \delta_{\ell_i,-\ell_{se}}\left|\mathcal{M}_{p_i,p_{se}}^{\ell_i,\ell_{se}}\right|^2. \tag{7}$$

The terms $\mathcal{N}_{p_i}^{\ell_i}$ and $\mathcal{M}_{p_i,p_{se}}^{\ell_i,\ell_{se}}$ are given by the analytical expressions Eq. (S20) and (S22) and have been plotted in Figs. 2(a) and 2(b), respectively, where the beam waist of the seed and detection beam waists are equal to the beam waist of the pump $w_d = w_{se} = w_i = w_i'$. The beam waists w_{se}, w_i, and w_i' correspond to the beam waists in k-space of the corresponding LG mode function given by Eq. (1). The term $\mathcal{N}_{p_i}^{\ell_i}$ corresponds to the mean number of idler photons in mode $\tilde{\mathrm{LG}}_{p_i}^{\ell_i}$ in the SPDC process, while the term $\mathcal{M}_{p_i,p_{se}}^{\ell_i,\ell_{se}}$ corresponds to the mean number of signal–idler photon pairs in modes $\tilde{\mathrm{LG}}_{p_{se}}^{\ell_{se}}$ and $\tilde{\mathrm{LG}}_{p_i}^{\ell_i}$. The origin of both of these terms is explored in Sections (S3) and (S4) of Supplement 1. In this study, we focus on the OAM phase conjugation effect in the StimPDC process. Although our analytical expressions are derived for an arbitrary radial index p, the radial number does not modify the OAM phase conjugation condition itself ($\ell_i = -\ell_{se}$). Increasing p broadens the distributions $\mathcal{N}_{p_i}^{\ell_i}$ and $\mathcal{M}_{p_i,p_{se}}^{\ell_i,\ell_{se}}$ in a way consistent with the behavior of higher-order radial modes in SPDC [32]. We therefore restrict the analyses to the case $p = 0$. Note that in some systems, nonzero radial indices can give rise to coupling between the radial and azimuthal degrees of freedom, producing superpositions of higher-order radial modes and altered OAM spectra while maintaining overall OAM conservation [36]. We note that the numerical evaluation of $\mathcal{M}_{p_i,p_{se}}^{\ell}$, where $\ell = \ell_i = -\ell_{se}$, shows excellent agreement with the numerical evaluation of the analytical solution of the spiral spectrum of the unseeded SPDC [32] when both expressions are normalized, as plotted in Fig. 2(c). Reproducing this distribution in our stimulated scheme indicates that the process implements the expected azimuthal phase conjugation of the seed photon through the underlying OAM conservation in nonlinear optical processes. In the case of perfect phase conjugation in the SPS-PDC process, we require $\mathcal{N}_{p_i}^{\ell_i} = 0$ since it is not constrained by the Kronecker delta $\delta_{\ell_i,-\ell_{se}}$. As a result, a seeding photon carrying OAM ℓ_{se} always generates an idler with OAM $\ell_i = -\ell_{se}$. The Kronecker delta $\delta_{\ell_i,-\ell_{se}}$ is written explicitly in Eq. (7) to emphasize that when the stimulated process occurs the idler azimuthal index equals that of the seed. The first term in Eq. (7), $\mathcal{N}_{p_i}^{\ell_i}$, represents the spontaneous contribution to the mean photon number distribution. This term arises because the transverse wavevectors of the signal and seed photons do not interact, meaning that no stimulated process occurs, and the contribution is purely spontaneous. The second term in the sum refers to the stimulated contribution to the coincidence amplitude; however, in this term, the transverse wavevector of the idler is equal to the conjugate of the seed, as constrained by the Kronecker deltas. It is evident that the key feature indicating phase conjugation in the LG-resolved mean idler photon number distribution is the anti-diagonal along $\ell_i = -\ell_{se}$.

B. Measuring Without Heralding

We now consider what the statistics would look like when experimentally measuring the mean idler photon number in mode $\tilde{\mathrm{LG}}_{p_i}^{\ell_i}$ as a function of azimuthal index ℓ_i. One must consider that SPS-PDC only takes place when both a pump photon and a seed photon are present at the nonlinear crystal within the interaction time of the nonlinear crystal, Δt. If there is only a pump photon and no seed photon at the nonlinear crystal over Δt, only SPDC can occur. As a result, the measured mean idler photon number will have two contributing terms: a SPDC contribution and a SPS-PDC contribution, each weighted by their respective per-gate occurrence probabilities σ_{SPDC} and $\sigma_{\mathrm{SPS-PDC}}$ which both range from 0 to 1 depending on their relative likelihoods to occur. The measured mean photon number for idler photons in mode $\tilde{\mathrm{LG}}_{p_i}^{\ell_i}$ can be expressed as

$$[N_{p_i}^{\ell_i}]_{\mathrm{measured}} = \sigma_{\mathrm{SPDC}}[N_{p_i}^{\ell_i}]_{\mathrm{SPDC}} + \sigma_{\mathrm{SPS-PDC}}[N_{p_i}^{\ell_i}]_{\mathrm{SPS-PDC}}, \tag{8}$$

where $[N_{p_i}^{\ell_i}]_{\mathrm{SPDC}}$ is the mean photon number for idler photons in LG mode $\tilde{\mathrm{LG}}_{p_i}^{\ell_i}$ in SPDC summed over all idler radial

Research Article Vol. 43, No. 3 / March 2026 / Journal of the Optical Society of America B A41

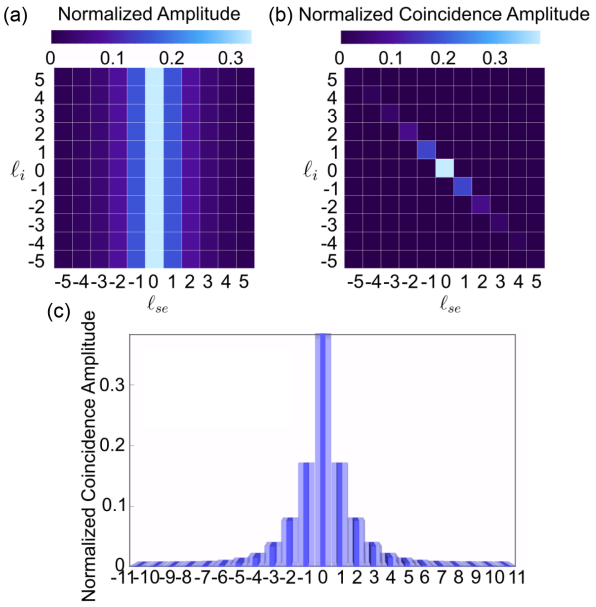


Fig. 2. Signature of OAM phase conjugation in SPS-PDC. (a) The spontaneous term: the idler distribution is independent of the seed's OAM. (b) The stimulated term only contributes along the anti-diagonal $\ell_i = -\ell_{se}$, the signature of OAM phase conjugation. (c) 1D spiral spectrum: the anti-diagonal slice (dark blue) agrees with the known SPDC spiral spectrum (light blue [32]). All plots are normalized over all possible azimuthal indices and $p_i = p_{se} = 0$.

indices p_i. To see how Eq. (8) arises, consider the two extremes. The first extreme: no seeding photons are sent, and a pump photon is always present at the nonlinear crystal ($R_p \Delta t \gg 1$ and $R_{se} = 0$), so $\sigma_{\text{SPS-PDC}} = 0$ and $\sigma_{\text{SPDC}} = 1$. It is trivial to see how the measured mean idler photon number will correspond to the mean idler photon number in the SPDC process as only SPDC can occur. For the other extreme, assume that there is always a pair of seed and pump photons present at the nonlinear crystal ($R_p \Delta t \gg 1$ and $R_{se} \Delta t \gg 1$). Interactions seeded by vacuum (where a pump photon is present while no seed photon is present) will not occur, so $\sigma_{\text{SPS-PDC}} = 1$ and $\sigma_{\text{SPDC}} = 0$. Similarly, it is clear that the measured mean idler photon number will correspond to the mean idler photon number in the SPS-PDC process, as it is the only process that can occur. So in the ideal scenario, to experimentally measure the distribution $[N_{p_i}^{\ell_i}]_{\text{SPS-PDC}}$, one would require that $\sigma_{\text{SPS-PDC}} = 1$ and $\sigma_{\text{SPDC}} = 0$. However, without heralding the presence of the seed, this condition is difficult to satisfy; this is shown in the following calculation. We assume Poissonian statistics to model the arrival probability of both pump and seed photons. While quantum single-photon sources exhibit sub-Poissonian photon number statistics, the Poissonian approximation captures the probabilistic nature of photon arrival within the interaction window Δt, which is sufficient for estimating interaction likelihoods [37]. The weighting factor σ_{SPDC} then depends on the product of the Poissonian statistics associated with at least one pump photon and no seed photons (vacuum) present over the interaction time Δt at the nonlinear crystal:

$$\sigma_{\text{SPDC}} = (1 - e^{-R_p \Delta t}) e^{-R_{se} \Delta t}, \tag{9}$$

where R_p (R_{se}) corresponds to the rate of pump (seed) photons per second. The probability of a stimulated interaction occurring is the joint probability that both a pump and a seed photon are present at the nonlinear crystal over time Δt:

$$\sigma_{\text{SPS-PDC}} = (1 - e^{-R_p \Delta t})(1 - e^{-R_{se} \Delta t}). \tag{10}$$

Since most single-photon sources emit single photons at low rates ($\lesssim 1.2 \times 10^8$ Hz) [38–40] and that interaction times in PDC experiments are typically on the order of picoseconds [41,42] (or much shorter in the absence of cavities), we can assume $R_{se} \Delta t \ll 1$ and expand both terms to the first order: $\sigma_{\text{SPDC}} \approx (1 - \exp\{-R_p \Delta t\})(1 - R_{se} \Delta t)$ and $\sigma_{\text{SPS-PDC}} \approx (1 - \exp\{-R_p \Delta t\}) R_{se} \Delta t$. Thus, the ratio between the two quantities is

$$\frac{\sigma_{\text{SPS-PDC}}}{\sigma_{\text{SPDC}}} \approx \frac{R_{se} \Delta t}{1 - R_{se} \Delta t} \ll 1. \tag{11}$$

Therefore, the vast majority of the SPS-PDC interaction will be overshadowed by the immense contribution of SPDC to the measured mean idler photon number distribution. This is shown further in Fig. 3 that depicts the mean photon number for idler photons in mode $\tilde{\text{LG}}_0^{\ell_i}$ (radial indices $p_i = p_{se} = 0$) over idler azimuthal index ℓ_i for detection beam waists equal to the beam waist of the pump ($w_d = w_i = w_i' = w_s$) in the SPS-PDC case, Eq. (7), and the measured case, Eq. (8) for $\ell_{se} \in [-5, 5]$. Both the SPS-PDC distribution Fig. 3(a) and measured distribution Fig. 3(b) are normalized over all possible idler azimuthal indices ℓ_i for each value of ℓ_{se}, and values of $R_p = 2 \times 10^{16}$ photons per second (corresponding to 10 mW of 405 nm), $R_{se} = 1.2 \times 10^8$ photons per second, and $\Delta t = 10$ ps are used in the simulated distributions. Using the proposed values for R_p, R_{se}, and Δt, we find that $\sigma_{\text{SPDC}} = 0.999$ and $\sigma_{\text{SPS-PDC}} = 1.2 \times 10^{-3}$ leading to the ratio $\sigma_{\text{SPS-PDC}}/\sigma_{\text{SPDC}} = 1.2 \times 10^{-3}$. In the SPS-PDC case, the OAM of the seed slightly increases the mean photon number when $\ell_i = -\ell_{se}$, which is the signature of phase conjugation. This effect is difficult to observe in the measured case since the number of stimulated events is far outweighed by the number of spontaneous events. Even with temporal gating, measurements

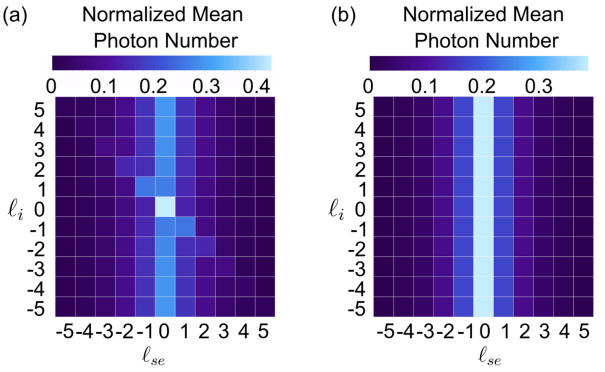


Fig. 3. Direct comparison of the simulated normalized mean photon numbers for idler photons in mode $\tilde{\text{LG}}_0^{\ell_i}$ for (a) SPS-PDC, $[N_0^{\ell_i}]_{\text{SPS-PDC}}$; (b) the measured SPS-PDC scenario with no heralding, $[N_0^{\ell_i}]_{\text{measured}}$. As we can observe, the slightly enhanced anti-diagonal OAM correlation pattern that is discernable in (a), indicating phase conjugation, becomes heavily suppressed in (b).

A42 Vol. 43, No. 3 / March 2026 / Journal of the Optical Society of America B Research Article

of down-converted modes contingent on the excitation of a single-photon source remain polluted by excess SPDC contributions, as currently available single-photon sources are not 100% efficient [38–40]. In other words, since not all source excitations produce a photon, many unseeded events (SPDC) appear indistinguishable from genuinely seeded interactions (SPS-PDC). In the following section, we demonstrate that by cascading PDC processes, one can overcome the excess SPDC contributions to the measured mean idler photon number distribution through the use of heralding the presence of the seeding photon, allowing the phase conjugation effect in SPS-PDC to be better observed.

3. CASCADED PARAMETRIC DOWN-CONVERSION

A. Joint Mean Photon Number Distribution for Idler Photons in Laguerre–Gaussian Modes

The CPDC configuration, shown in Fig. 1(b), heralds the presence of a seeding photon and the occurrence of a subsequent SPS-PDC event using temporal correlations between down-converted photon pairs from an initial SPDC process. This scheme filters excess background SPDC events, isolating only those interactions truly seeded by a single photon. To model this configuration, we develop a theoretical framework describing the expected spatial and temporal correlations between the idler photons when one of the spontaneously down-converted signal photons is used to seed a subsequent SPS-PDC process. In this section, we compute the joint mean photon number distribution for the idler photons, one from each nonlinear interaction, in modes $\tilde{\mathrm{LG}}^{\ell_{i1}}_{p_{i1}}$ and $\tilde{\mathrm{LG}}^{\ell_{i2}}_{p_{i2}}$, respectively, denoted by $[N^{\ell_{i1},\ell_{i2}}_{p_{i1},p_{i2}}]_{\mathrm{CPDC}}$, where the subscripts 1 and 2 denote the first and second nonlinear processes, respectively. The resulting distribution contains two distinct terms: one arising from spontaneous emission and one from stimulated emission seeded by a single photon. The OAM representation of the biphoton SPDC output state in the monochromatic, paraxial, and thin crystal approximations is given by [31]

$$|\psi_{\mathrm{SPDC}}\rangle = \sum_{\ell_i,\ell_s=-\infty}^{\infty}\sum_{p_i,p_s=0}^{\infty}\mathcal{M}^{\ell_i,\ell_s}_{p_i,p_s} \times \int \mathrm{d}^2\mathbf{q}_s\left[\tilde{\mathrm{LG}}^{\ell_s}_{p_s}(\mathbf{q}_s)\right]^*|1;\mathbf{q}_i,(\ell_i,p_i)\rangle|1;\mathbf{q}_s\rangle, \tag{12}$$

where $\mathcal{M}^{\ell_i,\ell_s}_{p_i,p_s}$ are the coincidence amplitudes associated with observing a pair of idler–signal photons in modes $\tilde{\mathrm{LG}}^{\ell_i}_{p_i}$ and $\tilde{\mathrm{LG}}^{\ell_s}_{p_s}$ in the output of SPDC, otherwise known as the spiral spectrum [32]; a derivation of this relation is developed in Section (S4) of Supplement 1. The azimuthal portion of this integral introduces the Kronecker delta $\delta_{\ell_i,-\ell_s}$; thus, without loss of generality, we homogenize the azimuthal indices such that $\ell_i = -\ell_s = \ell$. The resulting quad-photon CPDC output state is then found by substituting Eq. (12) as the seeding state in the typical StimPDC output state in the monochromatic, paraxial, and thin crystal approximations and the low-gain regime [18]:

$$\begin{aligned}|\psi_{\mathrm{CPDC}}\rangle &= \sum_{\ell=-\infty}^{\infty}\sum_{p_i,p_s=0}^{\infty}\mathcal{M}^{\ell}_{p_i,p_s}\left[\int \mathrm{d}^2\mathbf{q}_{s1}\left[\tilde{\mathrm{LG}}^{-\ell}_{p_s}(\mathbf{q}_{s1})\right]^* \times |1;\mathbf{q}_{i1},(\ell,p_i)\rangle|1;\mathbf{q}_{s1}\rangle \right.\\ &\left. + C_2\iiint \mathrm{d}^2\mathbf{q}_{s1}\mathrm{d}^2\mathbf{q}_{i2}\mathrm{d}^2\mathbf{q}_{s2}\,\tilde{W}_{d2}(\mathbf{q}_{i2}+\mathbf{q}_{s2}) \times \left[\tilde{\mathrm{LG}}^{-\ell}_{p_s}(\mathbf{q}_{s1})\right]^*\hat{a}^\dagger(\mathbf{q}_{s2})|1;\mathbf{q}_{i1},(\ell,p_i)\rangle|1;\mathbf{q}_{s1}\rangle|1;\mathbf{q}_{i2}\rangle\right].\end{aligned} \tag{13}$$

The joint mean photon number distribution associated with idler photons in modes $\tilde{\mathrm{LG}}^{\ell_{i1}}_{p_{i1}}$ and $\tilde{\mathrm{LG}}^{\ell_{i2}}_{p_{i2}}$ (per temporal detection mode) is given by $[N^{\ell_{i1},\ell_{i2}}_{p_{i1},p_{i2}}]_{\mathrm{CPDC}} = \langle\psi_{\mathrm{CPDC}}|\hat{n}(\mathbf{q}_{i1},(\ell_{i1},p_{i1}))\,\hat{n}(\mathbf{q}_{i2},(\ell_{i2},p_{i2}))|\psi_{\mathrm{CPDC}}\rangle$. Expanding the expectation value results in a binomial expansion; the first three terms of this expansion vanish due to the orthogonality of the Fock states. We again impose the relation in Eq. (4) and the ladder-operator action on Fock states, together with the orthonormality of the Fock basis, to evaluate the matrix elements. This introduces the Kronecker deltas $\delta_{\ell',\ell_{i1}}\delta_{\ell_{i1},\ell}\delta_{p'_i,p_{i1}}\delta_{p_{i1},p_i}$ and Dirac delta functions $\delta^2(\mathbf{q}'_{i1}-\mathbf{q}''_{i1})\delta^2(\mathbf{q}'''_{i1}-\mathbf{q}_{i1})$ for the first inner product, which collapses the sums over ℓ, ℓ' and p_i, p'_i at ℓ_{i1} and p_{i1}, and the integrals over $\mathbf{q}''_{i1}$ and $\mathbf{q}'''_{i1}$. Similarly, the second inner product collapses the integrals over $\mathbf{q}''_{i2}$ and $\mathbf{q}'''_{i2}$. The orthogonality of the LG modes forces $p_s = p'_s$ in the first term. This simplifies $[N^{\ell_{i1},\ell_{i2}}_{p_{i1},p_{i2}}]_{\mathrm{CPDC}}$ as

$$\begin{aligned}[N^{\ell_{i1},\ell_{i2}}_{p_{i1},p_{i2}}]_{\mathrm{CPDC}} &= \sum_{p_s=0}^{\infty}|\mathcal{M}^{\ell_{i1}}_{p_{i1},p_s}|^2|C_2|^2\iiint \mathrm{d}^2\mathbf{q}_{i2}\mathrm{d}^2\mathbf{q}'_{i2}\mathrm{d}^2\mathbf{q}_{s2}\,\tilde{W}_{d2}(\mathbf{q}_{i2}+\mathbf{q}_{s2}) \times \tilde{W}^*_{d2}(\mathbf{q}'_{i2}+\mathbf{q}_{s2})\tilde{\mathrm{LG}}^{\ell_{i2}}_{p_{i2}}(\mathbf{q}_{i2})\left[\tilde{\mathrm{LG}}^{\ell_{i2}}_{p_{i2}}(\mathbf{q}'_{i2})\right]^*\\ &+ \sum_{p_s,p'_s=0}^{\infty}C_2^*\iint \mathrm{d}^2\mathbf{q}_{s1} \times \mathrm{d}^2\mathbf{q}'_{i2}\,\tilde{W}^*_{d2}(\mathbf{q}_{s1}+\mathbf{q}'_{i2})\left[\tilde{\mathrm{LG}}^{-\ell_{i1}}_{p_s}(\mathbf{q}_{s1})\right]^*\left[\tilde{\mathrm{LG}}^{\ell_{i2}}_{p_{i2}}(\mathbf{q}'_{i2})\right]^* \times C_2\iint \mathrm{d}^2\mathbf{q}_{i2}\mathrm{d}^2\mathbf{q}_{s2}\,\tilde{W}_{d2}(\mathbf{q}_{i2}+\mathbf{q}_{s2})\tilde{\mathrm{LG}}^{\ell_{i2}}_{p_{i2}}(\mathbf{q}_{i2})\tilde{\mathrm{LG}}^{-\ell_{i1}}_{p'_s}(\mathbf{q}_{s2}).\end{aligned} \tag{14}$$

We then note that the remaining triple integral in the first term of Eq. (14) corresponds to the spontaneous overlap integral found in the first term of Eq. (6), which is solved analytically in Eq. (S20). The second term of Eq. (14) contains two double integrals that have the same form as the double integrals found in the second term of Eq. (6), with both having the solution found in Eq. (S22). Each of these double integrals introduces the Kronecker delta $\delta_{\ell_{i1},\ell_{i2}}$, which is a signature of the stimulating process. The resulting joint mean idler photon number is given by

Research Article Vol. 43, No. 3 / March 2026 / Journal of the Optical Society of America B A43

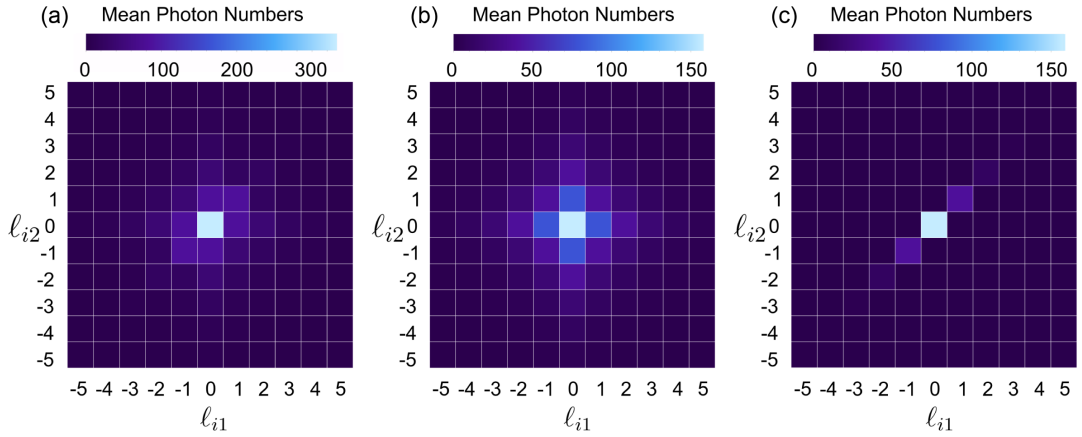


Fig. 4. Joint simulated mean photon numbers (z axis) associated with generating idler photon pairs with indices ℓ_{i1}, ℓ_{i2} for the (a) CPDC configuration, showing a strong diagonal along $\ell_{i1} = \ell_{i2}$ corresponding to phase conjugation; (b) spontaneous contribution, which is broad due to the lack of correlation between the two idler modes; and (c) stimulated contribution, present only along the diagonal $\ell_{i1} = \ell_{i2}$ as the second idler is produced in the conjugate OAM mode of the seeding photon ($-\ell_{s1} = \ell_{i1}$). The mean photon number distribution in (a) is obtained by summing the spontaneous and stimulated terms.

$$[N^{\ell_{i1},\ell_{i2}}_{p_{i1},p_{i2}}]_{\mathrm{CPDC}}$$
$$= \sum_{p_s=0}^{\infty} \left|\mathcal{M}^{\ell_{i1}}_{p_{i1},p_s}\right|^2 \mathcal{N}^{\ell_{i2}}_{p_{i2}} + \sum_{p_s,p_s'=0}^{\infty} \mathcal{M}^{\ell_{i1}}_{p_{i1},p_s}\left[\mathcal{M}^{\ell_{i1}}_{p_{i1},p_s'}\right]^*$$
$$\times \left[\mathcal{M}^{-\ell_{i1},\ell_{i2}}_{p_s,p_{i2}}\right]^* \mathcal{M}^{-\ell_{i1},\ell_{i2}}_{p_s',p_{i2}}. \quad (15)$$

Notably, when $p_s = p_s'$, Eq. (15) reduces to the form of Eq. (7), multiplied by the factor $\sum_{p_s=0}^{\infty} |\mathcal{M}^{\ell_i}_{p_{i1},p_s}|^2$. This shows that the CPDC configuration does not generate a new OAM distribution beyond the SPS-PDC distribution; the SPS-PDC distribution is reweighed by $\sum_{p_s=0}^{\infty} |\mathcal{M}^{\ell_i}_{p_{i1},p_s}|^2$. Similarly to the case of SPS-PDC with an ideal single-photon source, this distribution consists of a spontaneous background contribution and a stimulated contribution that appears when the two idler indices are equal ($\ell_{i1} = \ell_{i2}$), agreeing with previous analyses of the same cascaded system [27]. Therefore, mean photon numbers along the diagonal will indicate the presence of the phase conjugation effect at the single-photon level.

B. Advantage of Heralding

This cascaded configuration offers a key advantage over the single-photon-seeded StimPDC: the experimentally measured quantity $[N^{\ell_{i1},\ell_{i2}}_{p_{i1},p_{i2}}]_{\mathrm{CPDC}}$ heralded by detections of idler photons in specified LG modes directly corresponds to the theoretical mean photon number distribution $[N^{\ell_{i1},\ell_{i2}}_{p_{i1},p_{i2}}]_{\mathrm{CPDC}}$. In this setup, coincidences are recorded only when both idler photons are detected within the correlation window, effectively ensuring that the SPS-PDC emission is measured exclusively when a seeding photon is present. This approach suppresses contributions from purely spontaneous interactions, which otherwise dominate in the measured SPS-PDC configuration. Since the experimentally measured joint idler mean photon number distribution does not consist of any purely SPDC contributions, the per-gate occurrence probabilities do not appear in the distribution. The enhancement of the phase conjugation signature in CPDC can be exemplified when plotting the joint mean idler photon number distribution given by Eq. (15). The plot Fig. 4(a) shows the joint simulated mean photon number distribution $[N^{\ell_{i1},\ell_{i2}}_{0,0}]_{\mathrm{CPDC}}$ for generating idler photon pairs in the CPDC configuration ($p_{i1} = p_{i2} = 0$). The restriction to $p_{i1} = p_{i2} = 0$ is made for the same reason discussed previously: nonzero radial indices broaden the mode-overlap terms without modifying the OAM phase-conjugation relation between ℓ_{i1} and ℓ_{i2}. The distribution exhibits an enhancement along the diagonal $\ell_{i1} = \ell_{i2}$, indicating the phase conjugation effect. To illustrate the origin of this feature, we separate the total distribution into its spontaneous and stimulated contributions in Figs. 4(b) and 4(c), respectively. The spontaneous term lacks an enhancement along the diagonal, consistent with the absence of transverse-mode interaction between the seed and down-converted photons in the second nonlinear crystal. In contrast, the stimulated term is confined to the diagonal $\ell_{i1} = \ell_{i2}$ due to the Kronecker delta $\delta_{\ell_{i1},\ell_{i2}}$ reflecting the constraint $\ell_{i2} = -\ell_{s1} = \ell_{i1}$ imposed by the interaction between the seed's transverse wavevector and the down-converted modes.

Both Figs. 4(c) and 2(b) illustrate the same single-photon-level phase conjugation process; however, their spectral widths differ. In Fig. 2(b), we assume a uniform seeding probability of one photon for all ℓ values. In contrast, for the CPDC case shown in Fig. 4(c), the probability of seeding a photon varies and decreases depending on its ℓ_i value. Previous studies have shown that increasing the beam waist ratio between the pump and the seed modifies the single-photon probability distribution as a function of ℓ_i [43]. This adjustment could, in principle, be used to reshape the distribution observed in Fig. 4(c); this effect is briefly explored in Section (S5) of Supplement 1.

To quantify the advantage of using the CPDC configuration, we characterize the visibility of the phase conjugation signature in both the CPDC and measured SPS-PDC mean photon number distributions. Since phase conjugation only occurs along specific pairs of azimuthal indices in both cases, along

A44 Vol. 43, No. 3 / March 2026 / Journal of the Optical Society of America B Research Article

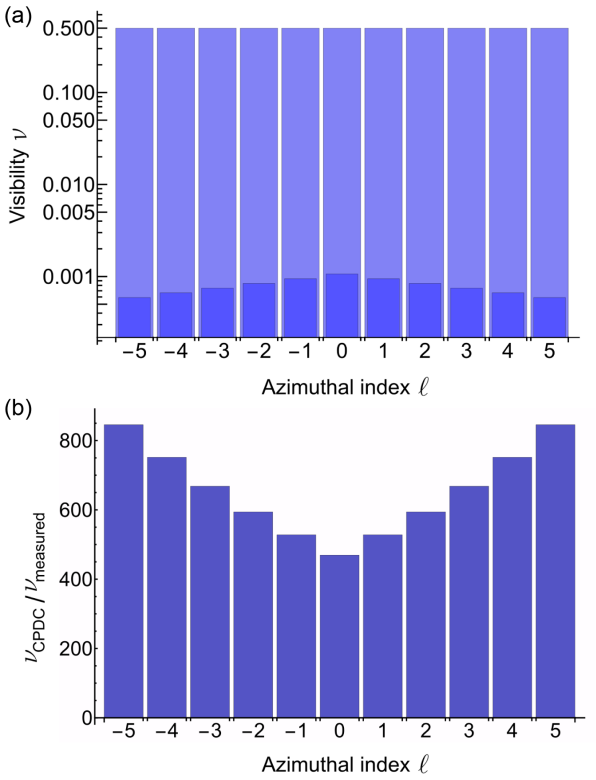


Fig. 5. (a) Comparison between the visibilities of the phase conjugation signature for the CPDC distribution (light blue) and measured SPS-PDC distribution (dark blue); (b) the visibility gain between the CPDC and measured SPS-PDC configurations. Heralding the presence of the seeding photon allows the visibility of the phase conjugation signature in the CPDC configuration to be heavily enhanced relative to the measured SPS-PDC configuration.

the diagonal $\ell_{i1} = \ell_{i2}$ in the CPDC case and along the anti-diagonal $\ell_i = -\ell_{se}$ in the SPS-PDC case, the visibility will only be considered for these indices ($\ell = \ell_{i1} = \ell_{i2} = \ell_i = -\ell_{se}$). Additionally, we will examine the case where $p_i = p_{se} = p_{i1} = p_{i2} = 0$. The visibility of the phase conjugation signature can be quantified for each index ℓ as the fraction of the mean photon number that the stimulated term contributes

$$[\nu_{0,0}^{\ell}]_{\mathrm{CPDC}} = \frac{\sum_{p_s, p_s'=0}^{\infty} \mathcal{M}_{0,p_s}^{\ell} \left[\mathcal{M}_{0,p_s'}^{\ell}\right]^* [\mathcal{M}_{p_s,0}^{\ell}]^* \mathcal{M}_{p_s',0}^{\ell}}{[N_{0,0}^{\ell}]_{\mathrm{CPDC}}}, \tag{16}$$

for the CPDC distribution and

$$[\nu_0^{\ell}]_{\mathrm{measured}} = \frac{\sigma_{\mathrm{SPS-PDC}} |\mathcal{M}_{0,0}^{\ell}|^2}{[N_0^{\ell}]_{\mathrm{measured}}}, \tag{17}$$

for the SPS-PDC distribution. The visibilities $[\nu_{0,0}^{\ell}]_{\mathrm{CPDC}}$ and $[\nu_0^{\ell}]_{\mathrm{measured}}$ are plotted in Fig. 5(a), where a logarithmic scale is used due to the difference in magnitude between the two quantities. Furthermore, the visibility gain in the CPDC configuration, $[\nu_{0,0}^{\ell}]_{\mathrm{CPDC}}/[\nu_0^{\ell}]_{\mathrm{measured}}$, is plotted in Fig. 5(b). The higher visibilities in the CPDC configuration indicate that heralding the presence of the seeding photon allows for the phase conjugation signature to be observed much easier. This is further supported by the visibility gain of two orders of magnitude for all values of ℓ in the CPDC configuration relative to the measured SPS-PDC configuration.

4. CONCLUSION

We have developed a fully analytical model for CPDC that captures both the spontaneous and stimulated contributions to the mean photon number distribution $[N_{p_{i1},p_{i2}}^{\ell_{i1},\ell_{i2}}]_{\mathrm{CPDC}}$ associated with generating idler photon pairs in specific LG modes in CPDC. The model predicts that the spontaneous term yields a broad background with no enhanced diagonal structure, whereas the stimulated term produces a distinct enhancement in the distribution along $\ell_{i1} = \ell_{i2}$. This provides a clear theoretical signature for identifying azimuthal phase conjugation at the single-photon level. The advantage of the CPDC configuration over performing SPS-PDC without heralding for the presence of the seed is the ability to filter out unwanted SPDC contributions, thereby increasing the visibility of the phase conjugation signature by two orders of magnitude. This approach represents a significant step toward experimentally realizing quantum nonlinear optical effects with structured single photon, opening pathways for advancing quantum information processing schemes.

Funding. Canada Research Chairs (950-231657); Natural Sciences and Engineering Research Council of Canada (Alliance Consortia Quantum Grant ALLRP 578468 - 22, Discovery Grant RGPIN/2017-06880).

Acknowledgment. Conceptualization—Aarón A. Aguilar-Cardoso. Methodology—Tobey J. B. Luck and Aarón A. Aguilar-Cardoso. Formal analysis—Tobey J. B. Luck and Aarón A. Aguilar-Cardoso. Investigation—Tobey J. B. Luck and Aarón A. Aguilar-Cardoso. Software—Tobey J. B. Luck. Validation—Cheng Li, Manuel F. Ferrer-Garcia, Jeremy Upham, Jeff S. Lundeen, and Robert W. Boyd. Visualization—Tobey J. B. Luck. Writing: original draft—Tobey J. B. Luck. Writing: review and editing—Aarón A. Aguilar-Cardoso, Cheng Li, Manuel F. Ferrer-Garcia, Jeremy Upham, Jeff S. Lundeen, and Robert W. Boyd. Supervision—Aarón A. Aguilar-Cardoso and Manuel F. Ferrer-Garcia. Project administration—Manuel F. Ferrer-Garcia. Funding acquisition—Jeff S. Lundeen and Robert W. Boyd.

Disclosures. The authors declare no conflicts of interest.

Data availability. Data underlying the results presented in this paper are not publicly available at this time but may be obtained from the authors upon reasonable request.

Supplemental document. See Supplement 1 for supporting content.

REFERENCES

1. D. Cozzolino, D. Bacco, B. Da Lio, *et al.*, "Orbital angular momentum states enabling fiber-based high-dimensional quantum communication," Phys. Rev. Appl. **11**, 064058 (2019).
2. G. Vallone, V. D'Ambrosio, A. Sponselli, *et al.*, "Free-space quantum key distribution by rotation-invariant twisted photons," Phys. Rev. Lett. **113**, 060503 (2014).
3. M. Mirhosseini, O. S. Magaña-Loaiza, M. N. O'Sullivan, *et al.*, "High-dimensional quantum cryptography with twisted light," New J. Phys. **17**, 033033 (2015).
4. O. S. Magaña Loaiza, M. Mirhosseini, B. Rodenburg, *et al.*, "Amplification of angular rotations using weak measurements," Phys. Rev. Lett. **112**, 200401 (2014).
5. Y. Yan, G. Xie, M. P. Lavery, *et al.*, "High-capacity millimetre-wave communications with orbital angular momentum multiplexing," Nat. Commun. **5**, 4876 (2014).

6. S. Ecker, F. Bouchard, L. Bulla, *et al.*, "Overcoming noise in entanglement distribution," Phys. Rev. X **9**, 041042 (2019).
7. M. Bogdanov, S. Dimakov, A. Gorlanov, *et al.*, "Correction of segmented mirror aberrations by phase conjugation and dynamic holography," Opt. Commun. **129**, 405–413 (1996).
8. Y. Liu, C. Ma, Y. Shen, *et al.*, "Focusing light inside dynamic scattering media with millisecond digital optical phase conjugation," Optica **4**, 280–288 (2017).
9. Z. Yu, M. Xia, H. Li, *et al.*, "Implementation of digital optical phase conjugation with embedded calibration and phase rectification," Sci. Rep. **9**, 1537 (2019).
10. D. S. Simon, C. A. Fitzpatrick, and A. V. Sergienko, "Discrimination and synthesis of recursive quantum states in high-dimensional Hilbert spaces," Phys. Rev. A **91**, 043806 (2015).
11. E. Nagali, F. Sciarrino, F. De Martini, *et al.*, "Quantum information transfer from spin to orbital angular momentum of photons," Phys. Rev. Lett. **103**, 013601 (2009).
12. M. R. Fewings and A. L. Gaeta, "Compensation of pulse distortions by phase conjugation via difference-frequency generation," J. Opt. Soc. Am. B **17**, 1522–1525 (2000).
13. S. Gasparoni, J.-W. Pan, P. Walther, *et al.*, "Realization of a photonic controlled-not gate sufficient for quantum computation," Phys. Rev. Lett. **93**, 020504 (2004).
14. H. Zhou, Y. Duan, H. Song, *et al.*, "Automatic turbulence mitigation for coherent free-space optical links using crystal-based phase conjugation and fiber-coupled data modulation," Opt. Lett. **48**, 2194–2197 (2023).
15. Y. Zhou, J. Zhao, B. Braverman, *et al.*, "Multiprobe time reversal for high-fidelity vortex-mode-division multiplexing over a turbulent free-space link," Phys. Rev. Appl. **15**, 034011 (2021).
16. X. Liu, A. R. Chraplyvy, P. J. Winzer, *et al.*, "Phase-conjugated twin waves for communication beyond the kerr nonlinearity limit," Nat. Photonics **7**, 560–568 (2013).
17. N. Leonhard, G. Sorelli, V. N. Shatokhin, *et al.*, "Protecting the entanglement of twisted photons by adaptive optics," Phys. Rev. A **97**, 012321 (2018).
18. P. H. S. Ribeiro, S. Pádua, and C. H. Monken, "Image and coherence transfer in the stimulated down-conversion process," Phys. Rev. A **60**, 5074–5078 (1999).
19. Y. Xu, S. Tang, A. N. Black, *et al.*, "Orthogonal spatial coding with stimulated parametric down-conversion," Opt. Express **31**, 42723–42729 (2023).
20. T. Permaul, A. Forbes, and T. Konrad, "Quantum optical formulation of difference-frequency generation and optimal cloning of spatial modes," arXiv (2025).
21. A. Zavatta, S. Viciani, and M. Bellini, "Quantum-to-classical transition with single-photon-added coherent states of light," Science **306**, 660–662 (2004).
22. D. Wang, E. H. Zhou, J. Brake, *et al.*, "Focusing through dynamic tissue with millisecond digital optical phase conjugation," Optica **2**, 728–735 (2015).
23. G. Cerullo and S. De Silvestri, "Ultrafast optical parametric amplifiers," Rev. Sci. Instrum. **74**, 1–18 (2003).
24. M. T. Turnbull, P. G. Petrov, C. S. Embrey, *et al.*, "Role of the phase-matching condition in nondegenerate four-wave mixing in hot vapors for the generation of squeezed states of light," Phys. Rev. A **88**, 033845 (2013).
25. X. Qiu, H. Guo, Y. Ren, *et al.*, "High-dimensional photonic orbital-angular-momentum frequency interface," Phys. Rev. Appl. **19**, 044072 (2023).
26. M. Tsang, "Spectral phase conjugation via extended phase matching," J. Opt. Soc. Am. B **23**, 861–867 (2006).
27. Z. Y. Ou, L. J. Wang, and L. Mandel, "Photon amplification by parametric downconversion," J. Opt. Soc. Am. B **7**, 211–214 (1990).
28. A. Mair, A. Vaziri, G. Weihs, *et al.*, "Entanglement of the orbital angular momentum states of photons," Nature **412**, 313–316 (2001).
29. L. Kopf, R. Barros, S. Prabhakar, *et al.*, "Conservation of angular momentum on a single-photon level," Phys. Rev. Lett. **134**, 203601 (2025).
30. S. P. Walborn, A. N. de Oliveira, R. S. Thebaldi, *et al.*, "Entanglement and conservation of orbital angular momentum in spontaneous parametric down-conversion," Phys. Rev. A **69**, 023811 (2004).
31. J. P. Torres, A. Alexandrescu, and L. Torner, "Quantum spiral bandwidth of entangled two-photon states," Phys. Rev. A **68**, 050301 (2003).
32. F. M. Miatto, A. M. Yao, and S. M. Barnett, "Full characterization of the quantum spiral bandwidth of entangled biphotons," Phys. Rev. A **83**, 033816 (2011).
33. D. P. Caetano, M. P. Almeida, P. H. Souto Ribeiro, *et al.*, "Conservation of orbital angular momentum in stimulated down-conversion," Phys. Rev. A **66**, 041801 (2002).
34. C. H. Monken, P. H. S. Ribeiro, and S. Pádua, "Transfer of angular spectrum and image formation in spontaneous parametric down-conversion," Phys. Rev. A **57**, 3123–3126 (1998).
35. M. Liscidini and J. E. Sipe, "Stimulated emission tomography," Phys. Rev. Lett. **111**, 193602 (2013).
36. A. de Oliveira, G. Santos, N. R. da Silva, *et al.*, "Beyond conservation of orbital angular momentum in stimulated parametric down-conversion," Phys. Rev. Appl. **16**, 044019 (2021).
37. L. S. Tey, S. V. Muniandy, and W. Y. Chong, "Distinguishing photon-count fluctuation characteristics of classical and quantum light sources using non-markovian processes," Phys. Rev. E **111**, 044138 (2025).
38. R. Uppu, F. T. Pedersen, Y. Wang, *et al.*, "Scalable integrated single-photon source," Sci. Adv. **6**, eabc8268 (2020).
39. N. Somaschi, V. Giesz, L. De Santis, *et al.*, "Near-optimal single-photon sources in the solid state," Nat. Photonics **10**, 340–345 (2016).
40. K. H. Madsen, S. Ates, J. Liu, *et al.*, "Efficient out-coupling of high-purity single photons from a coherent quantum dot in a photonic-crystal cavity," Phys. Rev. B **90**, 155303 (2014).
41. O. Slattery, L. Ma, K. Zong, *et al.*, "Background and review of cavity-enhanced spontaneous parametric down-conversion," J. Res. Natl. Inst. Stand. Technol. **124**, 1–18 (2019).
42. E. Pomarico, B. Sanguinetti, T. Guerreiro, *et al.*, "Mhz rate and efficient synchronous heralding of single photons at telecom wavelengths," Opt. Express **20**, 23846–23855 (2012).
43. Y. Xu, S. Choudhary, and R. W. Boyd, "Stimulated emission tomography for efficient characterization of spatial entanglement," Phys. Rev. Res. **6**, L042047 (2024).

Supplemental Document

Journal of the Optical Society of America B OPTICAL PHYSICS

Description of single-photon orbital angular momentum conjugation with stimulated parametric down-conversion [Invited]: supplement

TOBEY J. B. LUCK,[1,*] AARÓN A. AGUILAR-CARDOSO,[1] CHENG LI,[1] MANUEL F. FERRER-GARCIA,[1] JEREMY UPHAM,[1] JEFF S. LUNDEEN,[1,2] AND ROBERT W. BOYD[1,3]

[1]*Nexus for Quantum Technologies, Department of Physics, University of Ottawa, Ottawa K1N 6N5, Ontario, Canada*
[2]*National Research Council of Canada, 100 Sussex Drive, Ottawa, Ontario K1A 0R6, Canada*
[3] *niversity of Rochester, Rochester, 14627, New York, USA*

This supplement published with Optica Publishing Group on 11 December 2025 by The Authors under the terms of the Creative Commons Attribution 4.0 License in the format provided by the authors and unedited. Further distribution of this work must maintain attribution to the author(s) and the published article's title, journal citation, and DOI.

Supplement DOI: https://doi.org/10.6084/m9.figshare.30724652

Parent Article DOI: https://doi.org/10.1364/JOSAB.578036

Supplementary Information for: *Description of Single-Photon Orbital Angular Momentum Conjugation with Stimulated Parametric Down-Conversion*

Tobey J.B. Luck[1], Aarón A. Aguilar-Cardoso[1], Cheng Li[1], Manuel F. Ferrer-Garcia[1], Jeremy Upham[1], Jeff S. Lundeen[1,2], and Robert W. Boyd[1,3]

[1]Nexus for Quantum Technologies, Department of Physics, University of Ottawa, Ottawa, K1N 6N5, ON, Canada
[2]National Research Council of Canada, 100 Sussex Drive, Ottawa, Ontario K1A 0R6, Canada
[3]Institute of Optics, University of Rochester, Rochester, NY 14627, USA

S1 Solving the spontaneous LG overlap integral

In this section, we analytically solve the overlap integral in the spontaneous term in the sum of Eq. (6) in the main text. Specifically,

$$\mathcal{N}_{p_i}^{\ell_i} = |C|^2 \iiint d^2\mathbf{q}_i d^2\mathbf{q'}_i d^2\mathbf{q}_s \tilde{W}_d(\mathbf{q}_i+\mathbf{q}_s)\tilde{W}_d^*(\mathbf{q'}_i+\mathbf{q}_s)\tilde{LG}_{p_i}^{\ell_i}(\mathbf{q}_i)\left[\tilde{LG}_{p_i}^{\ell_i}(\mathbf{q'}_i)\right]^*. \tag{S1}$$

First, the integral over $\mathbf{q}_s$ can be evaluated,

$$\begin{aligned}
&\int d^2\mathbf{q}_s \tilde{W}_d(\mathbf{q}_i+\mathbf{q}_s)\tilde{W}_d^*(\mathbf{q'}_i+\mathbf{q}_s) = \frac{w_d^2}{2\pi}\int d^2\mathbf{q}_s e^{-w_d^2|\mathbf{q}_i+\mathbf{q}_s|^2/4} e^{-w_d^2|\mathbf{q'}_i+\mathbf{q}_s|^2/4} \\
&= \frac{w_d^2}{2\pi}\int d^2\mathbf{q}_s e^{-w_d^2(2|\mathbf{q}_s+(\mathbf{q}_i+\mathbf{q'}_i)/2|^2+|\mathbf{q}_i-\mathbf{q'}_i|^2/2)/4} \\
&= \frac{w_d^2}{2\pi} e^{-w_d^2|\mathbf{q}_i-\mathbf{q'}_i|^2/8}\int d^2\mathbf{q}_s e^{-w_d^2(|\mathbf{q}_s+(\mathbf{q}_i+\mathbf{q'}_i)/2|^2)/2} \\
&= e^{-w_d^2|\mathbf{q}_i-\mathbf{q'}_i|^2/8}.
\end{aligned} \tag{S2}$$

Now Eq. (S1) can be evaluated as a double integral over $\mathbf{q}_i$ and $\mathbf{q'}_i$

$$\begin{aligned}
&\mathcal{N}_{p_i}^{\ell_i} = |C|^2 \iint d^2\mathbf{q}_i d^2\mathbf{q'}_i e^{-w_d^2|\mathbf{q}_i-\mathbf{q'}_i|^2/8}\tilde{LG}_{p_i}^{\ell_i}(\mathbf{q}_i)\left[\tilde{LG}_{p_i}^{\ell_i}(\mathbf{q'}_i)\right]^* \\
&= \int_{q_i=0}^{\infty} dq_i \int_{\phi_i=0}^{2\pi} q_i d\phi_i \int_{q_i'=0}^{\infty} dq_i' \int_{\phi_i'=0}^{2\pi} q_i' d\phi_i' e^{-w_d^2|\mathbf{q}_i-\mathbf{q'}_i|^2/8}\sqrt{\frac{w_i^2 p_i!}{2\pi(p_i+|\ell_i|)!}}\sqrt{\frac{{w_i'}^2 p_i!}{2\pi(p_i+|\ell_i|)!}} \\
&\times \left(\frac{w_i q_i}{\sqrt{2}}\right)^{|\ell_i|}\left(\frac{w_i' q_i'}{\sqrt{2}}\right)^{|\ell_i|} e^{-w_i^2 q_i^2/4} e^{-{w_i'}^2 {q_i'}^2/4}(-1)^{p_i+p_i} L_{p_i}^{|\ell_i|}\left(\frac{w_i^2 q_i^2}{2}\right) L_{p_i}^{|\ell_i|}\left(\frac{{w_i'}^2 {q_i'}^2}{2}\right) \\
&\times e^{i\ell_i(\phi_i+\pi/2)} e^{-i\ell_i(\phi_i'+\pi/2)}.
\end{aligned} \tag{S3}$$

The exponential kernel can be written in polar coordinates by making the substitution $|\mathbf{q}_i - \mathbf{q}_i'|^2 = q_i^2 + {q_i'}^2 - 2q_i q_i' \cos(\phi_i - \phi_i')$. The kernel now depends on the radial coordinates in momentum space, q_i and q_i', and on the difference between azimuthal angles, $\phi_i - \phi_i'$. We can then write the kernel as a superposition of plane waves with phase $\exp\{i\ell(\phi_i - \phi_i')\}$ [1]

$$e^{-w_d^2(q_i^2+{q_i'}^2-2q_iq_i'\cos(\phi_i-\phi_i'))/8} = \sum_{\ell'=-\infty}^{\infty} f_{\ell'}(q_i, q_i') e^{i\ell'(\phi_i-\phi_i')}. \tag{S4}$$

Where the Fourier coefficient $f_{\ell'}(q_i, q_i')$ has the form

$$\begin{aligned} f_{\ell'}(q_i, q_i') &= \frac{1}{2\pi}\int_0^{2\pi} d\phi\, e^{-w_d^2(q_i^2+{q_i'}^2-2q_iq_i'\cos\phi)/8} e^{i\ell'\phi} \\ &= \frac{1}{2\pi} e^{-w_d^2(q_i^2+{q_i'}^2)/8} \int_0^{2\pi} d\phi\, e^{w_d^2 q_i q_i' \cos\phi/4} e^{i\ell'\phi}. \end{aligned} \tag{S5}$$

This is a standard integral representation of the modified Bessel function of the first kind

$$I_\ell(z) = \frac{1}{2\pi}\int_0^{2\pi} e^{z\cos\phi} e^{i\ell\phi} d\phi, \tag{S6}$$

so we obtain

$$f_{\ell'}(q_i, q_i') = e^{-w_d^2(q_i^2+{q_i'}^2)/8} I_{\ell'}\left(\frac{w_d^2 q_i q_i'}{4}\right). \tag{S7}$$

The integral then becomes

$$\begin{aligned} \mathcal{N}_{p_i}^{\ell_i} &= \frac{|C|^2 w_i w_i' p_i!}{2\pi(p_i+|\ell_i|)!}\left(\frac{w_i w_i'}{2}\right)^{|\ell_i|} \int_{q_i=0}^{\infty}\int_{q_i'=0}^{\infty} dq_i dq_i' (q_i q_i')^{|\ell_i|+1} e^{-w_i^2 q_i^2/4} e^{-{w_i'}^2 {q_i'}^2/4} L_{p_i}^{|\ell_i|}\left(\frac{w_i^2 q_i^2}{2}\right) \\ &\times L_{p_i}^{|\ell_i|}\left(\frac{{w_i'}^2 {q_i'}^2}{2}\right) \sum_{\ell'=-\infty}^{\infty} e^{-w_d^2(q_i^2+{q_i'}^2)/8} I_{\ell'}\left(\frac{w_d^2 q_i q_i'}{4}\right) \int_{\phi_i=0}^{2\pi}\int_{\phi_i'=0}^{2\pi} d\phi_i d\phi_i' e^{i\ell'(\phi_i-\phi_i')} e^{i\ell_i(\phi_i+\pi/2)} \\ &\times e^{-i\ell_i(\phi_i'+\pi/2)}. \end{aligned} \tag{S8}$$

With the angular integral now expressing the form

$$\sum_{\ell'=-\infty}^{\infty} e^{-w_d^2(q_i^2+{q_i'}^2)/8} I_{\ell'}\left(\frac{w_d^2 q_i q_i'}{4}\right) \int_{\phi_i=0}^{2\pi} d\phi_i e^{i\phi_i(\ell'+\ell_i)} e^{i\ell_i\pi/2} \int_{\phi_i'=0}^{2\pi} d\phi_i' e^{-i\phi_i'(\ell'+\ell_i)} e^{-i\ell_i\pi/2}. \tag{S9}$$

Due to the orthogonality of exponential functions $\int_0^{2\pi} e^{i\phi} d\phi = 2\pi\delta_\phi$, the angular integral evaluates to

$$\sum_{\ell'=-\infty}^{\infty} e^{-w_d^2(q_i^2+{q_i'}^2)/8} I_{\ell'}\left(\frac{w_d^2 q_i q_i'}{4}\right) 4\pi^2 \delta_{\ell',-\ell_i}\delta_{\ell',-\ell_i}. \tag{S10}$$

Under integer indices, $I_\ell(\cdot) = I_{-\ell}(\cdot) = I_{|\ell|}(\cdot)$. The remaining radial integral then simplifies to

$$\begin{aligned} \mathcal{N}_{p_i}^{\ell_i} &= \frac{2\pi|C|^2 w_i w_i' p_i!}{(p_i+|\ell_i|)!}\left(\frac{w_i w_i'}{2}\right)^{|\ell_i|} \int_{q_i=0}^{\infty} dq_i e^{-(w_d^2+2w_i^2)q_i^2/8} q_i^{|\ell_i|+1} L_{p_i}^{|\ell_i|}\left(\frac{w_i^2 q_i^2}{2}\right) \\ &\times \int_{q_i'=0}^{\infty} dq_i' e^{-(w_d^2+2{w_i'}^2){q_i'}^2/8} (q_i')^{|\ell_i|+1} L_{p_i}^{|\ell_i|}\left(\frac{{w_i'}^2 {q_i'}^2}{2}\right) I_{|\ell_i|}\left(\frac{w_d^2 q_i q_i'}{4}\right). \end{aligned} \tag{S11}$$

The term $I_{|\ell_i|}\left(w_d^2 q_i q_i'/4\right)$ can be expanded as a series

$$I_{|\ell_i|}\left(\frac{w_d^2 q_i q_i'}{4}\right) = \sum_{r=0}^{\infty} \frac{1}{r!\Gamma(r+|\ell_i|+1)}\left(\frac{w_d^2 q_i q_i'}{8}\right)^{2r+|\ell_i|} \tag{S12}$$
$$= \sum_{r=0}^{\infty} \frac{1}{r!\Gamma(r+|\ell_i|+1)}\left(\frac{w_d^2}{8}\right)^{2r+|\ell_i|} (q_i)^{2r+|\ell_i|}\left(q_i'\right)^{2r+|\ell_i|}.$$

This allows for the integrals over q_i and q_i' to be completely decoupled

$$\mathcal{N}_{p_i}^{\ell_i} = \frac{2\pi|C|^2 w_i w_i' p_i!}{(p_i+|\ell_i|)!}\left(\frac{w_i w_i'}{2}\right)^{|\ell_i|}\sum_{r=0}^{\infty}\frac{(w_d^2/8)^{2r+|\ell_i|}}{r!\Gamma(r+|\ell_i|+1)}\int_{q_i=0}^{\infty} dq_i e^{-(w_d^2+2w_i^2)q_i^2/8} q_i^{2|\ell_i|+2r+1} \tag{S13}$$
$$\times L_{p_i}^{|\ell_i|}\left(\frac{w_i^2 q_i^2}{2}\right)\int_{q_i'=0}^{\infty} dq_i' e^{-(w_d^2+2{w_i'}^2){q_i'}^2/8} {q_i'}^{2|\ell_i|+2r+1} L_{p_i}^{|\ell_i|}\left(\frac{{w_i'}^2{q_i'}^2}{2}\right).$$

The integrals over q_i and q_i' are identical, aside from the change of indices. These integrals can be evaluated individually; we will now evaluate the general integral.

$$\mathcal{B} = \int_0^{\infty} dq e^{-(w_d^2+2w^2)q^2/8} q^{2|\ell|+2r+1} L_p^{|\ell|}\left(\frac{w^2q^2}{2}\right). \tag{S14}$$

Substituting $x = q^2w^2/2$ such that $dq = dx/(qw^2)$, and $q^{2|\ell|+2r} = (2/w^2)^{|\ell|+r}x^{|\ell|+r}$

$$\mathcal{B} = \int_0^{\infty} dx \frac{1}{w^2}\left(\frac{2}{w^2}\right)^{|\ell|+r} e^{-x(w_d^2+2w^2)/4w^2} x^{|\ell|+r} L_p^{|\ell|}(x). \tag{S15}$$

Adapting Gradshteyn & Ryzhik 7.414.7 [2]

$$\int_0^{\infty} e^{-st} t^{\beta} L_n^{\alpha}(t) dt = \frac{\Gamma(\beta+1)\Gamma(\alpha+n+1)}{n!\Gamma(\alpha+1)} s^{-\beta-1} {}_2F_1\left[-n, \beta+1; \alpha+1; \frac{1}{s}\right], \tag{S16}$$

which converges for $\mathrm{Re}(\beta) > -1$ and $\mathrm{Re}(s) > 0$, for our parameters yields

$$\mathcal{B} = 2^{3|\ell|+3r+2}\left(\frac{1}{w_d^2+2w^2}\right)^{|\ell|+r+1}\frac{\Gamma\left(|\ell|+r+1\right)\Gamma(|\ell|+p+1)}{p!\Gamma(|\ell|+1)} \tag{S17}$$
$$\times {}_2F_1\left[-p, |\ell|+r+1; |\ell|+1; \frac{4w^2}{w_d^2+2w^2}\right].$$

Where

$$\mathrm{Re}\left(\frac{w_d^2+2w^2}{4w^2}\right) > 0, \tag{S18}$$

since w_d and w describe waist parameters which are strictly real valued, non-zero numbers, and

$$\mathrm{Re}(|\ell|+r) > -1, \tag{S19}$$

since $|\ell|$ and r both range from $[0, \infty]$. Therefore, we can express the integral $\mathcal{N}_{p_i}^{\ell_i}$ as

$$\mathcal{N}_{p_i}^{\ell_i} = |C|^2\sum_{r=0}^{\infty}\frac{2^{2|\ell_i|+5}\pi\Gamma^2(|\ell_i|+p_i+1)\Gamma\left(|\ell_i|+r+1\right)}{r!p_i!(p_i+|\ell_i|)!\Gamma^2(|\ell_i|+1)} w_d^{4r+2|\ell_i|}(w_i w_i')^{|\ell_i|+1} \tag{S20}$$
$$\times\left(\frac{1}{(w_d^2+2w_i^2)(w_d^2+2{w_i'}^2)}\right)^{|\ell_i|+r+1} {}_2F_1\left[-p_i, |\ell_i|+r+1; |\ell_i|+1; \frac{4w_i^2}{w_d^2+2w_i^2}\right]$$
$$\times {}_2F_1\left[-p_i, |\ell_i|+r+1; |\ell_i|+1; \frac{4{w_i'}^2}{w_d^2+2{w_i'}^2}\right].$$

S2 Solving the stimulated LG overlap integral

In this section, we analytically solve the overlap integrals in the stimulated term in Eq. (6) in the main text. Thus, solving the integral

$$\mathcal{M}_{p_i,p_{se}}^{\ell_i,\ell_{se}} = C\iint d^2\mathbf{q}_i d^2\mathbf{q}_{se}\tilde{W}_d(\mathbf{q}_i+\mathbf{q}_{se})\tilde{LG}_{p_i}^{\ell_i}(\mathbf{q}_i)\tilde{LG}_{p_{se}}^{\ell_{se}}(\mathbf{q}_{se}) \tag{S21}$$

$$= \int_{q_i=0}^{\infty} dq_i \int_{\phi_i=0}^{2\pi} q_i d\phi_i \int_{q_{se}=0}^{\infty} dq_{se} \int_{\phi_{se}=0}^{2\pi} q_{se} d\phi_{se} \frac{w_d}{\sqrt{2\pi}} e^{-w_d^2|\mathbf{q}_i+\mathbf{q}_{se}|^2/4} \sqrt{\frac{w_i^2 p_i!}{2\pi(p_i+|\ell_i|)!}}$$

$$\times \sqrt{\frac{w_{se}^2 p_{se}!}{2\pi(p_{se}+|\ell_{se}|)!}} \left(\frac{w_i q_i}{\sqrt{2}}\right)^{|\ell_i|} \left(\frac{w_{se} q_{se}}{\sqrt{2}}\right)^{|\ell_{se}|} e^{-w_i^2 q_i^2/4} e^{-w_{se}^2 q_{se}^2/4} (-1)^{p_i+p_{se}} L_{p_i}^{|\ell_i|}\left(\frac{w_i^2 q_i^2}{2}\right)$$

$$\times L_{p_{se}}^{|\ell_{se}|}\left(\frac{w_{se}^2 q_{se}^2}{2}\right) e^{i\ell_i(\phi_i+\pi/2)} e^{i\ell_{se}(\phi_{se}+\pi/2)}.$$

This integral closely matches the integral solved earlier in Eq. (S3) with a few minor changes: the kernel $\exp\{-w_d^2|\mathbf{q}_i-\mathbf{q'}_i|^2/8\}$ is replaced by the pump function $(w_d/\sqrt{2})\exp\{-w_d^2|\mathbf{q}_i+\mathbf{q}_{se}|^2/4\}$, the indices of the LG modes are not identical, and the modulus squared of the coefficients for the nonlinear process $|C|^2$ is replaced by C. Despite these changes, the same overall approach can be used to solve this integral. Solving the azimuthal integrals yields $\delta_{\ell',\ell_i}\delta_{\ell',-\ell_{se}}$ which forces the azimuthal phase-conjugation effect as the azimuthal index of the idler is constrained to be the negation of the azimuthal index of the seed photon $\ell_i = -\ell_{se}$. Following through with the rest of the calculation performed in Section (S1), we can express the integral as

$$\mathcal{M}_{p_i,p_{se}}^{\ell_i,\ell_{se}} = \delta_{\ell_i,-\ell_{se}} C \sum_{r=0}^{\infty} \frac{2^{|\ell_i|+2}\Gamma(|\ell_i|+p_i+1)\Gamma(|\ell_i|+p_{se}+1)\Gamma(|\ell_i|+r+1)}{r!\Gamma^2(|\ell_i|+1)} \tag{S22}$$

$$\times \sqrt{\frac{2\pi}{p_i! p_{se}!(p_i+|\ell_i|)!(p_{se}+|\ell_i|)!}} w_d^{4r+2|\ell_i|+1} (w_i w_{se})^{|\ell_i|+1} (-1)^{p_i+p_{se}+|\ell_i|}$$

$$\times \left(\frac{1}{(w_d^2+w_i^2)(w_d^2+w_{se}^2)}\right)^{|\ell_i|+r+1} {}_2F_1\left[-p_i, |\ell_i|+r+1; |\ell_i|+1; \frac{2w_i^2}{w_d^2+w_i^2}\right]$$

$$\times {}_2F_1\left[-p_{se}, |\ell_i|+r+1; |\ell_i|+1; \frac{2w_{se}^2}{w_d^2+w_{se}^2}\right].$$

S3 Measuring a single output mode from SPDC

A term that appears multiple times in this study is $\mathcal{N}_p^{\ell}$, which corresponds to the triple overlap integral in Eq. (S1). This term is distinct from the spiral spectrum and arises from a SPDC process in which only one of the output modes is measured. In this section, we derive how this term appears in SPDC when only measuring the idler mode, which gives the term more context for when it appears in other sections of the study. The process is modeled in Figure (S1). The mean photon number associated with measuring down-converted idler photons in mode $\tilde{LG}_{p_i}^{\ell_i}$ can be found by calculating the overlap $[N_{p_i}^{\ell_i}]_{\text{SPDC}} = \langle\psi_{\text{SPDC}}|\hat{n}(\mathbf{q}_i,(\ell_i,p_i))|\psi_{\text{SPDC}}\rangle$ where the biphoton SPDC state in the monochromatic, paraxial, and thin-crystal approximations is given by [3]

$$|\psi_{\text{SPDC}}\rangle = |0\rangle + C\iint d^2\mathbf{q}_i d^2\mathbf{q}_s \tilde{W}_d(\mathbf{q}_i+\mathbf{q}_s)|1;\mathbf{q}_i\rangle|1;\mathbf{q}_s\rangle. \tag{S23}$$

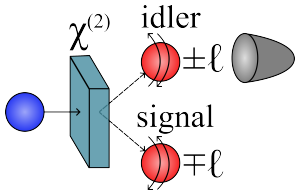


Figure S1: Schematic of the SPDC process in which the average number of photons in the idler mode and in a specificed LG mode are measured.

Due to the orthogonality of the Fock states: $\langle n;\mathbf{q}_1|m;\mathbf{q}_2\rangle = \delta(n-m)\delta^2(\mathbf{q}_1-\mathbf{q}_2)$ the first three terms in the binomial expansion of the mean photon number vanish. Thus, the remaining term in the mean photon number is given by

$$[N_{p_i}^{\ell_i}]_{\text{SPDC}} = |C|^2 \int\!\!\dots\!\!\int d^2\mathbf{q}_i d^2\mathbf{q'}_i d^2\mathbf{q''}_i d^2\mathbf{q'''}_i d^2\mathbf{q}_s d^2\mathbf{q'}_s \tilde{W}_d(\mathbf{q}_i+\mathbf{q}_s)\tilde{W}_d^*(\mathbf{q'}_i+\mathbf{q'}_s) \tag{S24}$$
$$\times \left[\tilde{LG}_{p_i}^{\ell_i}(\mathbf{q''}_i)\right]^* \tilde{LG}_{p_i}^{\ell_i}(\mathbf{q'''}_i)\langle 1;\mathbf{q'}_i|\hat{a}^\dagger(\mathbf{q''}_i)\hat{a}(\mathbf{q'''}_i)|1;\mathbf{q}_i\rangle\langle 1;\mathbf{q'}_s|1;\mathbf{q_s}\rangle.$$

The orthogonality of the annihilation and creator operators imposes $\delta^2(\mathbf{q'}_i-\mathbf{q''}_i)$ and $\delta^2(\mathbf{q'''}_i-\mathbf{q}_i)$ which collapses the integrals over $\mathbf{q''}_i$ and $\mathbf{q'''}_i$. Additionally, the orthogonality of the Fock states imposes the relation $\langle 1;\mathbf{q'}_s|1;\mathbf{q_s}\rangle = \delta^2(\mathbf{q'}_s-\mathbf{q}_s)$ The resulting mean photon number is then

$$[N_{p_i}^{\ell_i}]_{\text{SPDC}} = |C|^2 \iiint d^2\mathbf{q}_i d^2\mathbf{q'}_i d^2\mathbf{q}_s \tilde{W}_d(\mathbf{q}_i+\mathbf{q}_s)\tilde{W}_d^*(\mathbf{q'}_i+\mathbf{q}_s)\tilde{LG}_{p_i}^{\ell_i}(\mathbf{q}_i)\left[\tilde{LG}_{p_i}^{\ell_i}(\mathbf{q'}_i)\right]^*, \tag{S25}$$

which directly matches the form of the double integrals found in the first term in Eq. (6) in the main text and are analytically solved in Eq. (S20).

S4 Spiral spectrum in SPDC

The spiral spectrum in SPDC refers to the coincidence amplitudes associated with measuring down-converted idler-signal photon pairs in SPDC, $\mathcal{M}_{p_i,p_s}^{\ell_i,\ell_s}$[1]. In the low-gain regime of SPDC, where the biphoton state contains exactly one signal-idler pair, the mean photon number of the joint number operator in specified Laguerre-Gaussian modes is equal to the detection probability for those modes. This is because the mean photon number reduces to the squared modulus of the projection amplitude of the biphoton state onto those modes, which directly yields the probability: $[N_{p_i,p_s}^{\ell_i,\ell_s}]_{\text{SPDC}} = [P_{p_i,p_s}^{\ell_i,\ell_s}]_{\text{SPDC}} = |\mathcal{M}_{p_i,p_s}^{\ell_i,\ell_s}|^2$. The mean photon number associated with measuring down-converted idler-signal photon pairs in specified LG modes can be found by calculating the overlap $[N_{p_i,p_s}^{\ell_i,\ell_s}]_{\text{SPDC}} = \langle\psi_{\text{SPDC}}|\hat{n}(\mathbf{q}_i,(\ell_i,p_i))\hat{n}(\mathbf{q}_s,(\ell_s,p_s))|\psi_{\text{SPDC}}\rangle$ where the biphoton SPDC state in the monochromatic, paraxial, and thin-crystal approximations is given by [3]

$$|\psi_{\text{SPDC}}\rangle = |0\rangle + C\iint d^2\mathbf{q}_i d^2\mathbf{q}_s \tilde{W}_d(\mathbf{q}_i+\mathbf{q}_s)|1;\mathbf{q}_i\rangle|1;\mathbf{q}_s\rangle. \tag{S26}$$

Due to the orthogonality of the Fock states: $\langle n;\mathbf{q}_1|m;\mathbf{q}_2\rangle = \delta(n-m)\delta^2(\mathbf{q}_1-\mathbf{q}_2)$ the first three terms in the binomial expansion of the mean photon number vanish. Thus, the remaining term in

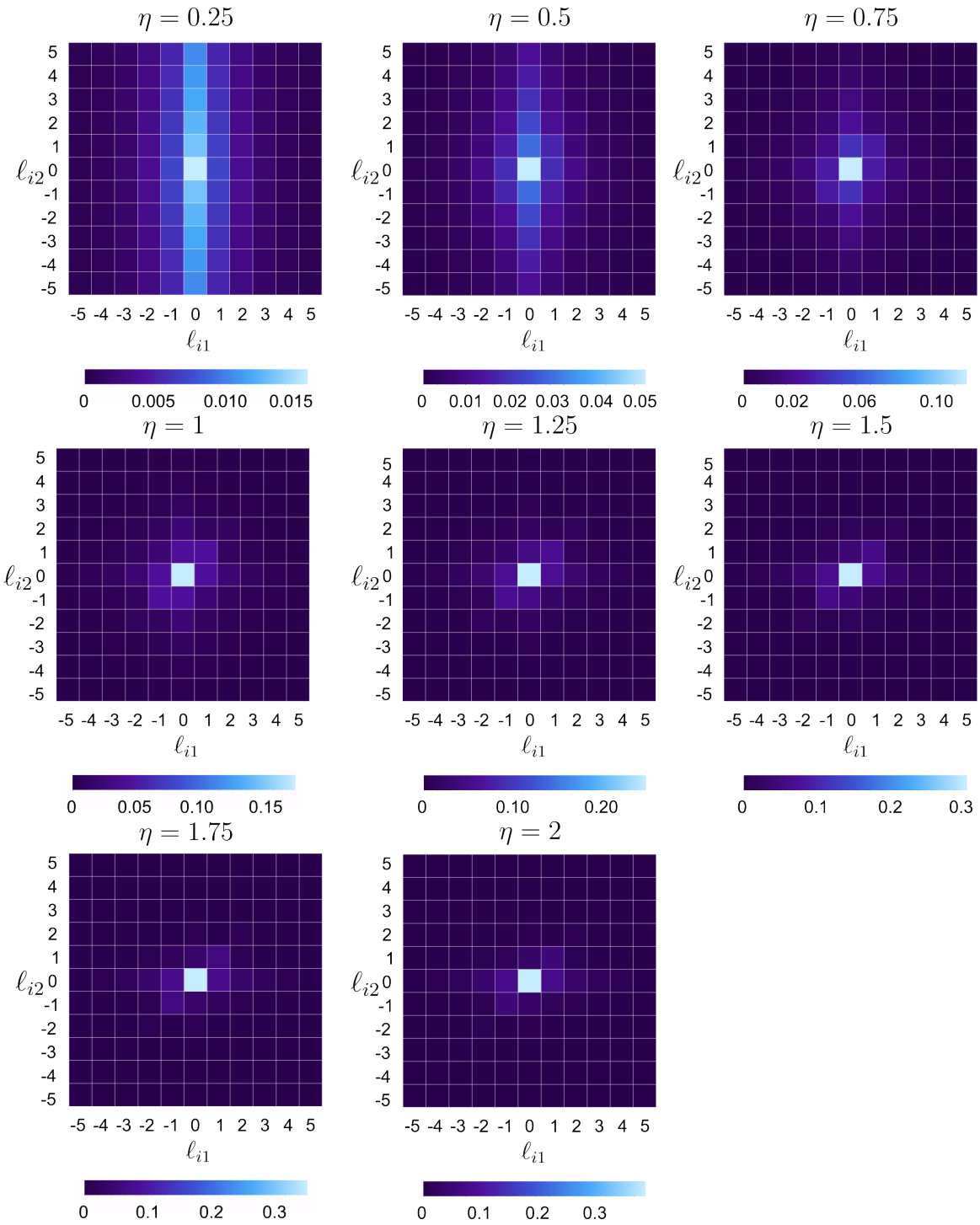


Figure S2: The simulated, joint normalized ($\sum_{\ell_{i1},\ell_{i2}=-\infty}^{\infty}[N_{p_{i1},p_{i2}}^{\ell_{i1},\ell_{i2}}]_{\text{CPDC}} = 1$) mean photon number distribution $[N_{p_{i1},p_{i2}}^{\ell_{i1},\ell_{i2}}]_{\text{CPDC}}$ for $w_{d2} = w_{s1}$ and differing beam waist ratios, $\eta \in [0.25, 0.5, 0.75, 1, 1.25, 1.5, 1.75, 2]$. The z-axis denotes the normalized mean photon number. The enhanced diagonal along $\ell_{i1} = \ell_{i2}$ is more prominent for values of $\eta > 1$. For values of $\eta < 1$, the distribution becomes more broad which obscures the diagonal enhancement. All distributions are plotted with radial indices $p_{i1} = p_{i2} = 0$. 6

the mean photon number is given by

$$[N_{p_i,p_s}^{\ell_i,\ell_s}]_{\text{SPDC}} = CC^* \int\!\dots\!\int d^2\mathbf{q}_i d^2\mathbf{q'}_i d^2\mathbf{q''}_i d^2\mathbf{q'''}_i d^2\mathbf{q}_s d^2\mathbf{q'}_s d^2\mathbf{q''}_s d^2\mathbf{q'''}_s \tilde{W}_d(\mathbf{q}_i+\mathbf{q}_s) \tag{S27}$$
$$\times \tilde{W}_d^*(\mathbf{q'}_i+\mathbf{q'}_s)\left[\tilde{LG}_{p_i}^{\ell_i}(\mathbf{q''}_i)\right]^* \tilde{LG}_{p_i}^{\ell_i}(\mathbf{q'''}_i)\left[\tilde{LG}_{p_s}^{\ell_s}(\mathbf{q''}_s)\right]^* \tilde{LG}_{p_s}^{\ell_s}(\mathbf{q'''}_s)$$
$$\times \langle 1;\mathbf{q'}_i|\hat{a}^\dagger(\mathbf{q''}_i)\hat{a}(\mathbf{q'''}_i)|1;\mathbf{q}_i\rangle\langle 1;\mathbf{q'}_s|\hat{a}^\dagger(\mathbf{q''}_s)\hat{a}(\mathbf{q'''}_s)|1;\mathbf{q_s}\rangle.$$

The action of the ladder operators on the Fock states and the orthogonality of the Fock states imposes $\delta^2(\mathbf{q'}_i-\mathbf{q''}_i)$, $\delta^2(\mathbf{q'''}_i-\mathbf{q}_i)$, $\delta^2(\mathbf{q'}_s-\mathbf{q''}_s)$, and $\delta^2(\mathbf{q'''}_s-\mathbf{q}_s)$ which collapses the integrals over $\mathbf{q''}_i$, $\mathbf{q'''}_i$, $\mathbf{q''}_s$, and $\mathbf{q'''}_s$. The resulting mean photon number is then

$$[N_{p_i,p_s}^{\ell_i,\ell_s}]_{\text{SPDC}} = C\iint d^2\mathbf{q}_i d^2\mathbf{q}_s \tilde{W}_d(\mathbf{q}_i+\mathbf{q}_s)\tilde{LG}_{p_i}^{\ell_i}(\mathbf{q}_i)\tilde{LG}_{p_s}^{\ell_s}(\mathbf{q}_s)C^*\iint d^2\mathbf{q'}_i d^2\mathbf{q'}_s \tilde{W}_d^*(\mathbf{q'}_i+\mathbf{q'}_s) \tag{S28}$$
$$\times\left[\tilde{LG}_{p_i}^{\ell_i}(\mathbf{q'}_i)\right]^*\left[\tilde{LG}_{p_s}^{\ell_s}(\mathbf{q'}_s)\right]^*.$$

Since $[N_{p_i,p_s}^{\ell_i,\ell_s}]_{\text{SPDC}} = \mathcal{M}_{p_i,p_s}^{\ell_i,\ell_s}[\mathcal{M}_{p_i,p_s}^{\ell_i,\ell_s}]^*$ the coincidence amplitudes are then

$$\mathcal{M}_{p_i,p_s}^{\ell_i,\ell_s} = C\iint d^2\mathbf{q}_i d^2\mathbf{q}_s \tilde{W}_d(\mathbf{q}_i+\mathbf{q}_s)\tilde{LG}_{p_i}^{\ell_i}(\mathbf{q}_i)\tilde{LG}_{p_s}^{\ell_s}(\mathbf{q}_s), \tag{S29}$$

which directly matches the form of the double integrals found in the second term in Eq. (6) in the main text and are analytically solved in Eq. (S22).

S5 Exploring the effects of differing beam waist ratios on the CPDC mean photon number distribution

In the main text, all mean photon number distributions were plotted assuming the beam waists in k-space of the LG mode functions are equal to the beam waist of the pump ($w_{d2} = w_{i2} = w'_{i2} = w_{s1} = w_{s2}$) for simplicity. However, previous studies have explored the effects of changing the ratios between the different beam waists on the coincidence amplitudes in SPDC and StimPDC [1, 4]. Since the phase conjugation effect of interest occurs at the second nonlinear crystal, we will investigate the cases for which $w_{d2} = w_{s1}$ and all other beam waists are equal to the same multiple of the pump beam waist, $w_{d2} = \eta w_{i2} = \eta w'_{i2} = \eta w_{s2}$.

The mean photon number distribution as a function of ℓ_{i1} and ℓ_{i2} in the CPDC configuration is plotted in Fig. (S2) for different detection beam waists. The presence of the enhanced diagonal for values of $\eta > 1$ indicates how the beam waist ratio at the second nonlinear crystal can be altered to enhance the phase conjugation effect. We also observe an enhanced horizontal along $\ell_{i2} = 0$ becoming increasingly more prominent as η increases. This is because the weight $\mathcal{N}_{p_{i2}}^{\ell_{i2}}$ in the spontaneous term in $[N_{p_{i1},p_{i2}}^{\ell_{i1},\ell_{i2}}]_{\text{CPDC}}$ tightens quicker about $\ell_{i2} = 0$ with increasing η than $\mathcal{M}_p^\ell$ does. In contrast, values of $\eta < 1$ obscure the enhanced diagonal as both the spontaneous and stimulated terms broaden which increases the relative weight to the off-diagonal terms, thus reducing the relative weight of the diagonal terms upon normalization.

References

[1] F. M. Miatto, A. M. Yao, and S. M. Barnett, "Full characterization of the quantum spiral bandwidth of entangled biphotons," Phys. Rev. A **83**, 033816 (2011).

[2] I. S. Gradshteyn, I. Ryzhik, D. Zwillinger, and V. Moll, *Table of integrals, series, and products; 8th ed.* (Academic Press, Amsterdam, 2015).

[3] P. H. S. Ribeiro, S. Pádua, and C. H. Monken, "Image and coherence transfer in the stimulated down-conversion process," Phys. Rev. A **60**, 5074–5078 (1999).

[4] Y. Xu, S. Choudhary, and R. W. Boyd, "Stimulated emission tomography for efficient characterization of spatial entanglement," Phys. Rev. Res. **6**, L042047 (2024).

Chapter 5

Implications of the Theoretical Findings

5.1 Introduction

The preceding chapters examined whether the phase-conjugation behaviour characteristic of classical stimulated parametric down-conversion can persist when the seeding field is reduced to a single photon. In the classical regime, StimPDC produces an idler field whose transverse structure is proportional to the product $E_p E_s^*$ [12, 42]. Equivalently, in the undepleted-pump, paraxial, and slowly-varying-envelope approximations used in Chapter 3, the generated idler envelope can be written in the form [12, 25, 43]

$$E_i(\mathbf{r}_\perp) \propto \int d^2\mathbf{r}'_\perp \, K(\mathbf{r}_\perp, \mathbf{r}'_\perp)\, E_p(\mathbf{r}'_\perp)\, E_s^*(\mathbf{r}'_\perp), \tag{5.1}$$

where K is an effective spatial response kernel determined by phase matching and propagation through the crystal, and reduces to a response in the thin-crystal limit considered throughout this thesis. In the thin-crystal regime one may write this more explicitly as

$$K(\mathbf{r}_\perp, \mathbf{r}'_\perp) \approx K_0\, \delta^{(2)}(\mathbf{r}_\perp - \mathbf{r}'_\perp), \qquad \Rightarrow \qquad E_i(\mathbf{r}_\perp) \propto K_0\, E_p(\mathbf{r}_\perp)\, E_s^*(\mathbf{r}_\perp), \tag{5.2}$$

which recovers the mean-field product relation derived in Chapter 3. Because the seed is a bright coherent beam with mean photon number $\langle \hat{n}_s \rangle \gg 1$, the stimulated contribution dominates the nonlinear interaction, and the idler inherits the conjugated phase of the seed with high fidelity. This deterministic behaviour enables wavefront reversal and underlies the turbulence-mitigation protocol reviewed in Chapter 3, where phase distortions acquired during free-space propagation are cancelled through reciprocal propagation [7, 9, 10].

When the seed is restricted to a single photon, the physical situation changes qualitatively. As shown in Chapter 4, the stimulated contribution no longer overwhelms the spontaneous background. Instead, both terms appear at the same order in perturbation theory and contribute coherently to the output state [21, 22, 44]. Concretely, in the low-gain regime the evolution operator may be expanded to first order as

$$|\Psi_{\text{out}}\rangle \simeq |\Psi_{\text{in}}\rangle - \frac{i}{\hbar} \int dt\, \hat{H}_{\text{int}}(t) |\Psi_{\text{in}}\rangle, \tag{5.3}$$

and for a seeded input state the single application of $\hat{H}_{\text{int}}$ generates both (i) pair creation from vacuum in the relevant modes (spontaneous emission) and (ii) bosonically enhanced emission into modes overlapping the seeded mode (stimulated emission) [22, 27, 44]. The idler therefore cannot be described by a single transverse mode or

by a classical mean field. Rather, it occupies a superposition of phase-conjugated and non-conjugated components whose relative weights are fixed by the photon-number scaling of the interaction [21, 22, 44].

A compact way to connect this qualitative statement to the mode-resolved theory developed earlier is to recall that, under the undepleted pump approximation, the $\chi^{(2)}$ interaction Hamiltonian has the pair-creation structure [12, 22]

$$\hat{H}_{\mathrm{int}}(t) = \sum_{\mu_i,\mu_s} \kappa_{\mu_i,\mu_s}\, \hat{a}^\dagger_{\mu_i} \hat{a}^\dagger_{\mu_s}\, e^{i(\omega_i+\omega_s-\omega_p)t} + \mathrm{h.c.}, \tag{5.4}$$

which is the same operator form established in Chapter 2. In the LG basis, the couplings κ_{μ_i,μ_s} are governed by the same transverse overlap integrals that define the SPDC spiral spectrum [19, 20, 31]. Chapter 4 showed that, for a single-photon seed, these same overlaps appear in two contributions to idler observables: a seed-independent background and a seed-dependent (phase-conjugated) enhancement.

This chapter synthesizes these results and places them in a broader conceptual and operational context. Section 5.2 contrasts classical and single-photon seeded StimPDC from a photon-number perspective and identifies the emergence of deterministic phase conjugation as a defining feature of the classical limit. Sections 5.3 through 5.5 clarify how this distinction manifests at the levels of scaling behaviour, conditional versus deterministic operations, and fundamental constraints imposed by quantum mechanics. Section 5.7 discusses the consequences for turbulence mitigation and quantum key distribution, while Section 5.8 outlines an experimental direction capable of probing phase-conjugated correlations in the joint-idler statistics of cascaded parametric down-conversion. Together, these results delineate the boundary between classical and quantum regimes of phase conjugation.

5.2 Classical and Single-Photon Seeded StimPDC

The difference between classical and single-photon seeded StimPDC arises from how the stimulated contribution to the nonlinear interaction scales with the photon number in the seeding mode [21, 22]. In the classical regime, the seed contains many photons and can be treated as a complex field amplitude [12, 22]. At the Hamiltonian level, one may write the standard three-wave-mixing interaction as [12, 25]

$$\hat{H}_{\mathrm{int}} \propto \int d^3\mathbf{r} \left[\chi^{(2)} E_p(\mathbf{r})\, \hat{E}_s^{(-)}(\mathbf{r})\, \hat{E}_i^{(-)}(\mathbf{r}) + \mathrm{h.c.}\right], \tag{5.5}$$

and in the classical limit one replaces the seed operator by its coherent amplitude, $\hat{E}_s^{(+)} \to E_s$, so that the effective driving term for the idler becomes proportional to $E_p E_s^*$. The stimulated term in the interaction Hamiltonian then scales with the seed intensity and overwhelms the spontaneous background. In this limit, the idler field is determined almost entirely by the classical product $E_p E_s^*$, producing a deterministic phase conjugated output.

When the seed contains only one photon, this scaling advantage disappears. As shown in Chapter 4, the stimulated contribution to the output state is no longer parametrically larger than the spontaneous contribution. Both terms enter at the same order in perturbation theory through the first-order term in Eq. (5.3) and add coherently at the level of the output state [22, 44]. The stimulated component still carries the conjugated phase structure associated with the seed, but it cannot be

isolated from the spontaneous background. Consequently, the idler does not occupy a single phase conjugated spatial mode.

It is helpful to state this directly at the level of mode-resolved observables. In the SPS-PDC calculation in Chapter 4, and in the analytic evaluation of the overlap integrals, the mean photon number in a chosen idler LG mode (ℓ_i, p_i) takes the form

$$\langle \hat{n}_i(\ell_i, p_i) \rangle = N_{p_i}^{\ell_i} + \delta_{\ell_i, -\ell_{\mathrm{se}}} \, |M_{p_i, p_{\mathrm{se}}}^{\ell_i, -\ell_{\mathrm{se}}}|^2, \tag{5.6}$$

where $N_{p_i}^{\ell_i}$ is the seed-independent spontaneous contribution and $M_{p_i,p_{\mathrm{se}}}^{\ell_i,-\ell_{\mathrm{se}}}$ is the stimulated overlap amplitude associated with a seed photon in mode $(\ell_{\mathrm{se}}, p_{\mathrm{se}})$. The Kronecker factor $\delta_{\ell_i,-\ell_{\mathrm{se}}}$ encodes the phase-conjugation selection rule at the level of the stimulated enhancement: stimulated emission enhances exactly the phase-conjugate OAM sector relative to the seed. Equation (5.6) makes explicit that, for a single-photon seed, the stimulated contribution is an additive correction on top of an unavoidable spontaneous background rather than a parametrically dominant term.

This distinction is a direct consequence of photon-number scaling rather than of imperfect alignment, pump shaping, or modal mismatch. Increasing the brightness of the seed strengthens the stimulated term relative to the spontaneous one, while a single photon cannot do so [21, 44, 30]. The emergence of deterministic phase conjugation therefore marks the transition to the classical limit of the interaction.

5.3 Photon-Number Scaling of Stimulated and Spontaneous Contributions

The qualitative distinction between classical and single-photon stimulated parametric down-conversion originates in how the nonlinear interaction scales with the photon number of the seeding mode. This scaling determines whether the stimulated contribution can dominate over the spontaneous background and therefore whether phase conjugation can be realized in a deterministic sense.

In a $\chi^{(2)}$ interaction driven by a classical pump, the probability amplitude for generating idler photons contains two conceptually distinct contributions. The first is the spontaneous term, which exists even in the absence of any seed and corresponds to vacuum fluctuations driving pair creation [22, 37]. The second is the stimulated term, which arises from the presence of photons in the seeding mode and enhances emission into modes that satisfy the appropriate phase matching and mode-overlap conditions. These two contributions coexist at the operator level and differ only in how their expectation values scale with the seed photon number.

Let $\hat{a}_s$ denote the annihilation operator of the seeded signal mode and let $\langle \hat{n}_s \rangle = \langle \hat{a}_s^\dagger \hat{a}_s \rangle$ be its mean photon number. In the low-gain regime relevant to both classical StimPDC and SPS-PDC, the mean idler photon number in a given spatial mode can be written as

$$\langle \hat{n}_i \rangle = \langle \hat{n}_i \rangle_{\mathrm{sp}} + \langle \hat{n}_i \rangle_{\mathrm{stim}}, \tag{5.7}$$

where the spontaneous contribution $\langle \hat{n}_i \rangle_{\mathrm{sp}}$ is independent of $\langle \hat{n}_s \rangle$, while the stimulated contribution scales linearly with it,

$$\langle \hat{n}_i \rangle_{\mathrm{stim}} \propto \langle \hat{n}_s \rangle. \tag{5.8}$$

This linear scaling is a direct consequence of the bosonic enhancement factor that appears when annihilation operators act on states with nonzero occupation number [27, 30]. A compact way to see this is to note that matrix elements of the form

$\langle n_s - 1|\hat{a}_s|n_s\rangle = \sqrt{n_s}$ enter the first-order transition amplitudes, implying that probabilities contain factors proportional to n_s once squared and averaged [22, 27].

In the classical regime, the seed is a coherent state with $\langle \hat{n}_s \rangle \gg 1$. Under these conditions the stimulated term overwhelms the spontaneous background by many orders of magnitude, and the idler field is effectively determined by the stimulated contribution alone. The idler therefore occupies a well-defined spatial mode proportional to the classical product $E_p E_s^*$, and phase conjugation emerges as a deterministic field-level phenomenon. Formally, one may summarize this limit by the asymptotic scaling

$$\frac{\langle \hat{n}_i \rangle_{\text{stim}}}{\langle \hat{n}_i \rangle_{\text{sp}}} \sim \langle \hat{n}_s \rangle \gg 1, \tag{5.9}$$

so that $\langle \hat{n}_i \rangle \simeq \langle \hat{n}_i \rangle_{\text{stim}}$ in practice.

In contrast, when the seed contains a single photon, $\langle \hat{n}_s \rangle = 1$, the stimulated and spontaneous contributions are of the same order of magnitude. Neither term can be neglected, and the idler field cannot be associated with a single spatial mode determined purely by the seed. Instead, the idler occupies a superposition of modes arising from both the spontaneous background and the weakly enhanced stimulated channel. This coexistence is not a technical limitation but a direct consequence of the photon-number scaling of the interaction, since Eq. (5.9) implies that the stimulated channel cannot become parametrically dominant for $\langle \hat{n}_s \rangle = \mathcal{O}(1)$ [22, 27, 45].

Equation (5.6) provides a mode-resolved realization of this statement: for each detected mode (ℓ_i, p_i) the stimulated enhancement is an additive term on top of a seed-independent $N_{p_i}^{\ell_i}$. A useful figure of merit is therefore the modal stimulated-to-spontaneous ratio,

$$\mathcal{R}_{\ell_i,p_i}(N) \equiv \frac{\langle \hat{n}_i(\ell_i,p_i)\rangle_{\text{stim}}}{\langle \hat{n}_i(\ell_i,p_i)\rangle_{\text{sp}}} = N \cdot \frac{\delta_{\ell_i,-\ell_{\text{se}}} |M_{p_i,p_{\text{se}}}^{\ell_i,-\ell_{\text{se}}}|^2}{N_{p_i}^{\ell_i}}, \tag{5.10}$$

which quantifies the quality of phase conjugation as a function of seed photon number N. At $N = 1$ this ratio is $\mathcal{O}(1)$, confirming that no mode-selective enhancement is possible in the single-photon regime, while $\mathcal{R} \gg 1$ in the classical limit $N \gg 1$ recovers deterministic wavefront reversal.

This scaling argument explains why the classical notion of phase conjugation does not carry over straightforwardly to the single-photon regime. In the absence of a large photon-number asymmetry between stimulated and spontaneous processes, the nonlinear interaction cannot isolate a unique conjugated component of the seed. Any phase conjugated contribution remains embedded within a background of non-conjugated spontaneous emission, preventing deterministic wavefront reversal.

Importantly, this limitation does not imply that phase information is destroyed in the single-photon regime. Rather, it implies that phase conjugation is no longer a property of a mean field, but must instead be understood in terms of quantum correlations and conditional measurements [22]. This distinction underlies the analysis of cascaded parametric down-conversion in Chapter 4, where heralding and joint-detection observables are used to isolate the stimulated contribution that is otherwise hidden by spontaneous emission.

The photon-number scaling discussed here therefore establishes a fundamental boundary between classical and quantum StimPDC. Classical phase conjugation relies on the dominance of stimulated emission, while single-photon operation necessarily involves a regime in which stimulated and spontaneous processes coexist on equal footing [22, 30]. All protocol-level consequences discussed in the remainder of this chapter follow directly from this scaling behaviour.

5.4 Deterministic versus Conditional Phase Conjugation

The photon-number scaling discussed in the previous section implies a fundamental distinction between two qualitatively different notions of phase conjugation: deterministic phase conjugation, which applies in the classical regime, and conditional access to phase-conjugated structure. Clarifying this distinction is essential for interpreting the results of Chapter 4 and for assessing the feasibility of turbulence-mitigation protocols based on stimulated parametric down-conversion [15].

Deterministic phase conjugation refers to a process in which the output field reliably occupies a single spatial mode whose phase is the complex conjugate of the input mode, independent of measurement or post-selection. In classical StimPDC, this condition is satisfied because the seed field is bright enough that stimulated emission into the idler mode overwhelmingly dominates over spontaneous parametric down-conversion. The idler field is therefore well described by a classical complex amplitude proportional to $E_p E_s^*$, and every realization of the process produces a conjugated wavefront. This determinism is what enables wavefront reversal and turbulence cancellation at the level of classical field propagation [7, 9, 10].

In the single-photon regime, this description breaks down. Because the stimulated and spontaneous contributions to the interaction are comparable in magnitude, the idler does not emerge in a single well-defined spatial mode. Instead, the output state contains both conjugated and non-conjugated components that arise from stimulated and spontaneous emission, respectively. As a result, there is no deterministic mapping from an input single-photon state to a uniquely phase-conjugated output field. Any attempt to associate a phase-conjugated wavefunction with the idler alone necessarily neglects the unavoidable contribution of spontaneous emission. One way to formalize this is to note that the reduced state of the idler alone,

$$\rho_i = \mathrm{Tr}_s[|\Psi_{\mathrm{out}}\rangle\langle\Psi_{\mathrm{out}}|]\,, \tag{5.11}$$

contains incoherent weight in multiple spatial modes, so that no single idler mode function can represent the unconditional output [17].

Nevertheless, phase-conjugated structure can still be accessed conditionally. In the CPDC configuration analyzed in Chapter 4, detection of the idler photon generated in the first crystal heralds the presence of a single-photon seed in the second crystal. Crucially, this conditioning does not modify the underlying dynamics of the stimulated or spontaneous emission processes in the second crystal, nor does it increase the relative strength of the stimulated contribution. Instead, heralding filters the measurement record by excluding events in which the second crystal emitted photons purely spontaneously, without a seeding photon present. This distinction can be expressed by comparing an unconditional moment, such as $\langle\hat{n}_{i_2}\rangle$, with a conditional statistic obtained from a coincidence observable. For example, if $\hat{n}_{i_1}$ denotes the photon number in the first idler (heralding) arm and $\hat{n}_{i_2}$ the photon number in the second idler arm, then a conditional mean may be written as

$$\langle\hat{n}_{i_2}\rangle_{\mathrm{cond}} = \frac{\langle\hat{n}_{i_1}\hat{n}_{i_2}\rangle}{\langle\hat{n}_{i_1}\rangle}, \tag{5.12}$$

where the numerator is a coincidence moment that suppresses contributions from uncorrelated background counts.

In a single-crystal SPS-PDC configuration without conditioning, the detected idler

field is dominated by unseeded spontaneous emission events simply because the probability of generating photon pairs in the absence of a seed greatly exceeds the probability of observing a stimulated event associated with a single-photon seed. The stimulated contribution is nevertheless present whenever a seed photon participates in the interaction; it is experimentally obscured by the much larger background of uncorrelated spontaneous emission. The CPDC architecture removes this background by post-selecting only those events for which a seed photon is known to have been present, thereby revealing the stimulated phase-conjugated contribution without altering its physical magnitude. In this sense, heralding changes the effective ensemble over which expectation values are evaluated, rather than changing the microscopic emission amplitudes produced by $\hat{H}_{\mathrm{int}}$.

Chapter 4 makes this separation explicit by writing the experimentally observed (unheralded) SPS-PDC signal in the second crystal as a mixture of "seed-present" and "seed-absent" trials,

$$\langle \hat{n}_i \rangle_{\mathrm{measured}} = \sigma_{\mathrm{sp}} \left(N_{p_i}^{\ell_i} + \delta_{\ell_i,-\ell_{\mathrm{se}}} |M_{p_i,p_{\mathrm{se}}}^{\ell_i,-\ell_{\mathrm{se}}}|^2 \right) + \sigma_{\mathrm{s}}\, N_{p_i}^{\ell_i}, \qquad \sigma_{\mathrm{sp}} + \sigma_{\mathrm{s}} = 1, \tag{5.13}$$

where σ_{sp} is the probability that a seed photon was present, so the stimulated term can contribute, and σ_{s} is the probability that no seed photon was present, so only the spontaneous background appears. In this picture, heralding increases the effective weight of the σ_{sp} branch within the conditioned dataset, making the stimulated (phase-conjugated) enhancement experimentally visible in coincidence observables even though it cannot dominate deterministically on each trial.

Phase conjugation therefore survives at the single-photon level not as a deterministic property of the idler field, but as a conditional feature of measured correlations and joint detection statistics. This distinction reflects a broader theme in quantum optics, where many effects that are directly observable at the classical level require post-selection or coincidence measurements in the quantum regime. Examples include Hong-Ou-Mandel interference, heralded single-photon generation, and entanglement swapping [46, 47, 48]. In all such cases, the underlying physical processes occur independently of the measurement strategy, but their signatures become experimentally accessible only through appropriate conditioning.

From the perspective of turbulence mitigation, this distinction is decisive. Classical phase conjugation enables round-trip cancellation because every realization of the idler field carries the conjugated wavefront. Conditional access to phase-conjugated structure, by contrast, does not guarantee that an individual photon returning through the channel will exhibit the required phase profile. Even when phase-conjugated correlations are present in coincidence measurements, they cannot enforce deterministic cancellation of turbulence-induced distortions on a shot-by-shot basis.

The analysis in Chapter 4 therefore demonstrates that single-photon seeded Stim-PDC admits phase-conjugated structure that is accessible only conditionally, rather than as a deterministic transformation of the idler field. This limitation is not a consequence of experimental inefficiency or imperfect mode matching, but a direct result of the quantum statistics of the interaction. Any protocol that requires deterministic wavefront reversal must therefore operate in a regime where stimulated emission dominates, while genuinely quantum protocols must instead be designed around conditional operations and correlation-based observables.

5.5 Limits of Phase Conjugation as a Quantum Operation

The failure of deterministic phase conjugation in the single-photon regime is not merely a consequence of unfavorable photon-number scaling, but reflects a deeper structural constraint imposed by quantum mechanics. At the level of single-particle wavefunctions, phase conjugation corresponds to complex conjugation of the spatial probability amplitude, $\psi(\mathbf{r}_\perp) \mapsto \psi^*(\mathbf{r}_\perp)$. In quantum theory, however, complex conjugation is not a unitary operation. Instead, it belongs to the class of antiunitary transformations, as formalized by Wigner's theorem [49, 50]. One may write the conjugation map as $|\psi\rangle \mapsto |\psi^*\rangle$, which is anti-linear and therefore cannot be implemented as a unitary operator acting on $|\psi\rangle$.

Wigner's theorem states that any symmetry transformation preserving transition probabilities must be represented by either a unitary or an antiunitary operator. While unitary operators can be generated by physical Hamiltonian evolution, antiunitary operators cannot arise from continuous, deterministic time evolution of a closed quantum system. Physical quantum processes are therefore restricted to completely positive, trace-preserving (CPTP) maps, which may be written in Kraus form as

$$\mathcal{E}(\rho) = \sum_k E_k \rho E_k^\dagger, \qquad \sum_k E_k^\dagger E_k = \mathbb{I}, \tag{5.14}$$

and are generated by unitary interactions with an environment followed by partial tracing [17]. As a result, a universal, deterministic implementation of complex conjugation on an arbitrary and unknown quantum state is forbidden [51].

This restriction has direct implications for phase conjugation. In classical wave optics, phase conjugation is a physically realizable process because classical fields are complex-valued functions rather than quantum states, and the nonlinear interaction can explicitly generate the complex conjugate of a field amplitude. In contrast, at the single-photon level the spatial mode is encoded in a quantum probability amplitude, and conjugation of that amplitude corresponds to an antiunitary transformation. Such an operation cannot be implemented deterministically without measurement or post-selection.

Related results appear in other contexts in quantum information. The universal NOT gate, which maps an arbitrary qubit state to its orthogonal complement and similarly involves complex conjugation in a suitable basis, cannot be implemented perfectly on unknown states [51]. The optimal universal NOT operation is necessarily approximate, reinforcing the general principle that antiunitary transformations cannot be realized exactly as physical quantum channels.

Viewed from this perspective, the results of Chapter 4 are not accidental. The appearance of a non-conjugated spontaneous contribution alongside the stimulated, conjugated term is a manifestation of the fact that stimulated parametric down-conversion cannot isolate an antiunitary operation at the single-photon level. Classical StimPDC effectively bypasses this limitation by operating in a regime where field amplitudes, rather than quantum states, are the relevant objects. When the seed contains only one photon, this distinction disappears, and the underlying antiunitary nature of phase conjugation becomes unavoidable.

This analysis clarifies why deterministic, high-fidelity phase conjugation is fundamentally tied to the classical limit. It also explains why no modification of pump shaping, spatial-mode engineering, or crystal geometry can restore classical behaviour in the single-photon regime. The limitation does not arise from experimental imperfections, but from the structure of quantum mechanics itself.

5.6 Consequences for Phase Conjugation Protocols

Phase conjugation protocols rely on the assumption that the generated field carries a uniquely defined conjugated wavefront. In the classical regime this assumption is justified: the dominance of the stimulated process suppresses all other contributions, and the idler reproduces the conjugated phase of the seed with high fidelity.

In the single-photon regime this condition is not satisfied. Although phase conjugated structure persists within the quantum correlations of the output state, the idler field cannot be described as a deterministic conjugated replica of the input. The spontaneous component of the interaction necessarily contributes, and its presence prevents the isolation of a single conjugated mode. The limitation is therefore operational rather than fundamental: it reflects the impossibility of achieving stimulated dominance with a single-photon seed, as summarized by the scaling relation in Eq. (5.9).

Equation (5.6) makes the same point in the simplest operational language: even in the phase-conjugate OAM sector, the stimulated enhancement appears as an additive correction on top of a seed-independent background. Any protocol requiring a deterministic output mode transformation must therefore operate in a regime where the effective stimulated-to-spontaneous ratio in Eq. (5.10) is $\gg 1$ across the relevant detection modes, which is precisely the classical limit.

This distinction clarifies the boundary between classical and quantum behaviour in StimPDC. Deterministic wavefront reversal is a property of the classical limit, where a mean field description is valid. In contrast, the single-photon regime admits only conditional or correlation-based signatures of conjugation rather than a unique phase conjugated output field.

5.7 Implications for QKD and Turbulence Mitigation

A single-photon version of the turbulence-mitigation protocol reviewed in Chapter 3 would be attractive for quantum key distribution, since the travelling quantum state could not be copied or measured without disturbance [18, 36, 41]. However, the protocol depends critically on the availability of a deterministic phase conjugated idler [15]. Because single-photon seeded StimPDC does not isolate a unique conjugated mode, the returning photon does not reliably reproduce the corrected spatial structure required for turbulence cancellation.

This does not imply that turbulence-induced phase distortions cannot be cancelled at the level of single-photon probability amplitudes. As discussed in Chapter 3, a single photon propagating through a reciprocal channel acquires a well-defined spatial phase [7, 8], and an operation that genuinely implements phase conjugation of the wavefunction would, in principle, enable round-trip cancellation. The limitation identified here is that classical StimPDC does not provide such an operation when seeded by a single photon, because the process yields a mixed idler state of the form in Eq. (5.11) rather than a pure conjugated output.

The analysis in Chapter 4 therefore identifies a practical boundary rather than a fundamental prohibition for protocols that rely on the no-cloning theorem for their security guarantees. It is worth noting, however, that not all QKD protocols derive their security from no-cloning alone. Certain prepare-and-measure protocols based on high-dimensional spatial modes can tolerate classical probes in the channel provided that the information-bearing states themselves remain quantum and that the channel estimation step does not expose the key alphabet [15]. In such schemes, the classical StimPDC turbulence-correction mechanism studied in [15] could in principle be

applied directly to suppress turbulence-induced crosstalk below the security threshold, without requiring single-photon seeding. The boundary identified in this thesis therefore applies specifically to extensions of the protocol in which the probe itself is the quantum information carrier: that extension is precluded by the scaling results of Chapter 4, but the broader family of StimPDC-assisted QKD schemes remains a viable and open direction.

5.8 Experimental Considerations

5.8.1 Preliminary Search for Temporal Correlations in SPDC

Motivated by the central role of temporal correlations in CPDC, an initial experimental effort focused on detecting mode-resolved temporal correlations in SPDC. The goal of this experiment was to test whether projecting the signal and idler photons onto conjugate OAM modes would yield enhanced temporal coincidences, thereby providing a simplified platform for validating mode-dependent correlations prior to implementing CPDC.

A schematic of the experimental setup is shown in Fig. 5.1. A continuous-wave 405 nm Gaussian pump beam with power ~ 40 mW drives Type-II SPDC in a ppKTP crystal. The theoretical framework developed in Chapter 2 assumed a homogeneous nonlinear medium, whereas ppKTP is a periodically poled crystal in which quasi-phase-matching is achieved through a periodic domain inversion rather than birefringence. In the spatial-mode analysis carried out in this thesis, the relevant quantity is the transverse overlap integral, which depends on the pump and signal/idler mode functions but not on the details of the phase-matching mechanism. Periodic poling modifies the effective nonlinearity and the longitudinal phase-matching envelope, both of which enter only as overall scaling factors in the low-gain regime. The transverse-mode selection rules and OAM conservation derived in Chapter 2 therefore apply without modification to the ppKTP geometry used here. The orthogonally polarized signal and idler photons are separated using a polarizing beam splitter, and residual pump light is suppressed using a bandpass filter centered at 800 nm. In each arm, the down-converted beam is expanded to maximize its spatial extent on a SLM, where a phase-only hologram corresponding to a LG mode is applied. After mode projection, each beam is demagnified and coupled into a single-mode fibre connected to a single-photon avalanche diode (SPAD). The detection events from the two SPADs are recorded using a temporal correlator.

In this configuration, angular momentum conservation in SPDC implies $\ell_p = \ell_s + \ell_i = 0$, such that temporal coincidences were expected to be enhanced when the signal and idler photons were projected onto conjugate OAM modes, $\ell_i = -\ell_s$. Experimentally, single-photon count rates of order 10-20 kHz were obtained independently in each arm by optimizing alignment and fibre coupling. However, no statistically significant temporal coincidence peak was observed for any combination of projected OAM modes within the available integration times, varying between 1 to 20 ns.

This outcome highlights a fundamental limitation of single-mode projection measurements in the low-gain SPDC regime. Although both down-converted arms were individually optimized to maximize single-photon count rates, no statistically significant temporal coincidences were observed. A likely explanation arises from the spatial structure of SPDC in the far field, where each down-converted mode occupies a conical emission pattern. Photon pairs generated in SPDC are correlated at diametrically opposite points on this cone [52].

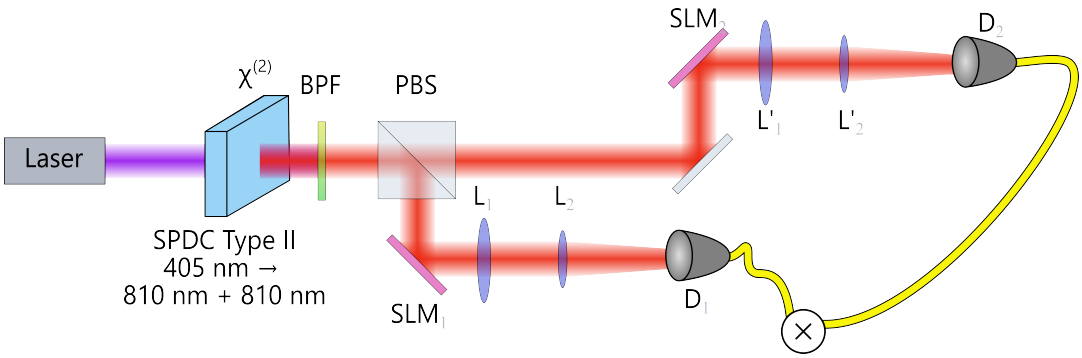


FIGURE 5.1: Preliminary experiment designed to probe mode-resolved temporal correlations in Type-II SPDC. A 405 nm pump drives SPDC in a ppKTP Type-II crystal, producing orthogonally polarized signal and idler photons that are separated using a polarizing beam splitter. Each arm is expanded, projected onto a selected LG mode using an SLM, and coupled into a single-mode fibre connected to a single-photon detector. Detection events are analyzed using a temporal correlator to search for coincidence peaks associated with conjugate OAM projections.

In the present configuration, projection onto single transverse modes using spatial light modulators followed by coupling into single-mode fibres imposes strong spatial filtering. As a result, even when high single-photon rates are obtained in each arm, the two detectors may sample uncorrelated regions of the SPDC emission cone. Under these conditions, the joint detection probability is strongly suppressed, and genuine temporal coincidences become indistinguishable from accidental background counts. This sensitivity to spatial alignment, inherent to single-mode fibre collection, provides a natural explanation for the absence of observable temporal correlations in this measurement.

5.8.2 Joint-Idler Measurements in CPDC

The CPDC theory developed in Chapter 4 predicts that the output of the cascaded interaction contains two idler photons whose joint statistics separate naturally into spontaneous and stimulated contributions. While single-photon seeded StimPDC does not produce a deterministic phase conjugated output field, phase conjugated structure persists within the joint probability amplitudes of the two idlers. Resolving this joint structure experimentally would provide a direct test of the quantum-mechanical origin of the stimulated contribution and would clarify the sense in which phase conjugation survives in the single-photon regime.

A concrete experimental implementation capable of probing these joint-idler correlations is sketched in Fig. 5.2. A continuous-wave 405 nm laser is split on a beam splitter to pump two $\chi^{(2)}$ crystals. The first crystal produces Type-II SPDC at the degenerate wavelength 810 nm. After spectral filtering, a polarizing beam splitter separates the signal and idler photons. The first idler is analyzed using a spatial light modulator (SLM) programmed with a phase pattern corresponding to a chosen transverse mode and is then coupled into a single-mode fibre connected to detector D_1. Detection of this photon heralds the presence of a single-photon seed in the second crystal.

The signal photon is combined with the second pump arm and drives the SPS-PDC interaction in the second crystal, realizing the CPDC configuration analysed

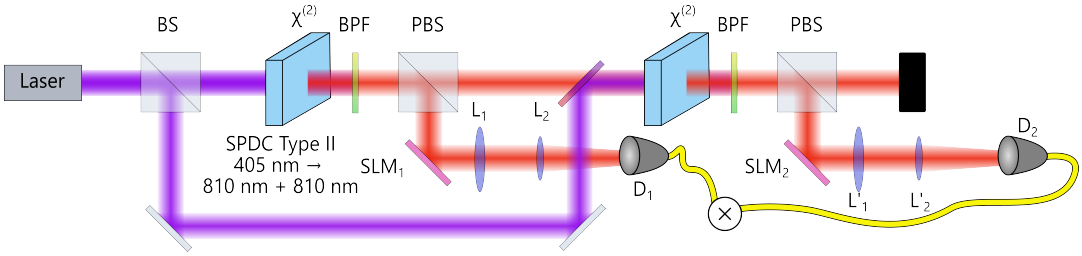


FIGURE 5.2: Proposed CPDC joint-idler measurement. A 405 nm pump is split to drive an SPDC stage (left) and an SPS-PDC/CPDC stage (right). Detection of the first idler photon heralds the presence of a single-photon seed in the second crystal. The two idler photons are analysed independently using spatial light modulators, single-mode fibres, and single-photon detectors D_1 and D_2. Coincidence counts between the two detection arms probe the joint-idler mean photon numbers predicted in Chapter 4.

in Chapter 4. A second spectral filter and polarizing beam splitter isolate the idler photon generated in this stage. Its transverse structure is analyzed using a second SLM and single-mode fibre connected to detector D_2. Coincidence detection between D_1 and D_2 therefore probes the joint-idler statistics of the cascaded process.

Let $\hat{n}_{1,m}$ denote the photon-number operator associated with the first idler projected onto transverse mode m on SLM 1, and $\hat{n}_{2,n}$ the corresponding operator for the second idler projected onto mode n on SLM 2. The CPDC theory predicts joint-idler mean photon numbers of the form

$$N_{mn}^{(i_1,i_2)} = \langle \hat{n}_{1,m}\, \hat{n}_{2,n} \rangle. \tag{5.15}$$

In the low-gain regime relevant here, the number of registered coincidences in modes (m, n) during an integration time T is approximately

$$C_{mn} \simeq R\,T\,\eta_1\eta_2\,N_{mn}^{(i_1,i_2)}, \tag{5.16}$$

where R is the effective pair-generation rate and $\eta_{1,2}$ are the overall detection efficiencies in the two arms. Up to the known proportionality factor $R\,T\,\eta_1\eta_2$, the measured coincidence matrix therefore samples the joint-idler mean photon numbers predicted by the CPDC model.

To connect Eq. (5.15) directly to the overlap structure used throughout this thesis, one may write the coincidence matrix as a sum of a background term and a phase-conjugated enhancement term,

$$N_{mn}^{(i_1,i_2)} = N_{mn}^{(\mathrm{bg})} + N_{mn}^{(\mathrm{pc})}, \tag{5.17}$$

where $N_{mn}^{(\mathrm{bg})}$ is the contribution from uncorrelated spontaneous emission in the second stage and $N_{mn}^{(\mathrm{pc})}$ contains the stimulated phase-conjugated correlations. In the LG basis, the same azimuthal selection rule that appears in Eq. (5.6) implies that $N_{mn}^{(\mathrm{pc})}$ exhibits a diagonal enhancement when the second idler is projected onto the phase-conjugate mode of the heralded seed. Operationally, this is the joint-idler analogue of the single-mode stimulated enhancement term $\delta_{\ell_i,-\ell_{\mathrm{se}}}|M|^2$.

Mapping C_{mn} over a restricted set of transverse modes would reveal the diagonal enhancement associated with the stimulated contribution and would provide a direct experimental signature of single-photon phase conjugated correlations, even in the

absence of a deterministic conjugated output field.

5.9 Summary and Outlook

This thesis examined the extent to which the phase-conjugation behaviour of stimulated parametric down-conversion survives when the seeding field is reduced from a classical beam to a single photon. In the classical regime, the dominance of stimulated emission ensures that the idler field is determined almost entirely by the product $E_p E_s^*$, producing high-fidelity phase conjugation and enabling practical wavefront reversal. This mechanism was shown to support deterministic turbulence mitigation in free-space channels [9, 10, 15].

When the seed contains only one photon, this dominance is fundamentally lost. The stimulated and spontaneous contributions to the nonlinear interaction remain comparable, as reflected by Eqs. (5.7)-(5.9) and concretely by the mode-resolved decomposition in Eq. (5.6). The idler cannot be isolated as a uniquely phase-conjugated field. Although phase-conjugated structure persists within quantum correlations and joint detection statistics, it does not manifest as a deterministic transformation acting on individual photons. This distinction follows directly from photon-number scaling and from the antiunitary nature of complex conjugation in quantum mechanics, rather than from experimental imperfections or mode-matching constraints.

These results establish a clear boundary between classical and quantum regimes of $\chi^{(2)}$-based phase conjugation. Deterministic wavefront reversal is a property of the classical limit, where mean-field descriptions apply and stimulated emission dominates. In the single-photon regime, phase conjugation can only appear conditionally, through higher-order correlations that do not support shot-by-shot correction of propagation-induced distortions. As a consequence, classical turbulence-mitigation strategies based on stimulated parametric down-conversion do not transfer directly to quantum communication protocols in which the probe itself carries quantum information.

At the same time, the analysis clarifies what remains possible. The classical Stim-PDC turbulence-correction mechanism demonstrated in [15] remains directly applicable to QKD schemes in which the turbulence-correcting probe is classical and only the information-bearing states are quantum, a family of protocols that does not require single-photon seeding. Cascaded parametric down-conversion also provides a practical means of isolating the stimulated contribution through heralding and joint-idler measurements, offering a controlled platform for studying single-photon phase-conjugated correlations. The proposed joint-idler experiments would directly test the separation between spontaneous and stimulated contributions and further illuminate the transition between classical and quantum behaviour.

More broadly, this work highlights the importance of distinguishing between field-level intuition and quantum-state transformations when extending classical nonlinear-optical concepts to the single-photon domain. Identifying mechanisms capable of reproducing phase conjugation under genuinely quantum conditions remains an open challenge and may require measurement-based strategies, tailored interactions, or hybrid classical-quantum architectures. Understanding the limits established here provides a necessary foundation for pursuing such approaches and for assessing the role of nonlinear optics in future quantum communication and information-processing schemes.

Appendix A

Related Coauthored Publications

A.1 Tailoring spatial modes produced by stimulated parametric down-conversion

Authors: A. A. Aguilar-Cardoso, C. Li, T. J. B. Luck, M. F. Ferrer-Garcia, J. Upham, J. S. Lundeen, and R. W. Boyd

Journal: Physical Review A **112**, 043541 (2025)

Status: Published.

Context

This work presents a theoretical and experimental investigation of spatial mode generation and control using StimPDC. The study analyzes how the spatial properties of the stimulated idler beam depend on the pump and seed beam characteristics, and demonstrates controlled generation of Laguerre-Gaussian, Hermite-Gaussian, and angular spatial modes. The results provide a general framework for engineering structured light via nonlinear optical interactions and inform several design choices adopted in subsequent StimPDC-based experiments discussed in this thesis.

Author Contributions

I participated in the conception of this work through regular group discussions on the theoretical modeling and experimental design, contributing to the direction of both the analytical framework and the measurement strategy. I assisted with the construction and alignment of the experimental setup and was involved in data collection during the experimental campaign. I also contributed to the technical refinement and editing of the manuscript. The primary theoretical development, experimental implementation, data acquisition, and analysis were performed by the lead author.

PHYSICAL REVIEW A **112**, 043541 (2025)

Tailoring spatial modes produced by stimulated parametric down-conversion

A. A. Aguilar-Cardoso,* C. Li, T. J. B. Luck, M. F. Ferrer-Garcia, and J. Upham
Department of Physics, University of Ottawa, 25 Templeton, Ottawa, Ontario K1N 6N5, Canada

J. S. Lundeen
Department of Physics, University of Ottawa, 25 Templeton, Ottawa, Ontario K1N 6N5, Canada, and National Research Council of Canada, 100 Sussex Drive, Ottawa, Ontario K1A 0R6, Canada

R. W. Boyd
Department of Physics, University of Ottawa, 25 Templeton, Ottawa, Ontario K1N 6N5, Canada, and Institute of Optics, University of Rochester, Rochester, New York 14627, USA

(Received 25 July 2025; accepted 6 October 2025; published 27 October 2025)

We theoretically study and experimentally demonstrate controlled generation of spatial modes of light via stimulated parametric down-conversion (StimPDC) by transferring the spatial structure of a pump beam to the stimulated idler beam. We show how the beam characteristics of the stimulated beam depend on both the pump and seed beam's characteristics, enabling experimental control over size and propagation behavior. We also show how to control and improve the fidelity of different spatial modes and demonstrate that the angular basis ensures uniform fidelity across modes generated with StimPDC.

DOI: 10.1103/g22l-cgr1

I. INTRODUCTION

Spatial modes of light, optical fields characterized by a transverse spatial distribution that is maintained during free-space propagation, has proven useful in a wide range of fields such as telecommunications [1,2], microscopy [3], and machine learning [4]. Typically, these structured optical fields are generated by linear optical methods, including digital holography using spatial light modulators (SLMs) [5], liquid-crystal-based q plates [6], and engineered metasurfaces [7]. Recently, there has been a growing interest in harnessing nonlinear optical (NLO) processes to generate and manipulate structured light. Unlike linear methods, NLO interactions enable *in situ* tailoring of spatial and spectral properties during propagation or frequency conversion, offering dynamic control and access to novel regimes of light–matter interaction [8,9].

A particularly promising NLO process for structured light generation is stimulated parametric down-conversion (StimPDC). In StimPDC, a nonlinear crystal is injected with a pump beam at frequency ω_p and a seed beam with frequency ω_s to produce a stimulated beam at frequency $\omega_i = \omega_p - \omega_s$. The spatial counterpart of this frequency relation, which is governed by the nonlinear phase-matching parameters, allows conditioning of the spatial structures of the stimulated beam on those of the pump and seed beams, as illustrated in Fig. 1. For instance, StimPDC can be tailored to produce an idler beam whose spatial structure is the phase conjugate of the seed beam [10,11], enabling a variety of applications such as the efficient generation and detection of quantum states [12–14] and information encoding [15]. Although not the focus of the current work, the polarization state of this simulated beam can be engineered through the optical properties of the nonlinear medium, allowing the generation of beams with spatially varying polarization [16].

While recent work has shown that the fidelity of structured light generated in the stimulated field is governed by the effective transverse overlap between the pump and seed beams [17], a comprehensive study that quantifies the fidelity of spatial mode generation via StimPDC and their longitudinal propagation is essential to assess its viability for the aforementioned advanced photonic applications. In this work we analyze the joint effect of the seed and pump beams' transverse structures and propagation properties on those of the generated stimulated beam. This paper is organized as follows. Section II presents a theoretical framework on how the seed and pump beams' spatial dimensions affect the stimulated beam's Rayleigh range, i.e., the field's propagation divergence. Section III evaluates fidelity between the target spatial mode and the output field generated through the nonlinear interaction. In Sec. IV we experimentally demonstrate the transfer of spatial structures in StimPDC and show that our theoretical predictions apply for a variety of spatial mode bases, such as Laguerre-Gauss (LG), Hermite-Gauss (HG), and angular (ANG) modes. We believe that these findings contribute to understanding the nonlinear optical methods for generating structured light and highlight the potential of StimPDC as a platform for high-fidelity mode transfer in optical communication systems.

 ©2025 American Physical Society

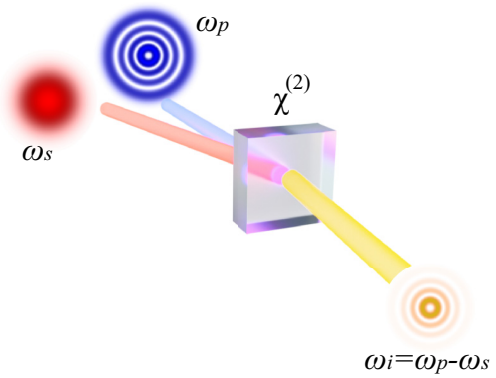


FIG. 1. Illustration of structured light generation using StimPDC. A structured pump beam at frequency ω_p interacts with a seed beam at ω_s, stimulating the emission of an idler beam at $\omega_i = \omega_p - \omega_s$ that inherits the spatial structure of the pump.

II. TAILORING STIMPDC

We assume that the seed beam is sufficiently strong such that the contribution from spontaneous parametric down-conversion (SPDC) is negligible compared to that of the StimPDC. This allows modeling of the interaction within the classical regime of nonlinear optics [18]. In addition, we consider that the nonlinear interaction between the complex field of the pump beam U_p and the seed beam U_s occurs within a nonlinear crystal whose thickness L is much smaller than the Rayleigh range of the incident beams, z_{Rp} and z_{Rs}. This thin-crystal approximation allows us to disregard the propagation effects induced within the nonlinear medium, reducing the interaction to a phase-matching condition applied at a single transverse plane. Under this framework it is possible to approximately describe the spatial profile of the generated stimulated beam U_i as [19]

$$U_i(r) \propto U_p(r,0)U_s^*(r,0), \tag{1}$$

where the subscripts p, s, and i identify the pump, seed, and stimulated beams, respectively, and r is the transverse spatial coordinates of the field.

The simulated beam generated from nonlinear interactions have free-space propagation properties that differ significantly from both the pump and seed beams. To describe this effect, let us consider that both the pump and the seed beams have a Gaussian profile with waist parameters $w_p \neq w_s$ at the center of the nonlinear crystal. The normalized complex amplitude of a Gaussian beam in cylindrical coordinates (r, ϕ, z) is given by

$$U(r,z) = \frac{U_0}{w(z)} e^{-\frac{r^2}{w^2(z)}} e^{i\left(\frac{kr^2}{2R(z)} - \Phi(z)\right)}, \tag{2}$$

where z is the central propagation direction of the beam, $\Phi(z)$ and $R(z)$ are the Gouy phase and radius of curvature of the wave front at z, $k = 2\pi/\lambda$ is the wave number, and λ is the wavelength of interest [20]. The beam waist evolves along propagation according to $w(z) = w_0\sqrt{1 + (\frac{z}{z_R})^2}$, where w_0 is the beam waist at the plane $z = 0$ and $z_R = \frac{\pi w_0^2}{\lambda}$ is the Rayleigh range. Therefore, by substituting Eq. (2) for both pump and seed beams in Eq. (1), it is straightforward to show that the beam waist parameters of the pump w_p, seed w_s, and stimulated beam w_i are related by

$$\frac{w_i}{w_s} = \frac{1}{\sqrt{1+\gamma_{sp}^2}}, \tag{3a}$$

$$\frac{w_i}{w_p} = \frac{1}{\sqrt{1+\frac{1}{\gamma_{sp}^2}}}, \tag{3b}$$

where we have defined $\gamma_{sp} = w_s/w_p$. As shown in Eqs. (3), the beam waist of the output beam w_i solely depends on the ratio of the waists of the pump and seed beams. Figure 2 depicts the effect of varying γ_{sp} when fixing the ratio between wavelengths of the pump and seed beams. For example, when $\gamma_{sp} \ll 1$, the pump field appears relatively constant over the transverse profile of the seed beam, which results in $w_i \approx w_s$. On the other hand, as the value of γ_{sp} increases, w_i

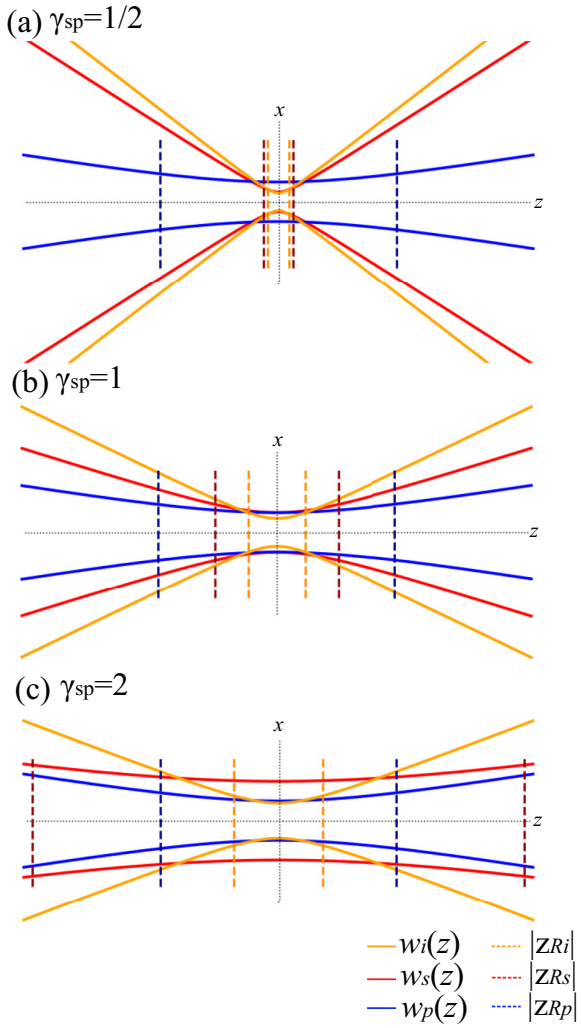


FIG. 2. Beam waist propagation of pump beam at $\lambda_p = 405$ nm (blue), seed beam at $\lambda_s = 780$ nm (red), and stimulated beam at $\lambda_i = 842$ nm (orange) for (a) $\gamma_{sp} = 1/2$, (b) $\gamma_{sp} = 1$, and (c) $\gamma_{sp} = 2$. As γ_{sp} increases, the stimulated beam waist w_s approaches that of the pump beam w_p, while its Rayleigh range converges to approximately half of the pump beam's Rayleigh range.

asymptotically approaches w_p. Finally, for $\gamma_{sp} = 1$, where both pump and seed beams have equal waists, the waist of the stimulated beam yields $w_i = w_{p,s}/\sqrt{2}$. Intuitively, one can understand the above behavior by treating the waist ratio γ_{sp} as a metric for describing the effective nonlinear interaction region.

Using these results for the waist of the output beam, we proceed to analyze the propagation of the output beam. It is possible to write the Rayleigh range of the stimulated beam in terms of the ratios,

$$\frac{z_{Ri}}{z_{Rs}} = \left(\frac{\lambda_s}{\lambda_p} - 1\right)\left(\frac{1}{1+\gamma_{sp}^2}\right), \tag{4a}$$

$$\frac{z_{Ri}}{z_{Rp}} = \left(1 - \frac{\lambda_p}{\lambda_s}\right)\left(\frac{1}{1+\frac{1}{\gamma_{sp}^2}}\right), \tag{4b}$$

where $\lambda_p < \lambda_s$. Notice that the Rayleigh range of the stimulated beam depends exclusively on the waist ratio γ_{sp} and the wavelength ratio λ_s/λ_p of the seed and pump beams. As depicted in Fig. 2(a), for very small values of γ_{sp}, z_{Ri} becomes comparable to that of the seed. Meanwhile, as depicted in Figs. 2(b) and 2(c), z_{Ri} becomes smaller than z_{Rp} for larger values of γ_{sp}, where the maximum value of $z_{Ri} = z_{Rp}/2$ is achieved for the particular case of degenerate StimPDC ($\lambda_s = \lambda_i$). The wavelength ratio λ_s/λ_p provides an additional degree of control over the stimulated beam, as long as the phase-matching conditions of the nonlinear crystal are fulfilled [19].

Before moving forward, it is important to highlight that these results offer a comprehensive and broadly applicable framework for the design of StimPDC-based light structuring systems.

III. TRANSFERRING SPATIAL MODES WITH STIMPDC

Although our analysis has only considered seed and pump beams with Gaussian profiles, we note that all previously discussed results regarding beam waist and divergence remain valid for any solution of the paraxial wave equation.

To analyze the generation of more complex spatial modes, it is necessary to define a measure that quantifies the spatial mode transfer from the pump beam to the stimulated idler beam. Therefore, we analytically calculate the fidelity,

$$F(\gamma_{sp}) = \frac{\left|\int U_p^*(\mathbf{r}) U_i(\mathbf{r}) d\mathbf{r}\right|^2}{\int U_p^*(\mathbf{r}) U_p(\mathbf{r}) d\mathbf{r} \int U_i^*(\mathbf{r}) U_i(\mathbf{r}) d\mathbf{r}}, \tag{5}$$

for different spatial modes on the pump beam $U_p(\mathbf{r})$ and the resulting spatial mode on the stimulated field $U_i(\mathbf{r})$ while keeping a Gaussian profile for the seed beam $U_s(\mathbf{r})$.

Equation (5) defines fidelity as the overlap between the idler field $U_i(\mathbf{r})$, given by Eq. (1) with beam waist w_i (as defined in the previous section), and the pump field $U_p(\mathbf{r})$ with beam waist w_p. We adopt this particular definition to study mode transfer from pump to idler via StimPDC. Under this definition, F=1 corresponds to complete overlap of the spatial profiles of the pump and stimulated beams, meaning the pump's spatial mode is perfectly transferred to the idler. Alternatively, fidelity may be defined as the overlap between the idler mode and a target spatial mode (e.g., the theoretical profile of an LG mode), also with beam waist w_i, or any other chosen beam waist that differs from w_p. However, this lies beyond the scope of the present work.

We start by considering the case that $U_p(\mathbf{r})$ is in an LG mode. The normalized complex amplitude of an LG beam in cylindrical coordinates (r, θ, z) is written as [20]

$$\mathrm{LG}_q^l(r,z) = \frac{\mathcal{N}}{w(z)}\left(\frac{\sqrt{2}r}{w(z)}\right)^{|\ell|} L_q^{|\ell|}\left(\frac{2r^2}{w^2(z)}\right) \times e^{-\frac{r^2}{w^2(z)}} e^{i\left(\ell\theta + \frac{kr^2}{2R(z)} - \Phi(z)\right)}, \tag{6}$$

where $L_q^{|\ell|}(\cdot)$ represents the generalized Laguerre polynomial, and the functions $R(z)$, $\Phi(z)$, and $w(z)$ retain the same definitions as in Eq. (2). The azimuthal index ℓ, which is also referred to as topological charge, determines the number and direction of 2π phase cycles around the optical axis. The radial index q indicates that the transverse intensity profile contains $q+1$ concentric rings. Therefore, by substituting Eq. (6) into Eq. (5), we calculate the fidelity as

$$F_{l,q}(\gamma_{sp}) = \frac{\left(\int_0^\infty e^{-\frac{u}{2\gamma_{sp}^2}} e^{-u} u^{|l|} [L_q^{|l|}(u)]^2 du\right)^2}{\int_0^\infty e^{-u} u^{|l|} [L_q^{|l|}(u)]^2 du \int_0^\infty e^{-\frac{u}{\gamma_{sp}^2}} e^{-u} u^{|l|} [L_q^{|l|}(u)]^2 du}, \tag{7}$$

where $u = 2r^2/w_p^2$, and the definition $\gamma_{sp} = w_s/w_p$ still holds for any spatial mode. Figure 3 shows the solutions of the fidelity integral, given by Eq. (7), for different modal numbers. Note that for a fixed value of the beam waist defined in Eq. (6), the size of the transverse spatial profile increases with modal numbers. Consequently, the overlap between the LG structure and the seed beam becomes progressively smaller for higher-order beams. This results in a decrease in the fidelity of the stimulated beam as l and q increases. This occurs because at large γ_{sp}, the effective interaction region is much smaller than the mode profile of the seed beam, such that the wave front of the seed beam approximates that of a plane wave. As a result, the stimulated field completely inherits the structure of the pump field. This behavior is also evident in Eq. (1), where as the seed beam waist approaches infinity, the seed field's spatial structure becomes indiscernible in the nonlinear interaction region, resulting in $U_i(r) \propto U_p(r, 0)$. Similarly, we consider the case of a pump beam described by an HG mode. The normalized amplitude of an HG beam is written as [20]

$$\mathrm{HG}_{n_x,n_y}(r,z) = \frac{\mathcal{N}}{w(z)} H_{n_x}\left(\frac{\sqrt{2}x}{w(z)}\right) H_{n_y}\left(\frac{\sqrt{2}y}{w(z)}\right) \times e^{-\frac{r^2}{w^2(z)}} e^{i\left(\frac{kr^2}{2R(z)} - \Phi(z)\right)}, \tag{8}$$

where $r^2 = x^2 + y^2$. $H_m(\cdot)$ is the generalized Hermite polynomials of index m, and the functions $R(z)$, $\Phi(z)$, and $w(z)$ retain the same definitions as in Eq. (2). Their transverse intensity consists of $(n_x+1)(n_y+1)$ bright lobes arranged in a rectangular grid, with nodal lines separating adjacent regions along the horizontal and vertical axes. Since the expression for an HG mode can be factorized into a product of its orthogonal

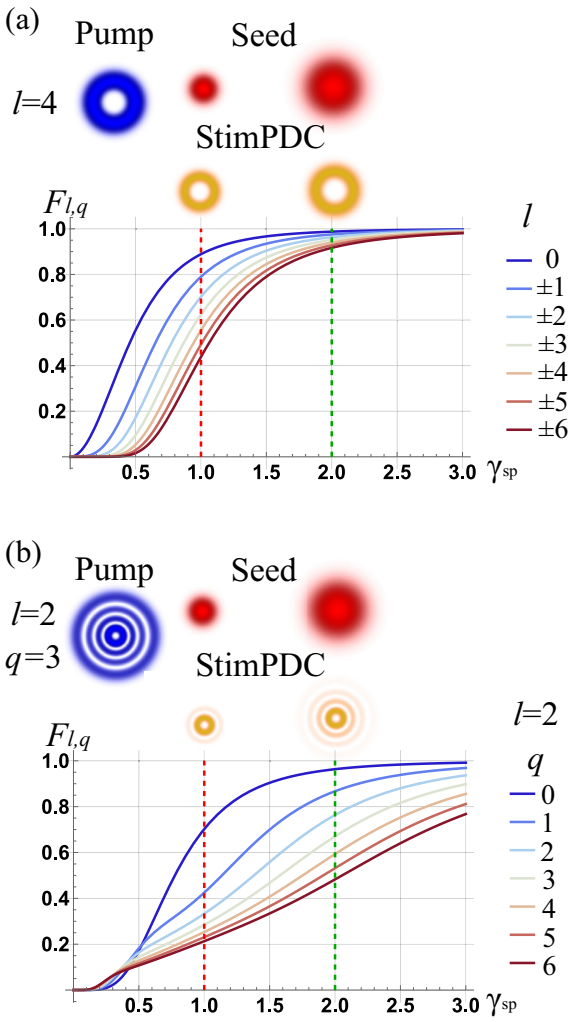


FIG. 3. Fidelity plots of stimulated beams calculated using Eq. (7) for different modal numbers as function of γ_{sp}: (a) OAM beams ($q = 0$) for $l \in [-6, 6]$, and (b) LG beams with $l = 2$ and $q \in [0, 6]$. The insets show examples of the transverse intensity profiles for both cases.

transverse components, we can write the fidelity as

$$F_{n_x,n_y}(\gamma_{sp}) = F_{n_x}(\gamma_{sp})F_{n_y}(\gamma_{sp}), \tag{9}$$

where $F_{n_{x(y)}}(\gamma_{sp})$ denotes the fidelity calculated for the $x(y)$ components and is explicitly written as

$$F_{n_j}(\gamma_{sp}) = \frac{\left(\int_{-\infty}^{\infty} e^{-\frac{u^2}{2\gamma_{sp}^2}} e^{-u^2}[H_{n_j}(u)]^2 du\right)^2}{\int_{-\infty}^{\infty} e^{-u^2}[H_{n_j}(u)]^2 du \int_{-\infty}^{\infty} e^{-\frac{u^2}{\gamma_{sp}^2}} e^{-u^2}[H_{n_j}(u)]^2 du}. \tag{10}$$

Figure 4(b) shows the fidelity values for HG modes of different modal numbers. We notice a similar behavior to the case of LG modes. Since the number of lobes increases with the modal numbers, the overlap between the HG structure and the seed beam becomes progressively smaller for higher-order beams. This results in a decrease in the fidelity of the generated beam.

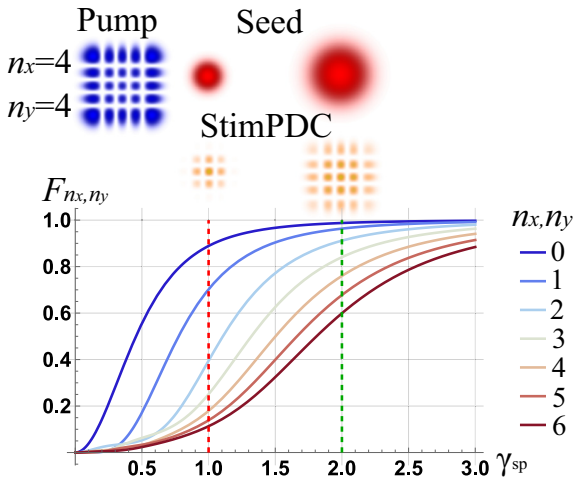


FIG. 4. Fidelity plots of stimulated beams calculated using Eq. (9) for HG beams with $n_x = n_y \in [0, 6]$ as function of γ_{sp}. The insets show examples of the transverse intensity profiles.

Both the LG and HG modes display a dependence of the fidelity on the mode number of the constituent basis functions due to the radial dependence of the transverse field, which bottlenecks the mode capacity in diffraction-limited systems. Nevertheless, it is possible to address this by defining an orthogonal basis in which the spatial modes depend only on the azimuthal coordinate. One such implementation is a basis formed by the angular (ANG) modes, which is named after their angularly varying intensity distribution. The ANG modes are written as

$$U_j(r) = \frac{1}{\sqrt{d}} \sum_{l=-L}^{L} \mathrm{LG}_0^l(\mathbf{r}) e^{-i2\pi \frac{jl}{d}},$$
$$L = \begin{cases} d/2, & \text{if } d \text{ is even} \\ (d-1)/2, & \text{if } d \text{ is odd} \end{cases} \tag{11}$$

where d determines the number of bright lobes azimuthally distributed around the optical axis, and the modal number j determines the azimuthal location of the intensity maxima. When d is even, the term with $l = 0$ is excluded from the sum in Eq. (11) to ensure a balanced superposition of OAM modes. The ANG modes form a mutually unbiased basis with the OAM basis [21]. We calculate the fidelity [Eq. (5)] of transferring an ANG mode from the pump to the stimulated field using

$$F_d(\gamma_{sp}) = \frac{\left(\sum_l \int_0^{\infty} e^{-\frac{u}{2\gamma_{sp}^2}} e^{-u} u^{|l|}[L_0^{|l|}(u)]^2 du\right)^2}{\sum_{l,l'} \int_0^{\infty} e^{-u} u^{|l|}[L_0^{|l|}(u)]^2 du \int_0^{\infty} e^{-\frac{u}{\gamma_{sp}^2}} e^{-u} u^{|l'|}[L_0^{|l'|}(u)]^2 du}. \tag{12}$$

Figure 5 shows the fidelity values for transferring ANG modes with different dimensions and modal numbers. Here, fidelity does not depend on the modal number j but rather solely on the dimensionality of the basis d. The fidelity decreases as the dimensionality of the basis increases. This is because a larger dimensionality would require higher values of l in Eq. (11), which increases the size of the transverse

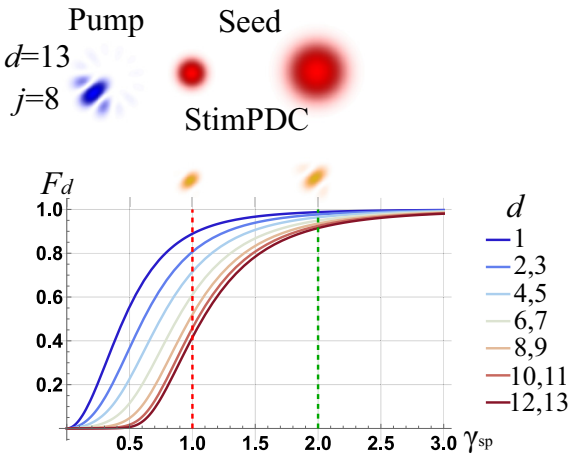


FIG. 5. Fidelity plots of stimulated beams calculated using Eq. (12) for ANG beams with $d \in [1, 13]$ as function of γ_{sp}. It is worth noting that fidelity decreases as the dimensionality increases. For even values of d, the $l = 0$ component is excluded, resulting in modes with the same transverse area as those corresponding to the adjacent odd dimension $d + 1$, which includes the $l = 0$ term, because aside from this additional Gaussian component, both sets of modes are composed of the same l contributions, which makes both of them have the same fidelity. The insets show examples of the transverse intensity profiles.

spatial distribution for each basis element, thus decreasing the overlap between the seed beam and the pump ANG modes. However, for a fixed dimension, all the basis elements are composed of the same OAM modes, while what changes is the intermodal complex phase of the superposition. Therefore, the size of the transverse spatial distribution remains the same for different modal numbers. As a result, every element within the same basis will have homogenized fidelity as a function of γ_{sp}.

This analysis remains applicable when the seed beam carries the complex spatial structure of interest while the pump beam remains Gaussian. In this specific case, the stimulated beam corresponds to the complex conjugate of the seed beam's spatial profile as seen in Eq. (1).

IV. EXPERIMENTS AND DISCUSSION

A. Experimental setup

We experimentally validate our theoretical predictions using the setup depicted in Fig. 6. A continuous-wave pump laser ($\lambda_p = 405$ nm, power $= 20$ mW) is collimated using lenses $f_1 = 250$ mm and $f_2 = 500$ mm. A spatial light modulator encodes the laser beam with a desired spatial structure. After SLM, the pump beam retains 2mW of power. The structured pump beam is then imaged with lenses $f_3 = 500$ mm and $f_4 = 250$ mm onto a 2-mm-long BBO crystal cut for type-II phase-matching. The seed laser ($\lambda_s = 780$ nm, power $= 20$ mW) is aligned at 4° with respect to the pumping beam, and its beam waist at the crystal plane is adjusted by changing f_5 and f_6 to obtain different γ_{sp} measurements. The polarizations of the beams are controlled using half-wave plates (HWPs) such that the two beams have orthogonal

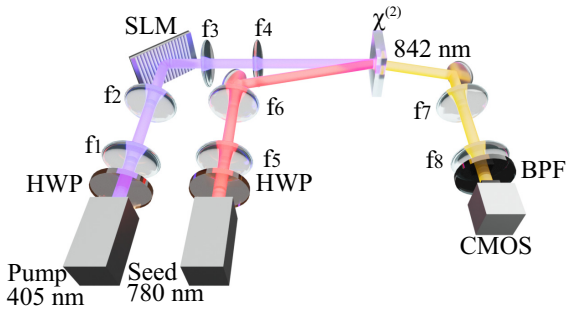


FIG. 6. A collimated 405-nm beam is directed onto the SLM to generate the desired spatial modes, which are then imaged onto the nonlinear crystal $\chi^{(2)}$ to serve as the pump. A Gaussian beam at 780 nm is seeded to stimulate the PDC process and its beam waist is varied. We achieve optimal phase-matching by tuning the polarizations input beams using HWPs. Finally, the stimulated beam is imaged onto a CMOS camera to capture its intensity. The CMOS camera is translated along the optical axis to record the beam intensity at different propagation distances.

polarizations with respect to each other. The idler beam ($\lambda_i =$ 842 nm) is directed onto a complementary metal-oxide semiconductor (CMOS) camera (pixel size 3.45 μm × 3.45 μm) using two lenses with focal lengths $f_7 = f_8 = 250$ mm. The camera is equipped with a bandpass filter centered at 840 nm with a 20-nm bandwidth.

B. Tailoring beam properties

As a first step, we demonstrate experimental control over the spatial features of the stimulated beam by varying γ_{sp}. The desired waist parameter of the pump beam is imposed by generating a fundamental Gaussian mode using the SLM. To estimate w_p, w_s, and w_i, we fit Eq. (2) to the intensity profile captured in the crystal plane. By varying $\gamma_{sp} = w_s/w_p$, we can compare experimentally measured w_i/w_p and w_i/w_s with Eqs. 3(b) and 3(a). We performed this procedure for $\gamma_{sp} \in [0.5, 3]$ with a 0.5 step size. These results are shown in Fig. 7(a).

If the waists of the pump and seed beam are equal ($\gamma_{sp} = 1$), the stimulated beam will be $2^{-1/2}$ times the waist of the incoming beam, resulting in a difference in the waist of the beam of approximately 30%, effectively truncating the spatial information of both input beams. However, if the beam waist of the seed increases compared to that of the pump ($\gamma_{sp} > 1$), the energy interaction area between the pump and the seed beam will increase. As a result, the waist of the stimulated beam asymptotically converges to that of the pump beam. For instance, expanding the seed beam waist to twice the pump beam waist ($\gamma_{sp} = 2$) reduces the size difference to 10%.

By shifting the camera along the optical axis in a range of 85 cm, we measure the evolution of the transverse profile during free-space propagation. By setting $w_p = 300$ μm and changing γ_{sp} from 1 to 2, we calculate that the Rayleigh range of the stimulated beam [Eqs. (4)] changes from 0.17 m to 1.06 m. Figure 7(b) compares the experimentally measured beam widths at different propagation distances with $w(z) = w_0\sqrt{1 + (\frac{z}{z_R})^2}$ evaluated for the specified Rayleigh

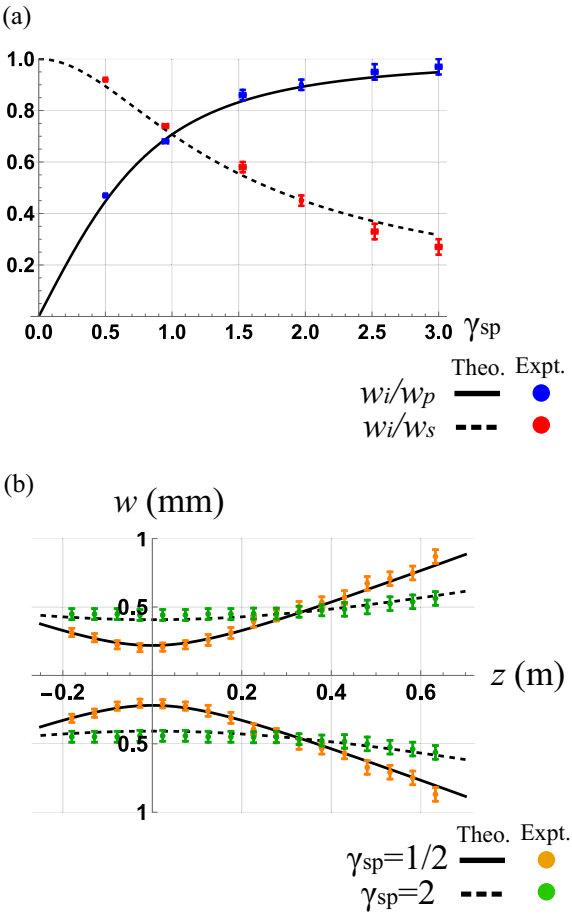


FIG. 7. Theoretical and experimental comparison of: (a) w_i/w_p and w_i/w_s given by Eqs. (3). Here the pump and seed beams are Gaussian beams with waist at $w_p = 300$ μm and the seed beam waist w_s is varied from $w_s = 150$ μm to $w_s = 900$ μm. (b) The beam waist profile over a propagation of 85 cm to show the tuning on the Rayleigh range of the stimulated beam given in Eq. (4). Here we change γ_{sp} by setting the seed beam waist at $w_p = 300$ μm (orange plot) and $w_p = 600$ μm (green plot). The error bars are given by the fit algorithm.

range values. Our results exhibit consistency between theory and experiment.

C. Improving fidelity of spatial modes

In free-space optical communication, it is important to retain a near-uniform fidelity across the utilized spatial modes without resorting to beams with excessive size contrast or compromising the thin-crystal approximation. Here we identify the optimal choice of technical parameter (specifically, γ_{sp}) and spatial mode basis by comparing the corresponding fidelity values measured in experiments.

To experimentally measure the fidelities, we recall that, in general, the inequality $|\int U_p^*(\mathbf{r})U_i(\mathbf{r})d\mathbf{r}| \leqslant \int |U_p^*(\mathbf{r})||U_i(\mathbf{r})|d\mathbf{r}$ holds, and equality is achieved only when the integrand is real and maintains the same sign over the entire integration domain, representing the upper-bound case. In our fidelity calculations for LG, HG, and ANG modes, the

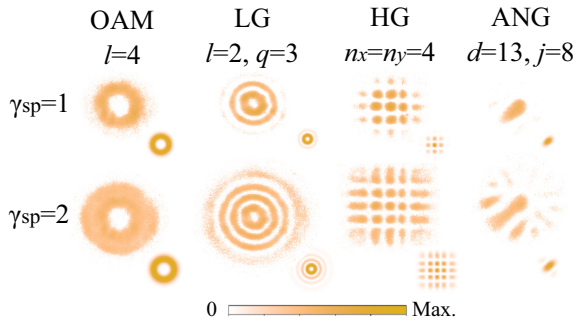


FIG. 8. Normalized intensity captures of the stimulated beam for $\gamma_{sp} = 1$ and $\gamma_{sp} = 2$ for different modes. The inset figures beneath each capture display the theoretical normalized intensity profiles derived in the preceding section.

functions $U_p^*(\mathbf{r})U_i(\mathbf{r})$ are always real and positive, as can be explicitly seen in the integrands of Eqs. (7), (10), and (12). This occurs since we are using the thin-crystal approximation and considering the pump has the beam waist at the crystal plane, which makes our fidelity calculations correspond to the upper-bound case. Consequentially, in our limiting case, the fidelity defined in Eq. (5) can be directly evaluated from the intensity distributions of the pump and stimulated fields at the crystal plane, since $|\int U_p^*(\mathbf{r})U_i(\mathbf{r})d\mathbf{r}| = \int \sqrt{I_p(\mathbf{r})}\sqrt{I_i(\mathbf{r})}d\mathbf{r}$. Therefore, the variations in the intensity profiles are the only source of mode mismatch, thereby simplifying the experimental measurements. Finally, in the numerical approximation $\int d\mathbf{r} \to \sum_{x,y} \Delta x \Delta y$, where Δx and Δy are the discrete sampling steps, we can estimate the fidelity as

$$F = \frac{\left(\sum_{x,y} \sqrt{I_p(x,y)I_i(x,y)}\right)^2}{\sum_{x,y} I_p(x,y) \sum_{x,y} I_i(x,y)}, \tag{13}$$

where $I_{p,i}(x,y) = |U_{p,i}(x,y)|^2$. Figure 8 shows examples of experimental normalized intensity captures for different modes, and Fig. 9 shows the average fidelity values, expressed as percentages, obtained for each mode base.

For LG and HG bases, decreasing γ_{sp} causes the transfer fidelity to reduce more at higher mode orders. This effect could reduce the effective spatial dimensionality and restrict the information capacity of StimPDC devices. As shown in Fig. 9(a), with a decreased γ_{sp} from 2 to 1, LG modes with dimensionality $d = 13$ ($q = 0$ and $l \in [-6, 6]$) would display a reduced average fidelity with an increased variation, from 93% ± 1% to 57% ± 19%. Similar results are seen for beams in LG modes with different radial indices ($l = 2$ and $q \in [0, 6]$) and HG modes with different mode indices ($n_x = n_y \in [0, 6]$), as depicted in Figs. 9(b) and 9(c), respectively. Although ANG modes experience a reduced average fidelity from 82% to 34%, as shown in Fig. 9(d), they retain a fidelity consistency of ±1% across all mode orders. The discrepancy between the experimental and theoretical fidelities of the ANG modes may be attributed to imperfections in the phase masks used for their generation. Nevertheless, we show that when multiple modes are employed, ANG modes exhibit greater consistency across the basis, whereas LG and HG modes display mode-dependent variations in fidelity.

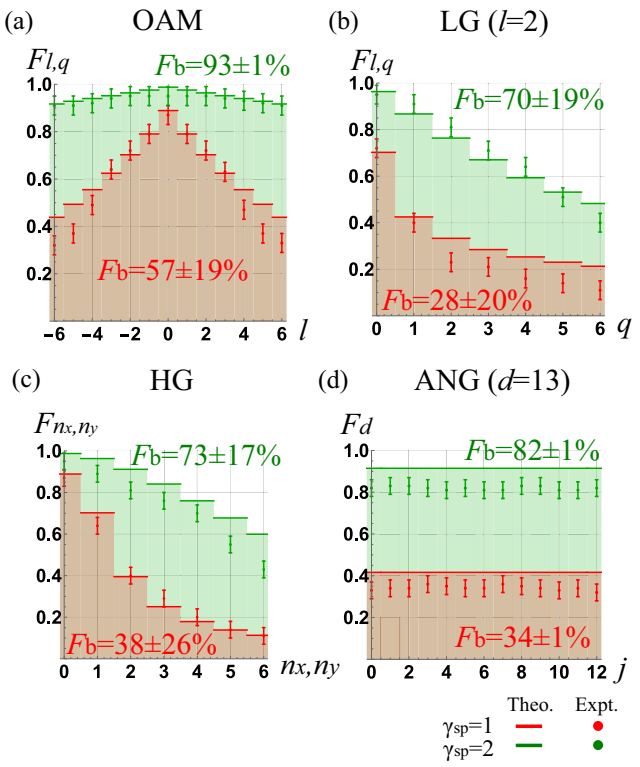


FIG. 9. Theoretical and experimental comparison of fidelity for the spatial modes: (a) OAM ($q = 0$) for $l \in [-6, 6]$, (b) LG with fixed $l = 2$ and with $q \in [0, 6]$, (c) HG basis for $n_x = n_y \in [0, 6]$, and (d) ANG basis with $d = 13$. The error bars are given by the signal-to-noise ratio of the CMOS captures.

This feature makes ANG modes particularly advantageous for applications such as free-space quantum key distribution [22,23], where encoding and transmitting information evenly across spatial modes is crucial.

With γ_{sp} increased from 1 to 2, the average mode fidelity in all bases improved. This result agrees with our theoretical predictions and has significant implications for practical applications using StimPDC. Since maintaining information transfer fidelity via StimPDC requires increasingly large γ_{sp} at higher mode orders, one needs to either make the seed beam waist increasingly large or make the pump beam waist diminishingly small. However, the commercially available nonlinear crystals typically have clear apertures of a few millimeters, making it impractical to use large seed beams without inducing diffraction effects. On the other hand, reducing the beam waist of the pump decreases its Rayleigh length and could invalidate the thin-crystal approximation. In this case, the nonlinear propagation effects could become prominent and introduce distortion to the stimulated beam.

V. CONCLUSIONS

We present a comprehensive study on the transfer of transverse spatial structure and longitudinal propagation properties in StimPDC. Specifically, we theoretically and experimentally investigate the dependence of the Rayleigh range and mode fidelity of the stimulated beam on the wavelength, beam waist, and Rayleigh range of the pump and seed beams. We demonstrate this dependence by showcasing the transfer of LG, HG, and ANG modes in StimPDC. Our results show that while the transfer fidelity of ANG modes depends solely on the ratio of the beam waists of both input beams ($\gamma_{sp} = \frac{w_s}{w_p}$), that of LG and HG modes is also influenced by the mode order. Therefore, the fidelity of mode transfer in StimPDC can be optimized by both tuning the input beam parameters and choosing an ideal spatial mode basis. Following this principle, we successfully transferred complex spatial structures in LG, HG and ANG modes from the pump beam to the stimulated output beam with high fidelities.

Our work provides technical guidance for controlling structured light using nonlinear optical methods and has significant implications for implementing StimPDC for free-space optical communication applications. For instance, since the ANG basis maintains a nearly constant fidelity across all mode orders, it could be preferred for ensuring intermodal information consistency. Although our experiments were conducted using fixed wavelengths, our theoretical model applies to StimPDC using pump and seed beams with arbitrary phase-matched wavelengths. This capability could enable control of the spatial structures of optical beams with spectral tuning. These findings advance structured light manipulation in nonlinear optics and underscore the potential of StimPDC for high-fidelity mode transfer in optical communication systems.

DATA AVAILABILITY

The data that support the findings of this article are not publicly available upon publication because it is not technically feasible and/or the cost of preparing, depositing, and hosting the data would be prohibitive within the terms of this research project. The data are available from the authors upon reasonable request.

[1] F. Bouchard, K. Heshami, D. England, R. Fickler, R. W. Boyd, B. Englert, L. L. Sánchez-Soto, and E. Karimi, Experimental investigation of high-dimensional quantum key distribution protocols with twisted photons, Quantum **2**, 111 (2018).

[2] A. Klug, C. Peters, and A. Forbes, Robust structured light in atmospheric turbulence, Adv. Photonics **5**, 016006 (2023).

[3] K. K. M. Bearne, Y. Zhou, B. Braverman, J. Yang, S. A. Wadood, A. N. Jordan, A. N. Vamivakas, Z. Shi, and R. W. Boyd, Confocal super-resolution microscopy based on a spatial mode sorter, Opt. Express **29**, 11784 (2021).

[4] X. Fang, X. Hu, B. Li, H. Su, K. Cheng, H. Luan, and M. Gu, Orbital angular momentum-mediated machine learning for high-accuracy mode-feature encoding, Light. Sci. Appl. **13**, 49 (2024).

[5] C. Rosales-Guzmán and A. Forbes, *Structured Light with Spatial Light Modulators* (Society of Photo-Optical Instrumentation Engineers, SPIE, 2017).

[6] A. Rubano, F. Cardano, B. Piccirillo, and L. Marrucci, *Q*-plate technology: a progress review, J. Opt. Soc. Am. B **36**, D70 (2019).

[7] A. H. Dorrah and F. Capasso, Tunable structured light with flat optics, Science **376**, eabi6860 (2022).

[8] W. T. Buono and A. Forbes, Nonlinear optics with structured light, Opto-Electron. Adv. **5**, 210174 (2022).

[9] W. M. Jones and M. A. Reber, Ultrafast structured light through nonlinear frequency generation in an optical enhancement cavity, Opt. Lett. **49**, 4999 (2024).

[10] A. G. de Oliveira, M. F. Z. Arruda, W. C. Soares, S. P. Walborn, R. M. Gomes, R. M. de Araújo, and P. H. S. Ribeiro, Real-time phase conjugation of vector vortex beams, ACS Photonics **7**, 249 (2020).

[11] G. H. dos Santos, A. G. de Oliveira, N. R. da Silva, G. Cañas, E. S. Gómez, S. Joshi, Y. Ismail, P. H. S. Ribeiro, and S. P. Walborn, Phase conjugation of twisted Gaussian Schell model beams in stimulated down-conversion, Nanophotonics **11**, 763 (2022).

[12] M. Liscidini and J. E. Sipe, Stimulated emission tomography, Phys. Rev. Lett. **111**, 193602 (2013).

[13] J. Fadrný, M. Neset, M. Bielak, M. Ježek, J. Bílek, and J. Fiurášek, Experimental preparation of multiphoton-added coherent states of light, npj Quantum Inf. **10**, 89 (2024).

[14] Y. Xu, S. Choudhary, and R. W. Boyd, Stimulated emission tomography for efficient characterization of spatial entanglement, Phys. Rev. Res. **6**, L042047 (2024).

[15] Y. Xu, S. Tang, A. N. Black, and R. W. Boyd, Orthogonal spatial coding with stimulated parametric down-conversion, Opt. Express **31**, 42723 (2023).

[16] A. de Oliveira, N. R. da Silva, R. M. de Araújo, P. H. Souto Ribeiro, and S. P. Walborn, Quantum optical description of phase conjugation of vector vortex beams in stimulated parametric down-conversion, Phys. Rev. Appl. **14**, 024048 (2020).

[17] S. Singh, I. Nape, and A. Forbes, Enhanced fidelity in nonlinear structured light by virtual light-based apertures, Opt. Express **33**, 27615 (2025).

[18] M. F. Z. Arruda, W. C. Soares, S. P. Walborn, D. S. Tasca, A. Kanaan, R. M. de Araújo, and P. H. S. Ribeiro, Klyshko's advanced-wave picture in stimulated parametric down-conversion with a spatially structured pump beam, Phys. Rev. A **98**, 023850 (2018).

[19] R. W. Boyd, *Nonlinear Optics* (Academic Press, New York, 2020).

[20] B. E. A. Saleh and M. C. Teich, *Fundamental Photonics* (John Wiley & Sons, New York, 1991).

[21] M. Mirhosseini, O. S. Magaña-Loaiza, M. N. O'Sullivan, B. Rodenburg, M. Malik, M. P. J. Lavery, M. J. Padgett, D. J. Gauthier, and R. W. Boyd, High-dimensional quantum cryptography with twisted light, New J. Phys. **17**, 033033 (2015).

[22] M. Mafu, A. Dudley, S. Goyal, D. Giovannini, M. McLaren, M. J. Padgett, T. Konrad, F. Petruccione, N. Lutkenhaus, and A. Forbes, Higher-dimensional orbital-angular-momentum-based quantum key distribution with mutually unbiased bases, Phys. Rev. A **88**, 032305 (2013).

[23] L. Scarfe, F. Hufnagel, M. F. Ferrer-Garcia, A. D' Errico, K. Heshami, and E. Karimi, Fast adaptive optics for high-dimensional quantum communications in turbulent channels, Commun. Phys. **8**, 79 (2025).

A.2 All-optical turbulence mitigation for free-space quantum key distribution using stimulated parametric down-conversion

Authors: A. A. Aguilar-Cardoso, C. Li, T. J. B. Luck, M. F. Ferrer-Garcia, J. Upham, J. S. Lundeen, and R. W. Boyd

Journal: Optica **13**, 386-394 2025.

Status: Published.

Context

This work proposes and demonstrates an all-optical scheme for mitigating atmospheric turbulence in free-space quantum key distribution by exploiting the phase-conjugation properties of StimPDC. The study combines theoretical modeling, numerical simulations, and a proof-of-principle experiment to show that turbulence-induced modal crosstalk can be reduced below the security threshold for high-dimensional QKD protocols. While the results are closely related to the broader theme of StimPDC-based spatial-mode manipulation discussed in this thesis, this publication represents a collaborative effort with a distinct scientific focus on quantum communication through turbulent channels.

Author Contributions

I contributed to the conception of this work through group discussions on the experimental design, numerical simulation strategy, and interpretation of results. I assisted with aspects of the experimental setup and participated in preliminary measurements. I also contributed to the technical refinement and editing of the manuscript. The primary conceptual development, theoretical modeling, experimental execution, and data analysis were carried out by the lead author.

386 Vol. 13, No. 3 / March 2026 / Optica Research Article

OPTICA

All-optical turbulence mitigation for free-space quantum key distribution using stimulated parametric down-conversion

Aarón A. Aguilar-Cardoso,[1,*] Cheng Li,[1] Tobey J. B. Luck,[1] Manuel F. Ferrer-Garcia,[1] Jeremy Upham,[1] Jeff S. Lundeen,[1,2] and Robert W. Boyd[1,3,4]

[1]Nexus for Quantum Technologies, Department of Physics, University of Ottawa, Ottawa, Ontario K1N 6N5, Canada
[2]National Research Council of Canada, 100 Sussex Drive, Ottawa, Ontario K1A 0R6, Canada
[3]Institute of Optics, University of Rochester, Rochester, New York 14627, USA
[4]rboyd@uottawa.ca

Received 7 November 2025; revised 26 January 2026; accepted 27 January 2026; published 23 February 2026

Free-space quantum communications offers a promising route for securely transmitting information over long distances. However, a major challenge for these systems is atmospheric turbulence, which distorts the spatial structure of light and can severely limit the amount of information that can be reliably transmitted. In this work, we propose and demonstrate a turbulence-resilient scheme for free-space quantum communication. By leveraging the phase conjugation property of stimulated parametric down-conversion, our scheme enables all-optical dynamic correction of spatial-mode distortion induced by atmospheric turbulence, thereby enhancing the secure key rate in high-dimensional quantum key distribution. We develop a theoretical model that provides detailed guidelines for selecting the optimal basis and spatial properties needed to maximize the efficiency of the proposed scheme. Both numerical simulations and experimental results show that, even under strong turbulence, our scheme can reduce the quantum error rates well below the security threshold. These results highlight the potential of nonlinear optical approaches as powerful tools for robust quantum communication in realistic free-space environments. © 2026 Optica Publishing Group under the terms of the Optica Open Access Publishing Agreement

https://doi.org/10.1364/OPTICA.583778

1. INTRODUCTION

Quantum key distribution (QKD) enables two distant parties to share encryption keys with information-theoretic security, making it a cornerstone of proposed future communication networks [1]. While QKD was initially proposed on two-level quantum systems, high-dimensional QKD exploits larger Hilbert spaces, providing increased information capacity per photon, enhanced resilience to noise, and improved security against certain classes of attacks [2–4]. Different photonic degrees of freedom have been harnessed to implement high-dimensional QKD, with information encoded in frequency, time-bin, or transverse spatial modes [5–7]. In particular, transverse spatial modes, such as Hermite–Gaussian (HG) and Laguerre–Gaussian (LG) modes, retain their well-defined spatial structure during propagation under ideal conditions. This feature allows spatial modes of light to preserve the encoded information over long distances, making them attractive for free-space high-dimensional QKD implementations [8,9].

However, for QKD implementations in realistic free-space optical (FSO) scenarios, random dynamic fluctuations in the refractive index of air, caused by variations in temperature and pressure, induce phase and amplitude distortions in the propagating spatial modes [10]. These distortions reduce the mode fidelity of the transmitted states, impairing the retrieval of the encoded information at the receiver end [11–13].

Several solutions have been proposed and implemented to mitigate the effects of atmospheric turbulence in spatial mode transmission, such as digital adaptive optics and optical phase conjugation techniques. Adaptive optics methods use light modulation devices, such as spatial light modulators (SLMs) and deformable mirrors (DMs), to apply a digitally computed post-correction mask to the transmitted beam based on the channel distortion characterized by a probe beam. However, they typically require intensive data processing, and their effectiveness is limited by the computational time needed to both analyze and correct the optical distortions before the atmospheric conditions change again. Moreover, the response time of a commercial SLM for phase correction is typically limited to about 100 Hz [14], whereas that of the DM is up to 200 Hz [15,16]. In contrast, the characteristic fluctuation rate of dynamic atmospheric turbulence is on the order of 1 kHz for strong turbulence changes [10]. These limitations constrain the effectiveness of the adaptive optics

Research Article Vol. 13, No. 3 / March 2026 / Optica 387

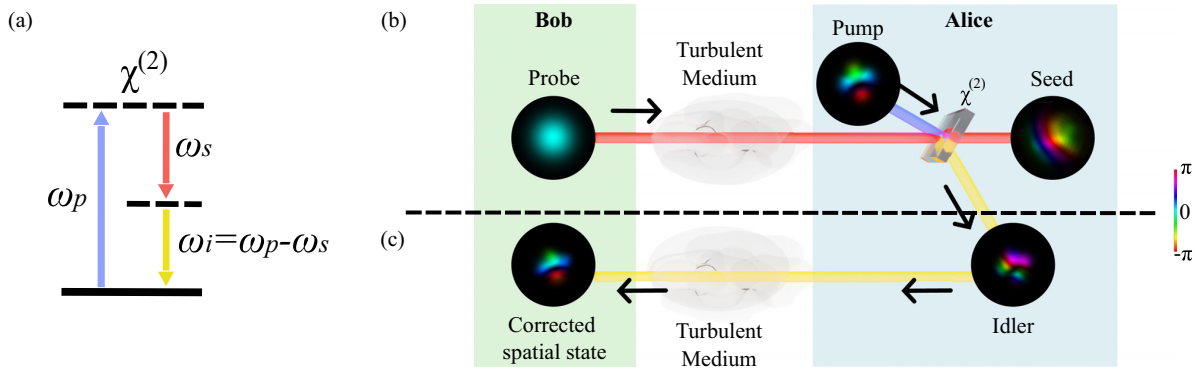


Fig. 1. (a) Energy level description of StimPDC. (b) StimPDC scheme: Bob sends a Gaussian beam through a turbulent transmission channel to probe the turbulence and thereby acquires phase distortions. Alice pumps a thin nonlinear crystal with a laser beam encoded with the spatial mode she wants to transmit to Bob. She also seeds the crystal along the signal path with the distorted probe beam. (c) As a result, the idler field carries Alice's target transmission mode together with the phase-conjugate of the turbulence distortions. For the degenerate situation in which the probe and idler fields have the same wavelength, phase distortions of the returning beam are canceled, and the intended spatial state is received.

techniques, especially for real-time aberration correction under strong turbulence. Recently, nonlinear optical processes such as four-wave mixing (FWM) have shown promising results due to their capacity to introduce optical phase conjugation, which conjugates the phase of an input beam and can be used to offset phase distortions acquired in the transmission channel. However, the response times of many commonly used $\chi^{(3)}$ materials for FWM have not been sufficiently fast, with measured values on the order of 10 mHz [17,18]. Although novel $\chi^{(3)}$ materials promise ultrafast FWM responses of 1 THz, characterizing their optical properties and achieving practical nonlinear conversion efficiency with them remain works in progress [19].

Recently, stimulated parametric down-conversion (StimPDC) has attracted increasing attention as an effective phase-conjugate process. Importantly, studies have demonstrated that StimPDC can generate phase conjugation of partially coherent beams, making this technique particularly suitable for correcting beams that have been distorted by turbulent media [20,21]. Furthermore, this three-wave-mixing nonlinear process has been shown to correct spatial modes affected by specific optical aberrations [22], as well as to recover images distorted by turbulence [23]. Although StimPDC-based optical phase conjugation is considered more experimentally challenging than its FWM-based counterpart [24], StimPDC offers an advantage for correcting dynamic aberrations due to its faster nonlinear response time. In particular, the nonlinear response time of $\chi^{(2)}$ materials has been demonstrated to be ultrafast, exceeding 1 THz, in commercially available nonlinear crystals [25].

In this work, we propose and demonstrate the first all-optical self-correction scheme for turbulence-resilient free-space high-dimensional QKD using StimPDC. Specifically, by exploiting the intrinsic phase conjugation property of the StimPDC (Fig. 1), we combine the spatial structure of the quantum state intended for transmission with the conjugate phase information of the turbulent channel, thereby embedding the correction within the nonlinear interaction. Unlike previous approaches that involve channel characterization in advance, our scheme does not require either party to have prior knowledge of the channel, as the nonlinear process inherently performs the compensation. We test our scheme's performance under varying turbulence conditions through numerical simulations and demonstrate its feasibility and effectiveness using a proof-of-principle experiment. These results offer a promising foundation for developing turbulence-resilient quantum FSO systems and could have implications for long-distance QKD and remote quantum networks.

2. PRINCIPLES OF THE STIMPDC SCHEME

Typically, the prepare-and-measure (P&M) QKD scheme for spatial modes of light (eigenmodes of the paraxial wave equation) relies on Alice's ability to efficiently transmit to Bob several sets of states $|U^{(b)}\rangle = \{|u_1^{(b)}\rangle, |u_2^{(b)}\rangle, \ldots, |u_d^{(b)}\rangle\}$ that each form an orthonormal basis b of dimension d; i.e.,

$$\langle u_j^{(n)} | u_{j'}^{(n)} \rangle = \delta_{j,j'}, \ j, j' = 1, \ldots, d, \ n = 1, \ldots, b, \quad (1)$$

and must be mutually unbiased bases (MUBs) with one another, meaning that the states that form each basis satisfy [8,9]

$$|\langle u_j^{(n)} | u_{j'}^{(n')} \rangle|^2 = \frac{1}{d}, \ j, j' = 1, \ldots, d, \ n \neq n' = 1, \ldots, b. \quad (2)$$

This property ensures that measurements in a mismatched basis yield completely random outcomes. As a result, an eavesdropper cannot gain any meaningful information by using a basis different from the one used for transmission. In this work, without loss of generality, we focus on the BB84-type protocols, in which one uses two sets of MUBs, each of dimension d.

In FSO scenarios, the phase aberrations introduced by atmospheric turbulence can be modeled by a spatially varying phase function $\phi_T(\vec{r}, \omega)$, which modifies and distorts the spatial profile of the state as a function of transverse position $\vec{r}$ and frequency ω [10,26]. A key measure of the system's performance is the crosstalk matrix $M^b_{j,j'} = |\langle u^{(b)}_{j,\text{Bob}} | u^{(b)}_{j',\text{Alice}} \rangle|^2$, which quantifies the overlap between the transmitted state $|u^{(b)}_{j',\text{Alice}}\rangle$ and the detected state $|u^{(b)}_{j,\text{Bob}}\rangle$. From this matrix, one can calculate the quantum error rate (QER) of the basis b induced by the turbulence, which is written as the fraction of erroneous detections relative to the total number of detection events in that basis:

$$Q_b = 1 - \frac{1}{d} \sum_{j=1}^{d} M^b_{j,j}. \quad (3)$$

Research Article Vol. 13, No. 3 / March 2026 / Optica 388

The average QER across all bases yields the total QER, denoted as Q. This metric reflects the average deviation from perfect orthogonality in the preparation and detection of spatial states, thereby serving as a global figure of merit for the communication link between Alice and Bob.

From the total QER value, the secure key rate r can be calculated using the following expression [4]:

$$r = \log_2(d) + 2(1-Q)\log_2(1-Q) + 2Q\log_2\left(\frac{Q}{d-1}\right). \quad (4)$$

The maximum tolerable error is determined by the value $Q_{\max}$ at which the secure key rate r drops to zero. This threshold increases with the dimension d, making high-dimensional protocols more resilient to communication errors and noise and thus more suitable for real-world implementations of quantum communication systems [27–30].

We propose a scheme based on StimPDC to overcome the undesired phase distortions introduced by atmospheric turbulence on the transmitted spatial states (i.e., to reduce Q). Parametric down-conversion (PDC) is a nonlinear optical process in which a pump beam with frequency ω_p interacts with a second-order nonlinear medium with a nonlinear susceptibility of $\chi^{(2)}$ to generate a signal and an idler photon. A StimPDC process refers to a PDC process seeded with a signal beam with frequency ω_s, which stimulates the generation of idler photons at frequency $\omega_i = \omega_p - \omega_s$ [Fig. 1(a)] [31]. Crucially, the idler field is related to the phase-conjugate of the seed beam. The scheme we propose is depicted in Figs. 1(b)–1(c), and is implemented as follows:

In contrast to the P&M scheme, Alice does not directly send her prepared states. Instead, she pumps a nonlinear crystal $\chi^{(2)}$ with a coherent state $|U_A\rangle$, prepared in a spatial mode $U_A(\vec{r})$ that belongs to a family of spatial modes satisfying the conditions given by Eqs. (1) and (2). This beam is characterized by beam waist w_A, Rayleigh range z_{RA}, and frequency ω_A. Meanwhile, Bob independently sends a coherent state $|U_B\rangle$, prepared in a Gaussian mode $U_B(\vec{r})$ with waist parameter w_B, Rayleigh range z_{RB}, and frequency ω_B through the shared turbulence channel of length Z_T connecting him with Alice. As it propagates toward Alice's stage, Bob's beam experiences wavefront distortions. We denote the state of the distorted beam as $|U_B^T\rangle$, which serves as a probe of the turbulence effects within the channel. Upon receiving the distorted probe beam from Bob, Alice seeds it into the signal path of the nonlinear process to stimulate the generation of the idler field with frequency $\omega_i = \omega_A - \omega_B$ [Fig. 1(b)].

The unnormalized stimulated contribution to the idler state obtained by Alice is [32]

$$|U_i\rangle \propto \iint \mathrm{d}\vec{q}_s\,\mathrm{d}\vec{q}_i\,\tilde{U}_A(\vec{q}_s,\vec{q}_i)\tilde{U}_B^{T*}(\vec{q}_s)|1,\vec{q}_i\rangle, \quad (5)$$

in which we have written the state vector in the Fock state representation (photon number = 1), with $\vec{q_{s(i)}}$ representing the transverse momentum of the signal(idler) beam, while $\tilde{U}_A(\vec{q})$ and $\tilde{U}_B(\vec{q})$ represent the angular spectrum of the pump and seed beams, respectively. As seen in Eq. (5), the spatial structure of the idler state is determined by the product of the spatial profile Alice aims to transmit and the conjugated phase information acquired by the probe beam as it propagates through the turbulent medium. It is worth noting that Eq. (5) describes the stimulated contribution to the idler field under the low-gain approximation, where only single-photon output states are considered, and higher-order multi-photon terms are neglected due to their negligible contribution to the overall field [32]. Even though the StimPDC process can generate multi-photon states, we note that these principles remain valid when using weak coherent beams, which are commonly employed in practical QKD implementations [27–29].

In the final step of this scheme, Alice sends the idler field back to Bob [Fig. 1(c)]. The idler photon now carries conjugated phase information of the turbulence that effectively offsets the phase distortions acquired during the return path. We note that since the phase aberrations introduced by the turbulent medium are dispersive, that is, inherently frequency-dependent, $\phi_T(\vec{r},\omega)$, it is important that the idler field has approximately the same frequency as Bob's probe beam ($\omega_i \approx \omega_B$). This condition is optimally fulfilled under fully degenerate conditions and sufficiently fulfilled in the near-degenerate regime.

3. ENGINEERING SPATIAL STATES WITH STIMPDC

The proposed scheme requires further optimization to fully exploit the distortion-correction capabilities of StimPDC. In particular, the choice of spatial basis for information transmission and the beam parameters of the seed, pump, and idler fields must enable maximal mode-transfer fidelity through StimPDC.

The reliability of spatial mode transfer via StimPDC, in the absence of turbulence, is quantified by the fidelity between the generated idler field state $|U_i\rangle$ and the pumped target state $|U_A\rangle$ to be transmitted by Alice. This fidelity is given by

$$F = |\langle U_A|U_i\rangle|^2 = \frac{\left|\int U_A^*(\vec{r})U_B^*(\vec{r})U_A(\vec{r})\mathrm{d}\vec{r}\right|^2}{\int |U_A(\vec{r})|^2\mathrm{d}\vec{r}\int |U_B^*(\vec{r})U_A(\vec{r})|^2\mathrm{d}\vec{r}}, \quad (6)$$

where normalization factors have been included for each state. As demonstrated in Ref. [33], the fidelity of spatial mode transfer depends solely on the ratio of the beam waists $\gamma = w_B/w_A$. High fidelities require $\gamma > 1$, meaning the seed beam must have a larger transverse extent than the target mode. This condition makes the overall fidelity of mode transmission dependent on the choice of basis. For instance, LG modes are less ideal choices since the sizes of their transverse profiles increase with mode orders, resulting in diminishing transmission fidelity at higher mode orders [33]. However, one can overcome this issue by using mode families in which all elements share the same optical diameter D, such as balanced superpositions of LG modes. We define D as the second-moment diameter of the spatial mode that will be transmitted through the channel [34].

We test our scheme using two sets of MUBs, namely MUB1 and MUB2. We use $d = 2$ to evaluate our scheme in a typical two-dimensional QKD system, and $d = 5$ to evaluate its performance in a high-dimensional QKD configuration. Therefore, we define MUB1 and MUB2 for each dimension. The states forming both MUBs are defined as superpositions of LG modes with zero radial index $q = 0$, with $l \in [-1, 1]$ for $d = 2$ and $l \in [-2, 2]$ for $d = 5$. The procedure for constructing both bases in each dimension is detailed in Supplement 1. These states are shown in Fig. 2(a). These bases satisfy both the orthonormality condition [Eq. (1)] and the mutual unbiasedness condition [Eq. (2)]. The dependence of fidelity [Eq. (6)] on γ is shown in Fig. 2(b). We confirm that the spatial states show highly uniform fidelity in each basis, as demonstrated in Ref [33]. For $\gamma = 1$, we obtain $F = 0.79$ for $d = 2$ and

Research Article Vol. 13, No. 3 / March 2026 / Optica 389

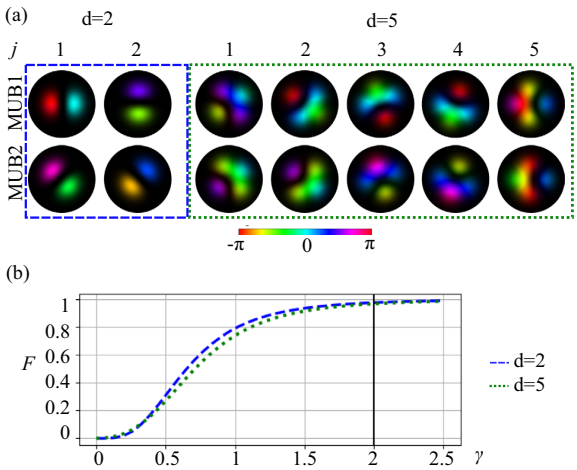


Fig. 2. (a) Amplitude and phase structure of the designed MUBs spatial states generated via StimPDC for $d = 2$ and $d = 5$. (b) Fidelity of the spatial basis generated with StimPDC as a function of the ratio $\gamma = w_B/w_A$. We see that for $\gamma = 2$ we obtain high fidelities for every element of each basis.

$F = 0.73$ for $d = 5$; while for $\gamma = 2$, the fidelities increase to $F = 0.97$ for both dimensions.

We therefore choose $\gamma = 2$ as the value for generating the desired spatial states with StimPDC. Under this condition, and with $\omega_B = \omega_i$, the remaining adjustable parameters are the beam waists w_B and w_i, which determine the optical diameters D_B and D_i. The optical diameter of a beam with OAM is given by [34]

$$D(z) = 2w_0 \sqrt{(|l| + 1)\left(1 + \left(\frac{z}{z_R}\right)^2\right)}, \tag{7}$$

where l is the topological charge, and $z_R = \frac{\pi w_0^2}{\lambda}$ is the Rayleigh range. In our case, the probe is a Gaussian beam ($l = 0$), while the transmitted spatial modes are superpositions of OAM states with a maximum $|l| = 2$ in the case of $d = 5$.

In the scheme, Bob has control over the probe beam's waist w_B and its corresponding Rayleigh range z_B. However, the idler field generated via StimPDC possesses a different waist w_i and, consequently, a different Rayleigh range z_i. These quantities can be evaluated within a classical model of StimPDC, as shown in Ref. [33], since the detection probability of $|U_i\rangle$ corresponds to the idler field intensity in the classical model, given by $|U_A(\vec{r})U_B^*(\vec{r})|^2$ [32]. Consequently, we can compute the beam diameters $D_B(z)$ and $D_i(z)$ at an arbitrary distance z along the propagation path. Figure 3 shows the analytically computed beam diameters of both the probe and the idler fields for different w_B values, for $\gamma = 2$ and $\lambda_B = 810$ nm, for $Z_T = 1$ km.

For the probe beam to adequately sample the spatial extent of the idler field along the turbulent path, we require $D_B(z) \geq D_i(z)$ for $z \in [0, Z_T]$. However, it is not convenient to arbitrarily enlarge w_B (i.e., D_B) as doing so would exacerbate the effects of turbulence. The reason behind this constraint is that the strength of turbulence experienced by an optical beam depends on the ratio between the beam's optical diameter D and the Fried parameter $r_0 = (0.423C_n^2k^2Z_T)^{-3/5}$, where C_n^2 is the refractive index structure constant, and k is the optical wavenumber [10,26].

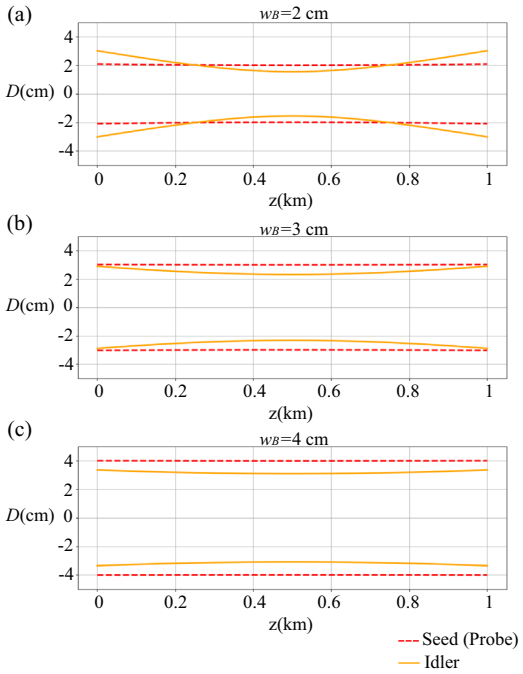


Fig. 3. Optical diameter of the probe beam sent by Bob and the stimulated idler field generated by Alice, shown for several different probe beam waists: (a) 2 cm, (b) 3 cm, and (c) 4 cm. There exists a specific value of w_B for which the condition $D_B(Z_T) = D_i(Z_T)$ is satisfied, corresponding in this case to scenario (b). Although scenario (c) satisfies the proposed criterion to a greater extent, it also amplifies the aberrations introduced by turbulence.

One can interpret the quantity D/r_0 as the number of atmospheric eddies (given that r_0 characterizes the spatial coherence length of the atmospheric eddies) within the beam's transverse profile. Therefore, D_B increases with the strength of turbulence. To address this issue, we adopt a practical optimization criterion aimed at minimizing D_B, regardless of the r_0 value of the channel: choose w_B such that $D_B(Z_T) = D_i(Z_T)$. We note that this condition is not unique to our scheme, as any adaptive optics scheme relying on a beacon beam is subject to the same constraint [15,16]. As an example, for $Z_T = 1$ km, this yields $w_B \approx 3$ cm, as seen in Fig. 3(b). This condition applies to systems with a fixed channel distance. If, instead, the protocol must operate over variable distances, the condition can be relaxed to $D_B(Z_T) > D_i(Z_T)$ by employing larger optical apertures on both the transmitter and the receiver sides, at the expense of accepting stronger turbulence influences, as seen in Fig. 3(c).

In our scheme, the idler field has a smaller diameter than the probe beam and thus experiences a different level of turbulence-induced distortions. However, both beams are subject to the same spatial phase modulations $\phi_T(\vec{r}, \omega)$. It is also worth mentioning that it is not possible for Alice to arbitrarily adjust the beam waist and Rayleigh range of the idler field, since this would simultaneously modify its transverse phase structure $\phi_T(\vec{r}, \omega)$, which would introduce additional aberrations into the idler field.

Research Article Vol. 13, No. 3 / March 2026 / Optica 390

4. TESTING THE STIMPDC SCHEME

A. Numerical Simulations

We employ the standard split-step method for simulating beam propagation through turbulence [11,26]. Here, the propagation path is divided into small segments where free-space propagation and turbulent phase masks are applied sequentially: each step consists of free-space propagation via the angular spectrum method, followed by a statistically accurate phase screen based on the Kolmogorov power spectrum, which represents the spatially varying phase distortions induced by atmospheric turbulence. Repetitively performing these operations models the cumulative effect of turbulence along the entire path, thereby generating both phase and amplitude distortions in the originally propagated beam. Comprehensive details of these simulations, together with the procedures for generating the employed phase masks, are presented in Supplement 1.

We test the scheme using the MUBs derived in the previous section, along with their established optimal beam parameters ($\gamma = 2$, $\lambda_B = 810$ nm, and $w_B = 3$ cm for $Z_T = 1$ km). As a representative example, in Figs. 4(a) and 4(b), we present simulated amplitude and phase profiles for the case $d = 2$ with the state $|u_1^{(2)}\rangle$, and for $d = 5$ with the state $|u_3^{(1)}\rangle$. We investigate both cases under turbulence conditions of $D_B/r_0 = [1, 5]$, which effectively cover regimes ranging from moderate ($D_B/r_0 = 1$) to strong turbulence ($D_B/r_0 = 5$). We note that our qualitative description of turbulence strength ("moderate/strong") is consistent with that used in existing literature [16,35]. Specifically, in Ref. [16], the turbulence strength of a free-space channel across a university campus with $D_B/r_0 = 1.03$ to 2.98 is described as "moderate to strong"; and in Ref. [35], the turbulence strength of a 143 km channel between two islands, which is characterized by $D = 35$ mm and $r_0 = 1.3$ cm ($D_B/r_0 \approx 2.7$), is referred to as "strong."

To demonstrate the advantage of the StimPDC scheme over the standard P&M approach, we simulate the transmission of spatial states for both schemes under the same conditions. We then compute the fidelity matrix $F^b_{j,j'}$ as the overlap between the retrieved mode j and the ideal mode j', for all states across both MUBs in each dimension. We evaluate the average fidelity F of both MUBs for $j = j'$. To obtain statistically consistent results, we averaged over 50 realizations of spatial state transmission through turbulence. To better compare the performance of both schemes, we use the average fidelity loss $\Delta F = 1 - F$ to quantify their resistance to turbulence. For the P&M approach, we identify

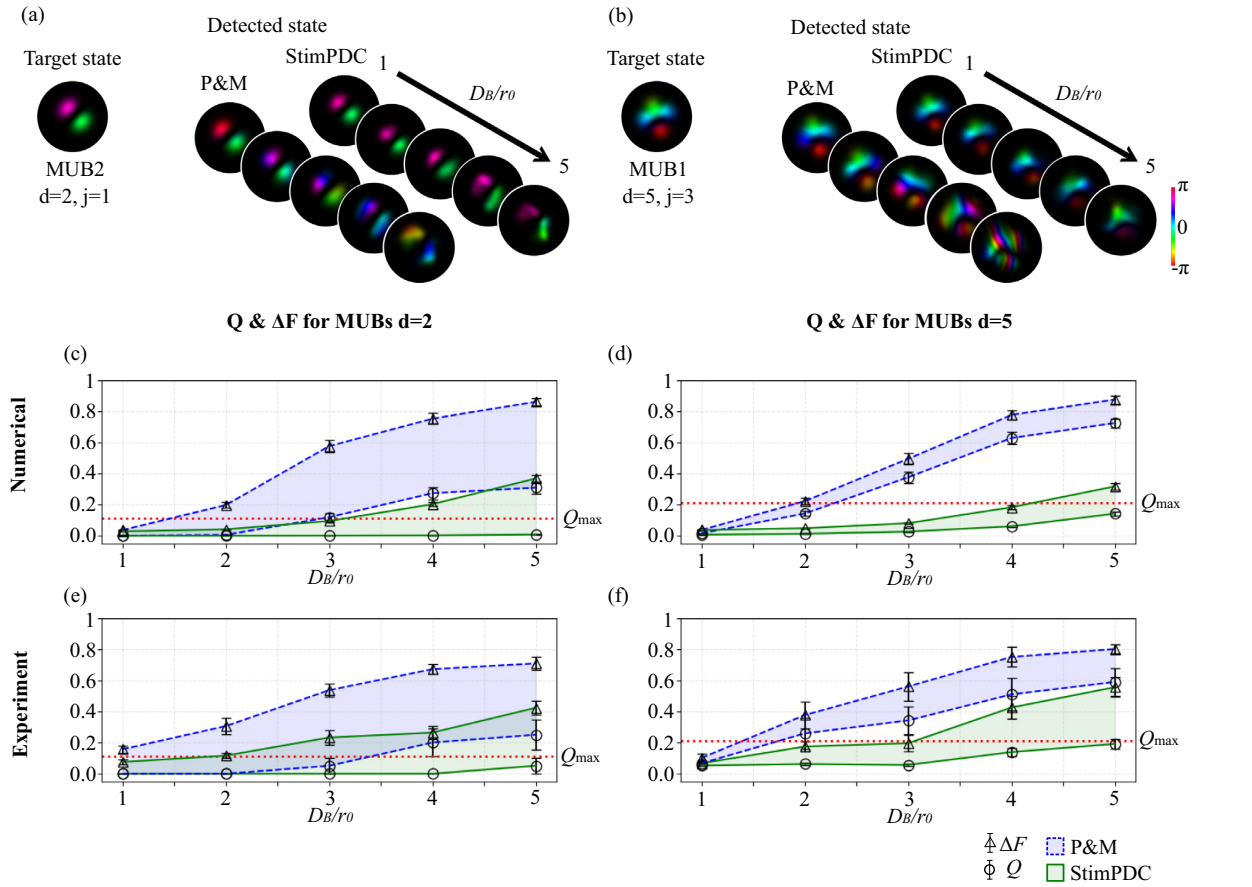


Fig. 4. Field simulation results for (a) MUB2, $d = 2$, $j = 1$ and (b) MUB1, $d = 5$, $j = 3$. The target state is shown along with the spatial states distorted by turbulence and corrected by our scheme. With the StimPDC scheme, it can be observed that the amplitude retains the same aberration, as in the P&M case. However, the phase resembles that of the original beam. Panels (c) and (d) show QER (Q) and fidelity loss (ΔF) for the P&M and StimPDC schemes using MUB1 and MUB2 for $d = 2$ and $d = 5$ obtained with the split-step method. Panels (e) and (f) present the experimental results. The error bars correspond to the standard error. The shaded area highlights the difference between the QER and the fidelity loss, indicating that the latter does not fully account for the observed crosstalk reduction.

Research Article Vol. 13, No. 3 / March 2026 / *Optica* 391

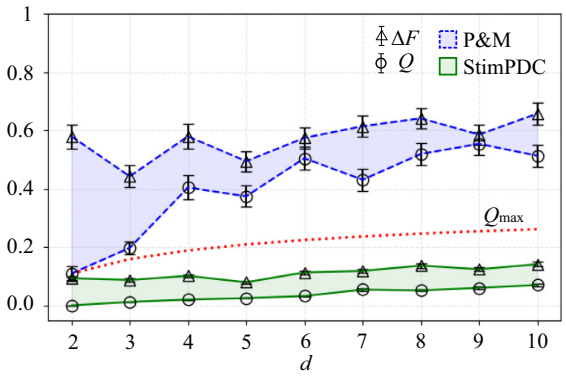


Fig. 5. QER (Q) and fidelity loss (ΔF) for the P&M and StimPDC schemes using MUB1 and MUB2 for $d = [2, 10]$, obtained with the split-step method for $D_B/r_0 = 3$. For all dimensions, the StimPDC scheme maintains $Q < Q_{\max}$.

that for $D_B/r_0 = 1$, the fidelity loss remains below 5%, while for $D_B/r_0 = 5$, the fidelity loss is nearly complete, increasing to almost 95%. Figures 4(c) and 4(d) show ΔF for MUBs with $d = 2$ and $d = 5$, respectively. For both dimensions, the P&M method exhibits up to a 90% fidelity loss, whereas our StimPDC scheme retains fidelity with losses limited to only about 30%.

Our scheme demonstrates improved fidelity over the P&M scheme with some residual fidelity loss. This is because the turbulence effects are only partially corrected, since the probe beam does not experience the same level of distortions as the spatial mode under test. However, this fidelity loss is not entirely related to modal crosstalk, but rather from residual aberrations that distort the ideal spatial profile, as seen in the examples of Figs. 4(a) and 4(b). To confirm this, we compute the QER from the normalized crosstalk matrix, which is defined as $M^b_{j,j'} = F^b_{j,j'} / \sum_{j'} F^b_{j,j'}$ [36], and display the calculated QER in Figs. 4(c) and 4(d).

As shown in Figs. 4(c) and 4(d), states with $d = 2$ show greater resilience to crosstalk, which can be attributed to their HG mode structure. HG modes have a Cartesian spatial profile without a central phase singularity, making them less sensitive to small angular distortions and to the loss of azimuthal symmetry [37–39]. Nevertheless, when $D_B/r_0 > 2$, the P&M scheme suffers from crosstalk-induced QER that surpasses the maximum tolerable error threshold $Q_{\max}$, rendering information transmission entirely ineffective, regardless of state dimensionalities. Finally, we demonstrate that the efficiency of our scheme is not dimension-dependent. Figure 5 presents the numerically simulated QER and fidelity loss for high-dimensional QKD ($d = [2, 10]$) at $D_B/r_0 = 3$, which are evaluated for different MUB1 and MUB2 sets. We show that, across all dimensions, the QER consistently remains below $Q_{\max}$, confirming the robustness and effectiveness of our protocol in mitigating crosstalk for high-dimensional QKD systems based on spatial states. It is worth noting that, as the dimensionality increases, the used spatial modes become more complex in their phase and amplitude distributions, which causes ΔF and Q to increase with both turbulence strength and dimension. While it is still important at any dimension to select a basis that is more resilient to turbulence, both the turbulence-resilient bases and those that are more susceptible to distortions will benefit from the StimPDC scheme [40].

B. Experiment

We use the setup shown in Fig. 6(a) to perform a proof-of-principle experiment. A collimated 405 nm beam illuminates spatial light modulator 1 (SLM1), which has been calibrated for this wavelength and is used to encode the desired spatial mode through standard holographic techniques. All selected parameters follow the optimization criteria described in Section 3. The structured pump beam, with power ≈ 1 mW, and a beam waist radius $w_A = 0.13$ cm ($D_A = 0.26\sqrt{3} = 0.45$ cm), is then imaged onto a 2 mm long beta-barium borate (BBO) crystal (cut for type-II phase matching) using a telescope composed of lenses with focal lengths $f_1 = 500$ mm and $f_2 = 250$ mm. A second collimated Gaussian beam at 780 nm, with power ≈ 20 mW, and a beam waist radius of $w_B = 0.25$ cm ($D_B = 0.5$ cm), propagates through a free-space path of length $Z_T = 1$ m to the nonlinear crystal. At the midpoint, it illuminates the right-half region of SLM2, where we encode phase masks that simulate atmospheric turbulence if needed. These phase masks are generated using the same numerical method described in the simulation section of Supplement 1, allowing us to recreate the effect of a turbulent channel on the probe beam for $D_A/r_0 \in [1, 5]$. The beam is then demagnified using a telescope with lenses $f_3 = 500\ mm$ and $f_4 = 250\ mm$, and subsequently seeded into the BBO crystal at an angle of 4° with respect to the pump beam, resulting in the generation of StimPDC with $\gamma = w_B/w_A \approx 2$.

First, to test the spatial states in the absence of turbulence, we modulate the pump beam with spatial modes within the chosen MUBs using SLM1, generating the MUB spatial states for both $d = 2$ and $d = 5$. The right-half region of SLM2 displays a flat, turbulence-free, phase profile. The generated idler field is collected using a magnifying telescope with lenses $f_5 = 250$ mm and $f_6 = 500$ mm and directed to the left-half region on SLM2, which is separated from the region illuminated by the probe beam. Figure 6(b) shows the intensity distributions of the generated modes at the plane of SLM2. In this left-half region of the SLM2, we encode a projection onto the target spatial mode. It is worth noting that, since our experiment is carried out in the near-degenerate StimPDC regime, we have calibrated SLM2 to operate at 810 nm, which is the wavelength at degenerate phase matching. Finally, the beam is sent through a Fourier lens $f_7 = 500$ mm, and the intensity at the center of the optical axis is measured using a CMOS camera in the Fourier plane. This central intensity provides an estimate of the modal overlap $|\langle u^{(b)}_j | u^{(b')}_{j'} \rangle|^2$ (please refer to Supplement 1 for more details) [28,41]. Then, we measure the fidelity and crosstalk matrices in the absence of turbulence. The results are shown in Fig. 6(c), experimentally confirming that the QKD conditions given by Eqs. (1) and (2) are satisfied.

To evaluate the P&M scheme under turbulence, we pump the crystal with the selected MUB states using SLM1. The right-half region of SLM2 still displays a flat, turbulence-free phase profile, allowing us to seed the StimPDC process with an unaberrated Gaussian beam. Meanwhile, turbulent phase masks simulating different turbulence strengths are applied to the left-half region of SLM2, along with the projection of the target spatial mode.

To evaluate the StimPDC scheme, we follow the same procedure; however, in this case, we apply the same turbulent phase mask to both the seed and idler fields (i.e., to both regions of SLM2), so that the seed beam now acts as a probe for the turbulent channel. The phase conjugation then automatically compensates for the influence of turbulence on the idler field. For both the P&M

Research Article Vol. 13, No. 3 / March 2026 / Optica 392

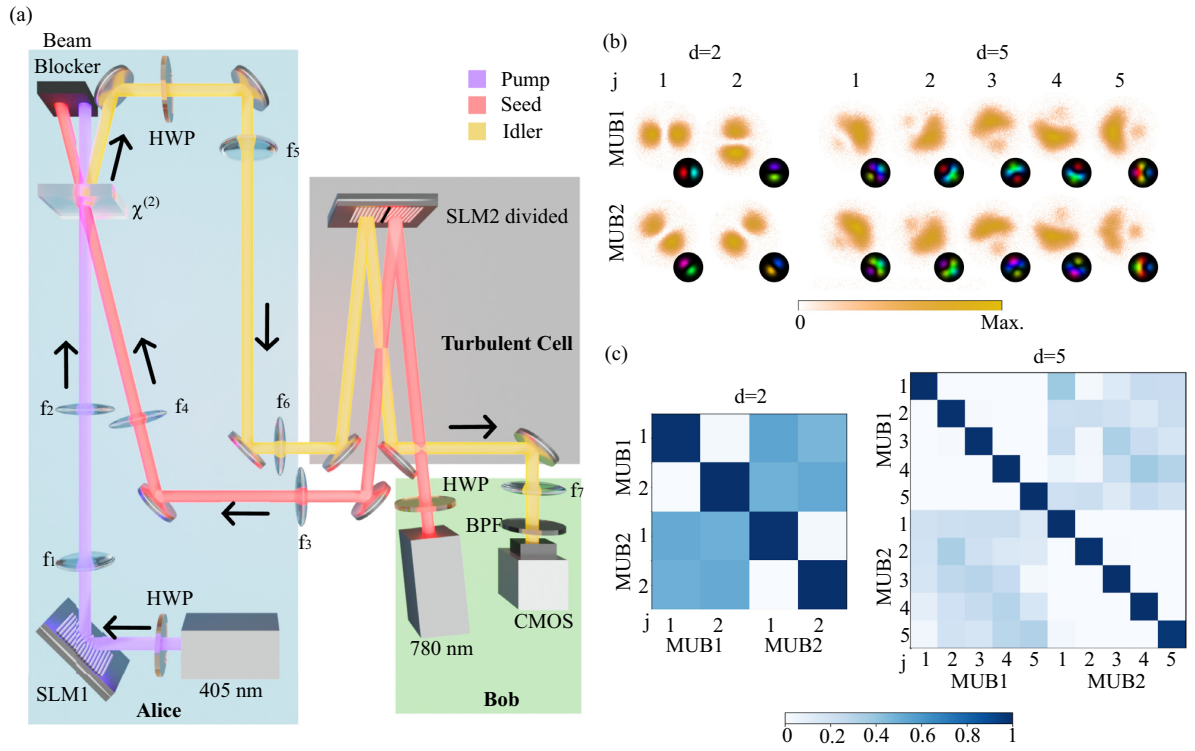


Fig. 6. (a) Experimental setup. Alice pumps the spatial state she intends to share with Bob with a 405 nm laser, while simultaneously seeds the 780 nm beam sent by Bob through the turbulent cell. This process generates StimPDC at 840 nm. The resulting beam is then sent back through the turbulent cell so that Bob can receive the state. (b) Normalized intensities of the idler field, obtained at the SLM2 plane using the CMOS camera, are shown for the previously chosen MUBs in cases of $d = 2$ and $d = 5$. (c) The corresponding normalized crosstalk matrices for both dimensions are also presented, experimentally confirming that the QKD conditions given by Eqs. (1) and (2) are satisfied.

and StimPDC schemes, we measure the crosstalk matrices and calculate the QER for each basis. The results are averaged over 50 turbulence realizations, which is done by applying different phase masks. The corresponding data for $d = 2$ is presented in Fig. 4(e), and that for $d = 5$ in Fig. 4.

Our results for the P&M scheme are in consistent agreement with previous studies that employed the same modal bases for $d = 2$ [39] and for $d = 5$ [40]. Moreover, our measurements for the StimPDC scheme are in good agreement with our theoretical predictions. The remaining discrepancies between numerical and experimental values can be attributed to measurement noise, with the signal-to-noise ratio estimated to be approximately 15 dB for $j = j'$. Even with these limitations, we demonstrate that fidelities can be improved by up to 30% for the MUBs with $d = 2$ and by up to 20% for the MUBs with $d = 5$ under the strongest turbulence conditions. More importantly, with our scheme, the average QER remains consistently below the corresponding $Q_{\max}$ values for both MUBs across all turbulence levels studied. This result confirms the robustness of our approach in transmitting higher security key rates under adverse propagation conditions, highlighting its potential for practical implementations in quantum key distribution and high-dimensional quantum communication through turbulent channels.

In our experiment, which employs continuous-wave pump and probe beams, the measured photon conversion efficiency from the probe field to the idler field is $\eta \approx 10^{-5}\%$ for both MUBs of $d = 2$, and $\eta \approx 10^{-6}\%$ for both MUBs of $d = 5$. It is worth noting that significantly higher StimPDC efficiencies, reaching up to 78%, have been reported in pulsed systems [42].

5. DISCUSSION AND CONCLUSION

In our proof-of-principle experiment, the idler field operates in the classical regime. However, it can be attenuated to the weak coherent state regime, so that one can employ our scheme to mitigate the influence of turbulence in practical QKD implementations using weak coherent structured optical fields [43–45]. It is worth noting that if the probe beam is in the single photon regime, spontaneous emission becomes as efficient as stimulated emission, generating non-negligible noise in the channel [46].

Regarding scheme security, it is worth noting that even if an eavesdropper were able to acquire complete knowledge of the turbulence-induced structure of the channel, the security of the communication would remain guaranteed by the assumptions associated with the idler state in the employed QKD protocol. However, since the mean photon number of Alice's source depends on the probe power, the channel may be vulnerable to laser-seeding attacks, which allow an adversary to increase the photon number and perform photon-number-splitting attacks [47]. This can be mitigated by operating above the probe saturation power, where additional injected power does not affect the idler photon number [42]. Importantly, the saturation power depends on the pump power and can be set to experimentally feasible values [48]. Any attempt by Eve to modify the photon number per mode via

Research Article Vol. 13, No. 3 / March 2026 / Optica 393

structured probe injection would manifest as detectable deviations in Bob's measurement statistics, leading to protocol abortion. Therefore, we believe that our scheme does not introduce additional security vulnerabilities beyond those of the underlying QKD protocol [49].

Since our scheme is intended for free-space operation, information losses in realistic implementations are unavoidable. In particular, atmospheric absorption and scattering inevitably reduce the number of photons reaching the receiver. Moreover, in practical implementations, the transmitter's and receiver's apertures may not be sufficiently large to efficiently capture all the employed spatial modes, leading to a degradation in the fidelity of the received states [50]. However, it is well established that the security conditions of QKD can be satisfied independently of the total channel loss under normal operating conditions when using weak coherent states [51]. Specifically, channel losses may reduce the achievable secret key rate but do not, by themselves, compromise the security of the protocol.

Another potential source of noise could arise from the counter-propagating geometry of the scheme, in which the classical probe beam and the weak coherent idler field share the same optical path. This issue can be mitigated through appropriate filtering of the two fields. In our proof-of-principle experiment, we employ two distinct but closely spaced wavelengths for the probe and idler fields, which allows straightforward wavelength filtering using a simple frequency filter. While this wavelength difference does not constitute a limiting factor for the correction scheme under our experimental conditions, over longer propagation distances, the accumulated phase mismatch between slightly different wavelengths may lead to an increased QER [52]. This limitation can be overcome by employing degenerate type-II StimPDC, in which the probe and idler fields operate at the same wavelength but in orthogonal polarization states, since it is well established that atmospheric turbulence does not induce significant polarization-mode mixing [10].

In conclusion, we have proposed and demonstrated a novel quantum communication scheme based on StimPDC to mitigate the degrading effects of atmospheric turbulence in FSO high-dimensional QKD. By exploiting the intrinsic phase-conjugation properties of StimPDC, our scheme allows the spatial structure of a quantum signal to self-correct without prior knowledge of the turbulent channel.

We developed a theoretical model to guide the optimal selection of spatial modes and system parameters for implementing the proposed scheme and verified its performance through numerical simulations and a proof-of-principle experiment. Our results show that the proposed scheme significantly reduces the QER, which in turn increases the secure key rate of the protocol across different turbulence levels. In particular, we demonstrated improvements of up to 50% over conventional P&M approaches, maintaining QERs below the security threshold even under strong turbulence.

These findings highlight the potential of nonlinear optical techniques, particularly StimPDC, for robust and scalable quantum communication in realistic atmospheric conditions. Our work provides a pathway toward implementing high-dimensional QKD systems with improved noise resilience. Moreover, this technique could potentially be expanded to aberration correlation in microscopy and sensing applications based on information encoding with spatial modes of light, leading to novel schemes for quantum-enhanced imaging and metrology.

Funding. Canada Research Chairs (950-231657); Natural Sciences and Engineering Research Council of Canada (ALLRP 578468-22, RGPIN/2017 06880).

Disclosures. The authors declare no conflicts of interest.

Data availability. Data underlying the results presented in this paper are available from the corresponding author upon reasonable request.

Supplemental document. See Supplement 1 for supporting content.

REFERENCES

1. C. H. Bennett and G. Brassard, "Quantum cryptography: public key distribution and coin tossing," in *Proceedings of IEEE International Conference on Computers, Systems and Signal Processing*, Bangalore, India (IEEE, 1984), pp. 175–179.
2. H. Bechmann-Pasquinucci and W. Tittel, "Quantum cryptography using larger alphabets," Phys. Rev. A **61**, 062308 (2000).
3. N. J. Cerf, M. Bourennane, A. Karlsson, *et al.*, "Security of quantum key distribution using *d*-level systems," Phys. Rev. Lett. **88**, 127902 (2002).
4. K. Brádler, M. Mirhosseini, R. Fickler, *et al.*, "Finite-key security analysis for multilevel quantum key distribution," New J. Phys. **18**, 073030 (2016).
5. K.-C. Chang, X. Cheng, M. C. Sarihan, *et al.*, "Recent advances in high-dimensional quantum frequency combs," Newton **1**, 100024 (2025).
6. I. Vagniluca, B. Da Lio, D. Rusca, *et al.*, "Efficient time-bin encoding for practical high-dimensional quantum key distribution," Phys. Rev. Appl. **14**, 014051 (2020).
7. F. Xu, X. Ma, Q. Zhang, *et al.*, "Secure quantum key distribution with realistic devices," Rev. Mod. Phys. **92**, 025002 (2020).
8. M. Mafu, A. Dudley, S. Goyal, *et al.*, "Higher-dimensional orbital-angular-momentum-based quantum key distribution with mutually unbiased bases," Phys. Rev. A **88**, 032305 (2013).
9. F. Bouchard, K. Heshami, D. England, *et al.*, "Experimental investigation of high-dimensional quantum key distribution protocols with twisted photons," Quantum **2**, 111 (2018).
10. L. Andrews and R. Phillips, *Laser Beam Propagation Through Random Media*, Online Access with Subscription: SPIE Digital Library (Society of Photo Optical, 2005).
11. C. Peters, V. Cocotos, and A. Forbes, "Structured light in atmospheric turbulence—a guide to its digital implementation: tutorial," Adv. Opt. Photonics **17**, 113–184 (2025).
12. T. Doster and A. T. Watnik, "Laguerre–Gauss and Bessel–Gauss beams propagation through turbulence: analysis of channel efficiency," Appl. Opt. **55**, 10239–10246 (2016).
13. P. Lochab, P. Senthilkumaran, and K. Khare, "Propagation of converging polarization singular beams through atmospheric turbulence," Appl. Opt. **58**, 6335–6345 (2019).
14. Y. Zhou, J. Zhao, B. Braverman, *et al.*, "Multiprobe time reversal for high-fidelity vortex-mode-division multiplexing over a turbulent free-space link," Phys. Rev. Appl. **15**, 034011 (2021).
15. L. Scarfe, F. Hufnagel, M. F. Ferrer-Garcia, *et al.*, "Fast adaptive optics for high-dimensional quantum communications in turbulent channels," Commun. Phys. **8**, 79 (2025).
16. J. Zhao, Y. Zhou, B. Braverman, *et al.*, "Performance of real-time adaptive optics compensation in a turbulent channel with high-dimensional spatial-mode encoding," Opt. Express **28**, 15376–15391 (2020).
17. H. Zhou, Y. Duan, H. Song, *et al.*, "Automatic turbulence mitigation for coherent free-space optical links using crystal-based phase conjugation and fiber-coupled data modulation," Opt. Lett. **48**, 2194–2197 (2023).
18. H. Zhou, X. Su, Y. Duan, *et al.*, "Automatic mitigation of dynamic atmospheric turbulence using optical phase conjugation for coherent free-space optical communications," Optica **12**, 158–167 (2025).
19. M. Z. Alam, I. De Leon, and R. W. Boyd, "Large optical nonlinearity of indium tin oxide in its epsilon-near-zero region," Science **352**, 795–797 (2016).
20. G. H. dos Santos, A. G. de Oliveira, N. Rubiano da Silva, *et al.*, "Phase conjugation of twisted Gaussian Schell model beams in stimulated down-conversion," Nanophotonics **11**, 763–770 (2022).
21. G. H.dos Santos, A. L. S. Santos Junior, M. Gil de Oliveira, *et al.*, "Experimental investigation of twist conservation in nonlinear optical three-wave mixing," Phys. Rev. Appl. **24**, 034075 (2025).

22. S. Singh, B. Sephton, W. Tavares Buono, *et al.*, "Light correcting light with nonlinear optics," Adv. Photonics **6**, 026003 (2024).
23. X. Zou, P. Hong, and Y. J. Ding, "Recovery of image distorted by turbulent atmosphere using phase-conjugate image generated by difference frequency generation," Appl. Phys. Lett. **105**, 241105 (2014).
24. A. Yariv, "Phase conjugate optics and real-time holography," IEEE J. Quantum Electron. **14**, 650–660 (1978).
25. H. Wang, K. Li, Z. Hu, *et al.*, "Ultrafast modulation of second harmonic waves through polarization selective interferometric autocorrelation," PhotoniX **6**, 18 (2025).
26. K. Khare, P. Lochab, and P. Senthilkumaran, *Orbital Angular Momentum States of Light: Propagation Through Atmospheric Turbulence*Advances in Optics, Photonics and Optoelectronics Series (Institute of Physics Publishing, 2020).
27. S.-K. Liao, W.-Q. Cai, W.-Y. Liu, *et al.*, "Satellite-to-ground quantum key distribution," Nature **549**, 43–47 (2017).
28. J. Meyer, Y. Reches, G. Gary Rozenman, *et al.*, "Analogy of free-space quantum key distribution using spatial modes of light: scaling up the distance and the dimensionality," Opt. Lett. **50**, 3297–3300 (2025).
29. J. Li, H. Han, J. Huang, *et al.*, "Doughnut-biting photon capturing scheme for drone-based orbital angular momentum quantum key distribution," Opt. Express **33**, 12304–12317 (2025).
30. M. Mirhosseini, O. S. Magaña-Loaiza, M. N. O'Sullivan, *et al.*, "High-dimensional quantum cryptography with twisted light," New J. Phys. **17**, 033033 (2015).
31. P. H. S. Ribeiro, S. Pádua, and C. H. Monken, "Image and coherence transfer in the stimulated down-conversion process," Phys. Rev. A **60**, 5074–5078 (1999).
32. A. G. de Oliveira, N. Rubiano da Silva, R. Medeiros de Araújo, *et al.*, "Quantum optical description of phase conjugation of vector vortex beams in stimulated parametric down-conversion," Phys. Rev. Appl. **14**, 024048 (2020).
33. A. A. Aguilar-Cardoso, C. Li, T. J. B. Luck, *et al.*, "Tailoring spatial modes produced by stimulated parametric down-conversion," Phys. Rev. A **112**, 043541 (2025).
34. V. Cocotos and A. Forbes, "Orbital angular momentum with topologically controlled beam sizes," J. Opt. **27**, 07LT01 (2025).
35. M. Krenn, J. Handsteiner, M. Fink, *et al.*, "Twisted light transmission over 143 km," Proc. Natl. Acad. Sci. **113**, 13648–13653 (2016).
36. Y. Zhou, B. Braverman, A. Fyffe, *et al.*, "High-fidelity spatial mode transmission through a 1-km-long multimode fiber via vectorial time reversal," Nat. Commun. **12**, 1866 (2021).
37. X. Gu, L. Chen, and M. Krenn, "Phenomenology of complex structured light in turbulent air," Opt. Express **28**, 11033–11050 (2020).
38. S. Restuccia, D. Giovannini, G. Gibson, *et al.*, "Comparing the information capacity of Laguerre–Gaussian and Hermite–Gaussian modal sets in a finite-aperture system," Opt. Express **24**, 27127–27136 (2016).
39. M. A. Cox, L. Maqondo, R. Kara, *et al.*, "The resilience of Hermite- and Laguerre-Gaussian modes in turbulence," J. Light. Technol. **37**, 3911–3917 (2019).
40. R. Abolhassani, L. Scarfe, F. Di Colandrea, *et al.*, "Investigating the performance of adaptive optics on different bases of spatial modes in turbulent channels," Opt. Express **34**, 3732–3743 (2026).
41. J. Pinnell, I. Nape, B. Sephton, *et al.*, "Modal analysis of structured light with spatial light modulators: a practical tutorial," J. Opt. Soc. Am. A **37**, C146–C160 (2020).
42. R. T. Murray, T. H. Runcorn, E. J. R. Kelleher, *et al.*, "Highly efficient mid-infrared difference-frequency generation using synchronously pulsed fiber lasers," Opt. Lett. **41**, 2446–2449 (2016).
43. C. Sekga and M. Mafu, "Measurement device-independent quantum key distribution with vector vortex modes under diverse weather conditions," Sci. Rep. **13**, 14931 (2023).
44. Z. Sun, Y. Li, and H. Ma, "Experimental high-dimensional quantum key distribution with orbital angular momentum," J. Opt. Soc. Am. B **41**, 351–355 (2023).
45. L. Wang, S.-M. Zhao, L.-Y. Gong, *et al.*, "Free-space measurement-device-independent quantum-key-distribution protocol using decoy states with orbital angular momentum," Chin. Phys. B **24**, 120307 (2015).
46. T. J. B. Luck, A. A. Aguilar-Cardoso, C. Li, *et al.*, "Description of single-photon orbital angular momentum conjugation with stimulated parametric down-conversion [Invited]," J. Opt. Soc. Am. B **43**, A37–A45 (2025).
47. A. Huang, A. Navarrete, S.-H. Sun, *et al.*, "Laser-seeding attack in quantum key distribution," Phys. Rev. Appl. **12**, 064043 (2019).
48. R. W. Boyd, *Nonlinear Optics*, 4th ed. (Academic, 2020).
49. S. Sun and A. Huang, "A review of security evaluation of practical quantum key distribution system," Entropy **24**, 260 (2022).
50. K. D. Ridley and E. Jakeman, "Incomplete phase conjugation through a random phase screen. II. Numerical simulations," J. Opt. Soc. Am. A **13**, 2393–2402 (1996).
51. W.-Y. Hwang, "Quantum key distribution with high loss: toward global secure communication," Phys. Rev. Lett. **91**, 057901 (2003).
52. J. Wu, X. Ke, W. Kang, *et al.*, "Study on the difference of wavefront distortion on beams caused by wavelength differences in weak turbulence region," Photonics **10**, 725 (2023).

Bibliography

[1] A. E. Willner, H. Huang, Y. Yan, Y. Ren, N. Ahmed, G. Xie, C. Bao, L. Li, Y. Cao, Z. Zhao, J. Wang, M. P. J. Lavery, M. Tur, S. Ramachandran, A. F. Molisch, N. Ashrafi, and S. Ashrafi. Optical communications using orbital angular momentum beams. *Adv. Opt. Photon.*, 7(1):66–106, Mar 2015.

[2] Manuel Erhard, Robert Fickler, Mario Krenn, and Anton Zeilinger. Twisted photons: new quantum perspectives in high dimensions. *Light: Science & Applications*, 7(3):17146–17146, Mar 2018.

[3] Jian Wang, Jeng-Yuan Yang, Irfan M. Fazal, Nisar Ahmed, Yan Yan, Hao Huang, Yongxiong Ren, Yang Yue, Samuel Dolinar, Moshe Tur, and Alan E. Willner. Terabit free-space data transmission employing orbital angular momentum multiplexing. *Nature Photonics*, 6(7):488–496, Jul 2012.

[4] Alois Mair, Alipasha Vaziri, Gregor Weihs, and Anton Zeilinger. Entanglement of the orbital angular momentum states of photons. *Nature*, 412(6844):313–316, Jul 2001.

[5] Mohammad Mirhosseini, Omar S Magaña-Loaiza, Malcolm N O'Sullivan, Brandon Rodenburg, Mehul Malik, Martin P J Lavery, Miles J Padgett, Daniel J Gauthier, and Robert W Boyd. High-dimensional quantum cryptography with twisted light. *New Journal of Physics*, 17(3):033033, 2015.

[6] Giuseppe Vallone, Vincenzo D'Ambrosio, Anna Sponselli, Sergei Slussarenko, Lorenzo Marrucci, Fabio Sciarrino, and Paolo Villoresi. Free-space quantum key distribution by rotation-invariant twisted photons. *Phys. Rev. Lett.*, 113:060503, Aug 2014.

[7] Larry C Andrews and Ronald L Phillips. *Laser Beam Propagation Through Random Media*, volume 152. SPIE Press, Bellingham, Washington, 2nd edition, 2005.

[8] C. Paterson. Atmospheric turbulence and orbital angular momentum of single photons for optical communication. *Phys. Rev. Lett.*, 94:153901, Apr 2005.

[9] A. Yariv. Phase conjugate optics and real-time holography. *IEEE Journal of Quantum Electronics*, 14(9):650–660, 1978.

[10] B. Ya. Zel'dovich, N. F. Pilipetsky, and V. V. Shkunov. *Principles of Phase Conjugation*, volume 42 of *Springer Series in Optical Sciences*. Springer-Verlag, Berlin, Heidelberg, 1985.

[11] Pochi Yeh. *Introduction to Photorefractive Nonlinear Optics*. Wiley Series in Pure and Applied Optics. Wiley, New York, 1993.

[12] Robert W. Boyd. *Nonlinear Optics*. Academic Press, 4 edition, 2020.

[13] Bahaa E. A. Saleh and Malvin Carl Teich. *Fundamentals of photonics: Part 1: Optics; 3rd edition.* Wiley series in pure and applied optics. Wiley, Hoboken, 2019.

[14] A.G. de Oliveira, N. Rubiano da Silva, R. Medeiros de Araújo, P.H. Souto Ribeiro, and S.P. Walborn. Quantum optical description of phase conjugation of vector vortex beams in stimulated parametric down-conversion. *Phys. Rev. Appl.*, 14:024048, Aug 2020.

[15] Aarón A. Aguilar-Cardoso, Cheng Li, Tobey J. B. Luck, Manuel F. Ferrer-Garcia, Jeremy Upham, Jeff S. Lundeen, and Robert W. Boyd. All-optical turbulence mitigation for free-space quantum key distribution using stimulated parametric down-conversion. *Optica*, 13(3):386–394, Mar 2026.

[16] A. A. Aguilar-Cardoso, C. Li, T. J. B. Luck, M. F. Ferrer-Garcia, J. Upham, J. S. Lundeen, and R. W. Boyd. Tailoring spatial modes produced by stimulated parametric down-conversion. *Phys. Rev. A*, 112:043541, Oct 2025.

[17] Michael A. Nielsen and Isaac L. Chuang. *Quantum Computation and Quantum Information: 10th Anniversary Edition.* Cambridge University Press, 2010.

[18] Valerio Scarani, Helle Bechmann-Pasquinucci, Nicolas J. Cerf, Miloslav Dušek, Norbert Lütkenhaus, and Momtchil Peev. The security of practical quantum key distribution. *Rev. Mod. Phys.*, 81:1301–1350, Sep 2009.

[19] J. P. Torres, A. Alexandrescu, and Lluis Torner. Quantum spiral bandwidth of entangled two-photon states. *Phys. Rev. A*, 68:050301, Nov 2003.

[20] S.P. Walborn, C.H. Monken, S. Pádua, and P.H. Souto Ribeiro. Spatial correlations in parametric down-conversion. *Physics Reports*, 495(4):87–139, 2010.

[21] Cameron Okoth, Andrea Cavanna, Nicolas Y. Joly, and Maria V. Chekhova. Seeded and unseeded high-order parametric down-conversion. *Phys. Rev. A*, 99:043809, Apr 2019.

[22] Leonard Mandel and Emil Wolf. *Optical Coherence and Quantum Optics.* Cambridge University Press, 1995.

[23] Halina Rubinsztein-Dunlop, Andrew Forbes, M V Berry, M R Dennis, David L Andrews, Masud Mansuripur, Cornelia Denz, Christina Alpmann, Peter Banzer, Thomas Bauer, Ebrahim Karimi, Lorenzo Marrucci, Miles Padgett, Monika Ritsch-Marte, Natalia M Litchinitser, Nicholas P Bigelow, C Rosales-Guzmán, A Belmonte, J P Torres, Tyler W Neely, Mark Baker, Reuven Gordon, Alexander B Stilgoe, Jacquiline Romero, Andrew G White, Robert Fickler, Alan E Willner, Guodong Xie, Benjamin McMorran, and Andrew M Weiner. Roadmap on structured light. *Journal of Optics*, 19(1):013001, nov 2016.

[24] John David Jackson. *Classical Electrodynamics.* Wiley, New York, 3rd edition, 1999.

[25] Y. R. Shen. *The Principles of Nonlinear Optics.* Wiley Classics Library. John Wiley & Sons, Hoboken, USA, 2003.

[26] J. Garrison and R. Chiao. *Quantum Optics.* Oxford Graduate Texts. OUP Oxford, 2008.

[27] Rodney Loudon. *The Quantum Theory of Light*. Oxford University Press, Oxford, 3rd edition, 2000.

[28] J. A. Armstrong, N. Bloembergen, J. Ducuing, and P. S. Pershan. Interactions between light waves in a nonlinear dielectric. *Phys. Rev.*, 127:1918–1939, Sep 1962.

[29] A. Yariv. *Quantum Electronics*. Wiley, 1967.

[30] Wojciech Wasilewski, Czesław Radzewicz, Robert Frankowski, and Konrad Banaszek. Statistics of multiphoton events in spontaneous parametric down-conversion. *Phys. Rev. A*, 78:033831, Sep 2008.

[31] Filippo M. Miatto, Alison M. Yao, and Stephen M. Barnett. Full characterization of the quantum spiral bandwidth of entangled biphotons. *Phys. Rev. A*, 83:033816, Mar 2011.

[32] H. Di Lorenzo Pires, H. C. B. Florijn, and M. P. van Exter. Measurement of the spiral spectrum of entangled two-photon states. *Phys. Rev. Lett.*, 104:020505, Jan 2010.

[33] Alison M. Yao and Miles J. Padgett. Orbital angular momentum: origins, behavior and applications. *Adv. Opt. Photon.*, 3(2):161–204, Jun 2011.

[34] L. Allen, M. W. Beijersbergen, R. J. C. Spreeuw, and J. P. Woerdman. Orbital angular momentum of light and the transformation of laguerre-gaussian laser modes. *Phys. Rev. A*, 45:8185–8189, Jun 1992.

[35] Yang Xu, Sirui Tang, A. Nicholas Black, and Robert W. Boyd. Orthogonal spatial coding with stimulated parametric down-conversion. *Opt. Express*, 31(25):42723–42729, Dec 2023.

[36] Peter W. Shor and John Preskill. Simple proof of security of the bb84 quantum key distribution protocol. *Phys. Rev. Lett.*, 85:441–444, Jul 2000.

[37] Morton H. Rubin, David N. Klyshko, Y. H. Shih, and A. V. Sergienko. Theory of two-photon entanglement in type-ii optical parametric down-conversion. *Phys. Rev. A*, 50:5122–5133, Dec 1994.

[38] Claude E Shannon. A mathematical theory of communication. *The Bell System Technical Journal*, 27(3-4):379–423, 623–656, 1948.

[39] Zhiwei Tao, Yichong Ren, Azezigul Abdukirim, Shiwei Liu, and Ruizhong Rao. Mitigating the effect of atmospheric turbulence on orbital angular momentum-based quantum key distribution using real-time adaptive optics with phase unwrapping. *Opt. Express*, 29(20):31078–31098, Sep 2021.

[40] Mehul Malik, Malcolm O'Sullivan, Brandon Rodenburg, Mohammad Mirhosseini, Jonathan Leach, Martin P. J. Lavery, Miles J. Padgett, and Robert W. Boyd. Influence of atmospheric turbulence on optical communications using orbital angular momentum for encoding. *Opt. Express*, 20(12):13195–13200, Jun 2012.

[41] W. K. Wootters and W. H. Zurek. A single quantum cannot be cloned. *Nature*, 299(5886):802–803, Oct 1982.

[42] A. G. de Oliveira, M. F. Z. Arruda, W. C. Soares, S. P. Walborn, A. Z. Khoury, A. Kanaan, P. H. Souto Ribeiro, and R. Medeiros de Araújo. Phase conjugation and mode conversion in stimulated parametric down-conversion with orbital angular momentum: a geometrical interpretation. *Brazilian Journal of Physics*, 49(1):10–16, Feb 2019.

[43] P. H. Souto Ribeiro, D. P. Caetano, M. P. Almeida, J. A. Huguenin, B. Coutinho dos Santos, and A. Z. Khoury. Observation of image transfer and phase conjugation in stimulated down-conversion. *Phys. Rev. Lett.*, 87:133602, Sep 2001.

[44] M. Liscidini and J. E. Sipe. Stimulated emission tomography. *Phys. Rev. Lett.*, 111:193602, Nov 2013.

[45] D. F. Walls and G. J. Milburn. *Quantum Optics*. Springer, 2008.

[46] David C. Burnham and Donald L. Weinberg. Observation of simultaneity in parametric production of optical photon pairs. *Phys. Rev. Lett.*, 25:84–87, Jul 1970.

[47] Marek Zukowski, A Zeilinger, MA Horne, and Artur Ekert. "event-ready-detectors" bell experiment via entanglement swapping. *Physical review letters*, 71:4287–4290, 01 1994.

[48] C. K. Hong, Z. Y. Ou, and L. Mandel. Measurement of subpicosecond time intervals between two photons by interference. *Phys. Rev. Lett.*, 59:2044–2046, Nov 1987.

[49] Eugene P. Wigner. Normal form of antiunitary operators. *Journal of Mathematical Physics*, 1(5):409–413, 1960.

[50] J. J. Sakurai and Jim Napolitano. *Modern Quantum Mechanics*. Cambridge University Press, Cambridge, 3rd edition, 2020.

[51] V. Bužek, M. Hillery, and R. F. Werner. Optimal manipulations with qubits: Universal-not gate. *Phys. Rev. A*, 60:R2626–R2629, Oct 1999.

[52] Evelyn A. Ortega, Jorge Fuenzalida, Mirela Selimovic, Krishna Dovzhik, Lukas Achatz, Sören Wengerowsky, Rodrigo F. Shiozaki, Sebastian Philipp Neumann, Martin Bohmann, and Rupert Ursin. Spatial and spectral characterization of photon pairs at telecommunication wavelengths from type-0 spontaneous parametric downconversion. *J. Opt. Soc. Am. B*, 40(1):165–171, Jan 2023.